University of Sussex

Nonlinear physics in a microresonator filtered fibre laser

Maxwell Rowley

Submitted for the degree of Doctor of Philosophy

University of Sussex

June 2020

Declaration

I hereby declare that this thesis has not been and will not be submitted in whole or in part to another University for the award of any other degree.

The thesis incorporates published materials to which I have contributed:

"Laser cavity-soliton microcombs." *Nature Photonics* **13** 384-389 (2019) [1]. This is a published paper to which I am an author. My contribution here was in the identification of steady state soliton solutions with the numerical model and the numerical fitting of experimental data. I also supported the experiments and the interpretation of the data.

"Turing patterns in a fiber laser with a nested microresonator: Robust and controllable microcomb generation." *Physical Review Research* - **2**, 023395 (2020) [2]. A paper that is accepted for publication at the time of writing, to which I am an author. My contribution here was in supporting the experimental activities, interpretation of the data, and the numerical fitting, as well as contributing to writing the manuscript.

"Thermo-optical pulsing in a microresonator filtered fiber-laser: a route towards all-optical control and synchronization." *Optics Express* **27**, 19242-19254 (2019) [3]. A published paper to which I am an author. For this work I devised and conducted the experiment, performed the analysis, and wrote the manuscript.

Signature:

Maxwell Rowley

UNIVERSITY OF SUSSEX

Maxwell Rowley, Doctor of Philosophy

Nonlinear physics in a microresonator filtered fibre laser

Summary

The invention of the optical frequency comb (OFC), a type of pulsed laser, has enabled the next leap in precision timing. For this breakthrough, Hall and Hänsch were awarded the Nobel prize in Physics in 2005. Their work has enabled the development of ultra-precise optical atomic clocks that can provide a fractional frequency precision below 10^{-18}. However, such devices are conventionally laboratory-based table-top systems with high power-consumption. To see this technology transition more broadly to everyday applications, developments must be made to create a more efficient and portable device.

The most promising platform for achieving this evolution are microresonators: photonic components which are often integrated within millimetre scale silicon microchips. The microresonator is a ring cavity, which can enable nonlinear processes at very low powers. Specifically, microresonators have been shown to generate OFCs – termed microcombs in this context. This discovery has opened up an exciting field of physics, bringing into the realm of possibility a fully integrated, low-power solution to the practical problem of conventional OFCs.

This thesis contains the results obtained in the *Emergent Photonics* research lab, where I have been studying a laser architecture comprising a microresonator nested within a fibre laser. Utilising such a scheme, I have studied the dynamic and complex regimes of laser operation which can emerge, towards the aim of developing a robust and portable OFC source.

This thesis is structured as follows. First, the system is described, then results on the various regimes of operation are presented: laser cavity-solitons, a self-sustaining localised laser pulse; Turing patterns, non-localised fields which fill the entire optical cavity; and thermal pulses, single-mode pulses of light which form on the 'slow' thermal timescales of the system. Finally, I will present my work on mapping these states within the system and controlling their emergence, along with concluding remarks.

Acknowledgements

First and foremost, thank you to my supervisors, Alessia Pasquazi and Marco Peccianti. Working in the EPic lab here at Sussex has been an absolute pleasure. Thank you for fostering such an encouraging environment, both inside the lab and out, and for all the opportunities - conferences, summer schools and more, that you have offered to me.

Thank you to everybody in the research group. Benjamin, Hualong, and Juan, thank you for your guidance and your friendship. Jacob and Luana, thank you for being part of this period at Sussex with me, and also to everyone else at Sussex that has made this University such a wonderful place over these past years.

To my friends and family, thank you for you support, it means more than you can ever realise.

And finally to Tallia, you made this all possible, thank you.

Contents

List of Abbreviations vii

List of Tables ix

List of Figures xxv

1 Introduction 1

1.1 The state of precision timing and optical frequency combs . . . 1

1.1.1 Optical frequency combs: development and general properties . . . 2

1.2 Miniature optical frequency combs and microresonators . . . 5

1.2.1 Optical microresonators . . . 5

1.3 Microcombs . . . 7

1.3.1 Cavity-solitons . . . 9

1.3.2 Temporal cavity-solitons in microcavities . . . 10

1.4 The future of cavity-soliton microcombs? . . . 13

1.4.1 Temporal laser cavity-solitons . . . 14

1.5 Outline of the thesis . . . 16

2 Laser cavity-soliton microcombs 18

2.1 Introduction . . . 19

2.2 Theoretical model . . . 20

2.3 Experimental results . . . 24

3 Turing Patterns in a microresonator-filtered fibre laser: robust and controllable microcomb generation 35

3.1 Introduction . . . 36

3.2 Theoretical background . . . 38

3.3 Modulational instability of the homogeneous, stationary states . . . 41

3.4 Experimental implementation . . . 43

3.5 Turing pattern selection via the Vernier effect 45
3.6 Fine tuning and phase locking of the Turing patterns 47
3.7 Conclusion 50

4 Thermo-optical pulsing in a microresonator-filtered fiber laser: a route towards all-optical control and synchronisation 52
4.1 Introduction 53
4.2 Experimental setup 54
4.3 Results and discussion 55
4.4 Conclusion 65

5 Spontaneous emergence of laser cavity-soliton microcombs 67
5.1 Introduction 68
5.2 Mapping the soliton regime 70
5.3 Phase resilience of the solitary solutions 74
5.4 Real-time observation of spontaneous laser cavity-soliton emergence 78

6 Summary and future perspectives 82

Bibliography 85

List of Abbreviations

OFC	Optical frequency comb
FSR	Free spectral range
DC	Direct current
NLSE	Non-linear Schrödinger equation
LLE	Lugiato-Lefever equation
CS	Cavity-soliton
CW	Continuous wave
VCSEL	Vertical-cavity surface-emitting laser
QCL	Quantum cascade laser
SIL	Self-injection locked
EDFA	Erbium-doped fibre amplifier
BS	Beam-splitter
PC	Polarisation controller
BPF	Band-pass filter
EYDFA	Erbium-Ytterbium co-doped fibre amplifier
PBS	Polarising beam-splitter
OC	Optical collimator
OSA	Optical spectrum analyser
PD	Photodiode
RF-BPF	Radio-frequency band-pass filter
MZI	Mach-Zehnder Interferometer
MI	Modulational instability
OC	Optical collimator
TS	Trivial solution
PSD	Power spectral density
TD	Translation delay-stage
DWDM	Dense wavelength division multiplexer
WGM	Whispering gallery mode
VOA	Variable optical attenuator
PM	Polarisation maintaining
TM	Transverse magnetic
TE	Transverse electric
FWHM	Full width half-maximum
RMS	Root-mean-square
OSC	Oscilloscope
MB	Maxwell-Bloch
HP-EDFA	High power - Erbium-doped fibre amplifier
PID	Proportional-integral-derivative
DFT	Dispersive Fourier-transform
DCF	Dispersion compensating fibre
EOM	Electro-optic modulator
FPC	Fibre polarisation controller

List of Tables

3.1 Results of the frequency non-uniformity measurements of the data in Fig. 3.6 and Fig. 3.8 for a time gate of 100 ms 49

List of Figures

1.1 **Time- and frequency-domain depictions of an optical frequency comb (OFC) emission.** Top: The electric field of the OFC (black), under mode-locked operation, manifests as a train of optical pulses that are separated in time by the inverse of the cavity repetition frequency. The pulse-to-pulse phase-slip $\Delta\varphi$ is the difference between the peak of the electric field, and its envelope (grey), for sequential pulses. Bottom: Spectral representation of the OFC. The laser emission is shown as coloured spectral lines (from red to blue) within region of gain from the optical amplifier (black dotted curve). The spectral lines are separated by f_{rep} which is determined by the optical cavity path length. The carrier-envelope offset frequency f_{ceo}, is related to the pulse-to-pulse phase-slip as $f_{ceo} = f_{rep}\Delta\varphi/2\pi$. 3

1.2 **Microresonator platforms.** Left: Integrated Hydex microresonator [45]. The micro-cavity can be seen at the lower left side of the chip, and has an FSR of 49 GHz and typical Q-factor above 1 million. Middle: Fused-silica micro-rod resonator. Such resonators are fabricated using a CO_2 laser-lathe process [55] and can be fabricated with FSRs ranging 10s to 100s GHz. The intrinsic Q-factor of such devices is $>10^8$. Right: Fabry-Perot style fibre-resonator. Such devices are fabricated using standard single-mode fibre, and undergo an intensive manual polishing process before a high-reflectivity (99.9935%) coating is applied to both ends of the fibre using an ion-beam sputtering deposition technique. Inset: high-reflectivity fibre mirror coating. 6

1.3 Left: Conceptual illustration of the localised soliton solution in a dissipative system. The opposing effects act to balance one another and manifest the localised solution. (b) Illustration of the power coupled to a single cavity resonance as the relative wavelength of an injected field is swept from low-high wavelengths. For an input power below the threshold of nonlinearity, the resonance is static (often termed the cold-cavity condition: the state when no light-induced effects are present - shown in blue). Above the threshold power, however, the resonance is shifted by the nonlinear response of the cavity (termed the hot-cavity condition: when the presence of light in the system significantly modifies the state via nonlinear effects - shown in red). The real and stable states are shown with the solid red line while the unstable state is depicted with the dashed line. It is clear that in the region highlighted with red shading, bistability exists (i.e. more than one stable solution for a fixed relative injection frequency). The asymmetry of the cavity resonance response, due to the focussing nonlinearity of the material, is illustrative of the critical role played by this relative detuning parameter in nonlinear cavity-systems. 10

1.4 **Schematic of the microresonator filtered fibre laser.** The main fibre cavity (black line) contains the dual-pumped Erbium-doped fibre amplifier (EDFA), a tuneable delay section for adjusting the total optical main-cavity path length, and a free-space section (red-beam). The free space section allows for practical control over parameters of the system in the laboratory and contains a beam splitter (BS) for sampling the intra-cavity field; polarisation control elements (PC) for which we use zero-order half- and quarter-waveplates to control the polarisation and manage losses; an optical isolator to ensure unidirectional operation; and a bandpass filter (BPF) which acts to stabilise the laser operation. The microresonator is nested to close ends of the main-cavity fibres, in a four-port add-drop filter configuration. Practically, the main-cavity fibres are connected to some fibre/ waveguide in order to evanescently couple light from the main-cavity to the microresonator. All fibre components are polarisation-maintaining where possible - the exception is the short fibres directly coupling onto the microresonator chip. 16

2.1 **Principle of operation of microcomb laser cavity-soliton formation.** (a) A short pulse (green) propagates in the micro-cavity (blue) sustained by a longer pulse (red) and a weak higher-order 'super-mode pulse' (purple) in the amplifying loop (yellow). This depicts the fundamental operation of a single soliton per cavity. (b) Cold-cavity spectral distribution. Micro-cavity resonances are depicted in green, amplifying-cavity resonances are in black, with leading and first-order super-modes highlighted in red and purple, respectively. The normalised frequency offset between the central frequency of the leading super-mode and the micro-cavity resonance is Δ; similarly, the frequency offset is $\Delta - 1$ for the central frequency of the first-order super-mode. In the convention used here and in Eq. 2.1, the positive values of Δ correspond to a leading order super-mode red-detuned with respect to the micro-cavity resonances. The variable δ is the normalised FSR detuning, appearing when the two cavities are not commensurate. 21

2.2 **Theoretical propagation of linear and solitary pulses.** The micro-cavity and gain cavity have a group velocity mismatch of $\delta = 0.03$. In these examples we used $\Delta = 0.47$ and $g = 0.14$. The number of super-modes used in the simulations is 61, as defined in Eqs. 2.3 and 2.4. (a) Evolution of the micro-cavity and multi-modal amplifying-cavity fields in the linear case, in normalised units (n.u.). The quantities in the upper and lower panels are the overall field intensities in the two cavities $|a(t,x)|^2$ and $\sum_{-N}^{N} |b_q(t,x)|^2$ (with reference to Eqs. 2.3 and 2.4). The group velocity of the fields is better shown in the insets, where the direction of the field is marked with an arrow. The mismatch between such group velocities causes a periodical decoupling of the fields. (b) Solitary propagation: both fields lock to the same group velocity v. (c) Equivalent spectral distribution of the super-modes within a resonance of the micro-cavity. Such a spectrum, for the linear case (orange), highlights the presence of several frequency components, one for every super-mode with frequency offset $\Delta - q$. In the case of solitary propagation (blue), conversely, all the modes lock to the frequency ϕ. 23

2.3 **Experimental setup for microcomb cavity-solitons' generation and laser-scanning spectroscopy detection of a hot resonator.** The setup is composed of a nonlinear microresonator, an erbium-ytterbium co-doped fibre amplifier (EYDFA), an optical isolator, an optical bandpass filter (BPF), a tunable delay line, a half-wave plate ($\lambda/2$), a polarising beam splitter (PBS) and two optical collimators (OCs). The output signals from the rejection port of the polarising beam splitter were detected with an optical spectrum analyser (OSA), an autocorrelator, and a fast photodetector (PD) connected to an oscilloscope. For the laser-scanning spectroscopy, a scanning CW laser was split into three signals, S1, S2, and S3. S1 was used to probe the resonances' profile and oscillating microcomb lines in the hot microresonator, while S2 and S3 were simultaneously used to perform frequency calibration. This was achieved by beating the external CW source with a reference comb (Menlo Systems, 250 MHz repetition rate). The resulting signal was passed through a radio-frequency bandpass filter (RF-BPF) before detection. In this way, it was possible to generate a set of calibration markers with a spacing of ∼250 MHz. We created an additional set of finer markers by coupling the signal S2 to an unbalanced Mach-Zehnder interferometer (MZI) with an FSR of ∼6.95 MHz. 25

2.4 **Temporal laser cavity-soliton measurement.** (a) Soliton generation, for two equidistant solitons per round-trip. The intra-cavity power at the output of the amplifier is 100 mW and at the output of the micro-cavity is 20 mW. Spectrum (in logarithmic scale) and autocorrelation (A-corr, left inset) with measurements (blue) and theoretical solitary state (red). Fit parameters are $\Delta = 0.49$ and $g = 0.1$, resulting in $\phi = -0.475$, corresponding to a red-shifted frequency of 35 MHz (Eq. 2.2). Right inset: theoretical intensity. (b) Intra-cavity spectrum (blue), showing within each micro-cavity resonance the lasing modes (red dots, red-shifted by ∼32 MHz from the resonance centre). The three plots correspond to the wavelengths highlighted in (a) by coloured shading. (c, d) The same measurements at higher fibre gain for two equidistant solitons per round-trip, leading to a 150 mW intra-cavity power at the output of the amplifier and 30 mW at the output of the ring. Here, $\Delta = 0.47$ and $g = 0.14$, with $\phi = -0.474$. (e, f) The same measurements for three solitons per round-trip. The intra-cavity power is the same as in case (c,d). Here, $\Delta = 0.49$ and $g = 0.11$, with $\phi = -0.474$. The autocorrelation shows that the solitons are not equidistant, highlighting the localised nature of the solution. 26

2.5 **Experimental propagation of soliton pulses.** Here, $\zeta_a = 1.25 \times 10^{-4}, \sigma = 1.5 \times 10^{-4}, \kappa = 2\pi$. We have $\Delta = 0.49, g = 0.1; \Delta = 0.47, g = 0.14$; and $\Delta = 0.49, g = 0.11$ for (a-c); (d-f), and (g-i), respectively. (a) Propagation of two soliton pulses, the intensity is displayed in false colours and logarithmic scale to better visualise the spectrum low energy components. (b) Slow temporal scale (radio-frequency) spectra obtained as the Fourier transform $\tilde{a}(\xi, x_0) = \int a(t, x_0) e^{-2\pi\xi t} dt$ of the propagating solution at the peak (blue, $x_0 = -0.25$) and at the tail (orange, $x_0 = -0.5$) of the pulse along the propagating time axis. Note that the spectra are normalised to obtain a maximum at 0 dB. The frequency axis is normalised with respect to the main-cavity FSR. (c) Comparison of the experimental radio-frequency spectrum (blue) with the background radio-frequency spectrum calculated in the simulations as $\tilde{a}(\xi, x_0) = \int |a(t, x_0)|^2 e^{-2\pi\xi t} dt$. 29

2.6 **Stable non-localised states.** Coherent state obtained with a setup similar to that of Refs. [127, 156]. States with different FSR are obtained by adjusting the cavity length with a similar procedure to that used in Refs. [156, 158]. (a) Optical spectrum, autocorrelation (left inset) and radio-frequency spectrum (right inset) of a coherent state at repetition rate equivalent to a single microring FSR (approximately 50 GHz). (b) Laser-scanning spectroscopy measurement for the most powerful spectral line, marked by a green line in panel (a). The measurement clearly shows a blue-detuned oscillation (c, d) Same measurement as in (a,b), for a coherent state at the repetition rate twice the microring FSR (approximately 100 GHz). (g,h) Same measurement as in (a,b), for a coherent state at a repetition rate equivalent to four-times the microring FSR (approximately 200 GHz). 30

2.7 **Temporal laser cavity-soliton and Lugiato-Lefever cavity-soliton comparison.** (a) Plot of laser cavity-soliton input field peak power versus normalised offset Δ, calculated for various gain values ($g = 0.05$ to 0.14 for plots from purple to green). Thick lines mark the stable self-localised solutions, both in the main graph and the inset, where the soliton frequency ϕ is reported. Note that negative values of ϕ correspond to frequencies red-shifted with respect to the micro-cavity centre, in agreement with the experiments. The grey area marks the region of existence for Lugiato-Lefever bright solitons. (b) Intensity profile on the micro-cavity for a laser cavity-soliton ($\Delta = 0.47$ and $g = 0.14$, blue line) and a Lugiato-Lefever cavity-soliton at the power threshold (orange line), highlighting the presence of a strong background in the latter case. (c) Spectrum of the theoretical cases in (b). The strong background of the Lugiato-Lefever cavity-soliton results in a dominant comb mode at the centre of the spectrum. Laser cavity-soliton lines generally possess a higher power spectral density. . . . 32

2.8 **Control of the repetition rate of temporal laser cavity-solitons.** (a) Specta for three combs as the fibre cavity length is changed within a broad range of 150 µm. Gain and losses have been readjusted to maintain the solitary state showing two equidistant solitons per round-trip. Intra-cavity powers are 20 (blue), 25 (orange), and 30 mW (black), respectively. (b) Residual frequency shift against mode number with respect to the best fit for the comb 1 case (blue). Error bars are defined as the size (10 %–90 %) of the slope associated to the Hilbert transform phase in the laser-scanning spectroscopy interferogram. Combs 2 and 3 show a change in FSR and, hence, repetition rate variations of 1.9 MHz and 3.2 MHz with respect to comb 1. (c) Calculated propagation of a stationary solitary solution when $\Delta = 0.49$ and $g = 0.1$, for $\delta = 0$, 0.01 and 0.02. The solitary wave is maintained in all three cases. 34

3.1 (a) Depiction of the laser operation. A Kerr microresonator (green ring) is nested into an amplifying fibre loop (yellow). A Turing pattern waveform (light-green) is excited in the micro-cavity and is sustained by leading order (red) and first-order (blue) 'super-mode' waveforms from the amplifying loop. These super-modes are periodical with the micro-cavity length, highlighted by a line segment L_a. (b) Spectral distribution of the modes in the cold-cavity condition. The micro-cavity resonances (green) have a free spectral range (FSR) denoted F_a while the FSR of the amplifying main-cavity modes (black) is denoted F_b. The leading order and first-order super-modes are plotted in red and blue, respectively. (c)-(e) Zoom of the m^{th}, central, and $-m^{th}$ resonances. Δ is the normalised frequency offset between the central frequency of the leading super-mode and the micro-cavity resonance. δ is the normalised FSR detuning, appearing when the two cavities are not commensurate. 38

3.2 Modulation instability (MI) maps for the stationary states. For the calculations: $\zeta_a = 1.7 \times 10^{-4}, \zeta_b = 3.5 \times 10^{-4}, \sigma = 2.5 \times 10^{-4}, \sqrt{\kappa} = 2.5$, which are compatible with the experimental regime discussed in the sections below. Here we used $N = 7$, corresponding to a total of 15 super-modes.(a) MI map for the trivial solution (TS) showing the regions of instability as a function of the cavity gain g and detuning Δ, with $\delta = 0$. (b) MI gain of the zero solution with $g = 0.03$ (indicated by a white dashed line) and $\delta = 0$. (c) MI gain of the low energy CW state I_0^+. (d) Zoom out of (c). (e,f,g,h) same as (a,b,c,d) with $\delta = 1/3$. 41

3.3 Self-starting Turing pattern states. The zero solution evolves into the state $I_+^{(0)}$, which is also unstable and gives rise to a Turing pattern. The simulation parameters are: $\zeta_a = 1.7 \times 10^{-4}, \zeta_b = 3.5 \times 10^{-4}, \sigma = 2.5 \times 10^{-4}, \Delta = -0.17, \sqrt{\kappa} = 2.5, g = 0.0365, \delta = -0.3342$ and $N = 7$. (a) Evolution of the temporal profile of the field in the micro-cavity with the y-axis normalised to the micro-cavity length. (b) Maximum intensity of the evolution in the micro-cavity. (c) Low energy stationary states. (d) Output time profile of the fields in the micro- and main-cavities. (e) Output spectral profiles of the fields within the micro- and main-cavities, with power spectral density (PSD) as a function of the normalised relative frequency. 44

3.4 (a) Experimental setup of the micro-resonator filtered fibre laser. EYDFA, Erbium-Ytterbium doped fibre amplifier; TD, translation delay-stage; BPF, bandpass filter; OC, output coupler. (b) Diagnostic setup for the laser scanning spectroscopy. PD, photodiode; MZI, Mach-Zehnder interferometer; RF-BPF, radio-frequency bandpass filter. (c) Diagnostic setup for the frequency non-uniformity measurement. The beat notes B1, B2, and B3 between the three desired comb lines W1, W2, and W3 and their adjacent reference frequency comb lines are selected using a dense wavelength division multiplexer (DWDM). They are then mixed and counted by a high-resolution frequency counter. 45

3.5 (a,d,g) Experimental optical power spectral density (PSD) for the micro-comb modes. The inserts depict the autocorrelation and the intra-cavity spectrum of the oscillating spectral mode with the highest power. The red line here shows the position of detuning Δ used in the respective simulations. The colour shadings in (d) are in reference to the resonance profiles presented in Fig. 3.6. (b,e,h) Simulated optical spectra calculated a $\delta = 1/2, 1/3$, and $1/4$ respectively, with corresponding gain settings and cavity detunings of (b) $g = 0.0400, \Delta = -0.36$, (e) $g = 0.0320, \Delta = -0.17$, and (h) $g = 0.0501, \Delta = -0.54$. (c,f,i) MI gain spectrum of the CW states. In the calculations: $\zeta_a = 1.7 \times 10^{-4}, \zeta_b = 3.5 \times 10^{-4}, \sigma = 2.5 \times 10^{-4}, \sqrt{\kappa} = 2.5$, and $N = 7$. 46

3.6 Experimental resonance profiles and beat note signals obtained with the probe laser scanning oscillating comb lines. (a-e) Descending rows correspond to a relative change in the main-cavity length of 0 µm, −100 µm, −200 µm, −300 µm and −400 µm. The four sequential colour-shaded plots correspond to different comb line wavelengths: 1547.13 nm, 1549.47 nm, 1550.64 nm and 1553.01 nm from the left to the right panels, as indicated by the colour shadings in Fig. 3.5(d). The dashed red line is a Lorentzian fit to the profile of the hot resonance while the vertical dashed-blue lines indicate the relative shift of the oscillating comb lines within their respective resonances. 48

3.7 (a,b) Numerical results showing the evolution of the temporal (a) and the spectral (b) profile of the field. The temporal evolution has a corresponding zoom of the stable operation to illustrate more clearly the pattern. For the simulations: $\zeta_a = 1.7 \times 10^{-4}, \zeta_b = 3.5 \times 10^{-4}, \sigma = 2.5 \times 10^{-4}, \Delta = -0.17, \sqrt{\kappa} = 2.5, g = 0.0365, \delta = -0.3942$, and $N = 7$. (c) Optical spectrum of the stable pattern state. (d) Differential phase evolution of three comb modes, indicated by the coloured shading in (c). The differential phase is calculated as the derivative of the absolute phase ψ_n over the temporal evolution and it is indicative of the stability intrinsic to the repetition rate of the comb. 49

3.8 (a) The average beat note frequencies between two selected microcomb lines and their adjacent reference frequency comb teeth (recorded by an oscilloscope) as a function of the decreasing main-cavity length. The raw frequency measurement (in megahertz), relative to the frequency for 0 µm delay, is shown in blue. (b) Distribution of the microcomb output spectrum stemming from an equidistant mode spacing, including a Gaussian fit (dashed red line). Here, we consider the −300 µm delay case, with a frequency counter gate time of 100 ms. 50

4.1 (a) Schematic of the experimental setup. PC, fibre polarisation controller; VOA, variable optical attenuator; BPF; bandpass filter; EDFA, Erbium-doped fibre amplifier; OSC, oscilloscope; OSA, optical spectrum analyser. Inset: Side view of the silica rod resonator and coupled fibre used for optical injection. (b) OSA transmission spectra of the resonator (grey) and BPF (blue shading) when seeded by the EDFA. (c-e) High-resolution transmission spectra obtained by CW wavelength sweep using either unpolarised (c) or polarised transverse magnetic (TM) (d) and transverse electric (TE) (e) light. (f) Zoom on the predominant spatial modes oscillating for each polarisation. (g) Spectrum of the selected TM main resonance and Lorentzian fit (dashed black line) used experimentally. 56

4.2 (a) Typical pulse trace measured experimentally using the setup shown in Fig. 4.1 in TM polarisation. (b) Zoom on a single pulse period. (c) Corresponding OSA spectrum. (d) Phase space portrait depicting the intensity versus the derivative of the intensity of the pulse train in panel (a). 57

4.3 (a) Schematic of the physical process that leads to a thermo-optically induced slow self-pulsing emission of the laser. The thermo-optical nonlinearity of the microrod modifies the refractive index, and thus the resonance frequency of the micro-cavity, as the laser intracavity power increases. As the resonance shifts, the cavity transmission is reduced, leading to a reduction in power and eventually the repetition of the process, resulting in the pulsed emission. The loaded Lorentzian resonator mode within the filtered bandwidth of the EDFA (shaded blue region around 1545 nm) dynamically shifts by an amount $\Delta\nu$ via the thermo-optical effect (see gradient arrow and coloured shadings). This shift is also expected across all resonances and as such, can be readily measured experimentally using a CW probe weakly coupled and slightly detuned from a resonance far outside the main cavity gain bandwidth (see e.g. red and blue arrows around 1561 nm). (b) Numerical results obtained using the coupled mode equations of Eqs. 4.1-4.4 for parameters yielding self-pulsing $|a|^2$ (solid blue line - see Eq. 4.1) shows a train of pulses associated with a periodic resonance frequency shift $\Delta\nu$, induced by thermo-optical effects (dashed purple line - see Eq. 4.4). (c) Example of pulse train obtained experimentally (solid black line) and corresponding transmission of a red-detuned (dashed red line) CW field, used to retrieve the dynamical resonance spectral shift as shown in (a). (d) Same measurements using a blue-detuned CW probe (dashed blue line). . 59

4.4 (a, b) Scatter plots of pulse peak power and duration obtained experimentally using the setup shown in Fig. 4.1(a). Here, data are extracted for various cavity transmission values (see colour scale, where 100 % transmission represents the minimum attenuation state of the VOA) and the EDFA gain settings, while increasing (a) or decreasing (b) the EDFA gain by adjustment of its pump current. The inset in (a) corresponds to the same scatter plot, obtained experimentally by replacing the initial EDFA in the setup by a longer and higher power gain medium (HP-EDFA). Here, the data are also obtained for various cavity transmission values while increasing the EDFA gain, but the colour scale instead represents the gain medium pumping current. (c) Scatter plot of the mean pulse duration and period obtained experimentally for various loss values and upward tuning of the gain. This analysis was performed using both available amplifiers (see legend) and by averaging the properties extracted from each ms-long experimental trace. (d) Corresponding properties retrieved from numerical simulations using a selected loss parameter α. Scatter points of the pulse properties are displayed for various values of normalised gain $G = g_0/\alpha$ (see colour scale). The numerical results are obtained using the coupled-mode equations of Eqs. 4.1-4.4 for selected parameters yielding self-pulsing behaviour. The pulse properties were extracted from the numerical field intensity via the same post-processing used on the experimental data sets. The grey shading region (featuring clusters of points instead of a point), corresponds to a dynamical regime where simulations exhibit self-pulsing only sustained for a limited period (i.e. in a slow transient ultimately leading to a stable CW solution). 62

4.5 (a-b) False colour maps showing the average intra-cavity power (see colour scale) for experimental measurement of the laser cavity operation. Measurements are performed for a range of loss values while increasing (a) or decreasing (b) the gain. (c-d) Corresponding map of the pulse peak powers displaying clear regions of self-pulsing operation (i.e. black areas are representative of parameters for which self-pulsing is absent - see colour scale). (e-h) Examples of phase space portraits retrieved from experimental data measured at selected transmission of 50 % (e,f) and 70 % (g,h), respectively. As these panels show, we observe different self-pulsing conditions around the attractor when increasing (e,g) and decreasing (f,h) the gain, even for the same cavity parameters, thus attesting to a variety of multistable regimes. 63

4.6 (a-d) Examples of experimental laser cavity dynamics observed when using a strong counter-propagating CW field (purple line) to both probe and influence the main cavity pulsing properties (blue line). The parameters of the main amplifying cavity are kept constant and a 15 mW CW probe around 1560 nm is coupled to the resonance but not frequency-stabilised. The drift of the CW around this resonance leads to a variety of slow-fast and multistable dynamics observed in self-pulsing and correlated to the CW field coupling, whose induced thermo-optical effects on the resonator properties can no longer be neglected. The panels show different regimes. (a) The CW detuning and associated coupled power initiates the self-pulsing. (b) A transient behaviour due to the passage from blue to red frequency detuning from the resonance. (c) Slow-fast dynamics associated with complex and threshold-like coupling behaviour. (d) Frequency doubling of the self-pulsing operation. 64

5.1 Illustration of the concept of a nonlocal nonlinearity permitting a self-starting, globally stable system. The change in stability of the stationary states for ‘cold’ and ‘hot’ cavities. The oscillating field grows from the initial modulational instability (MI) present in the zero energy state, and under the proper setting of global cavity parameters, evolves towards the stable soliton state. In this energetic regime, the global cavity settings are impacted by the nonlinearity such that the zero energy solution is shifted to detuning away from the MI region where the background state is stable and soliton solution is maintained. 70

5.2 (a) The spectral bandwidth of the laser output, corresponding to the colour scale inset, for various settings of the cavity global parameters - namely cavity length and amplifier pumping voltage. The temperature was kept within a fluctuation of few degrees at 20 °C. The soliton states with the largest bandwidth and are clearly identified in the orange/red region in the centre of the map. In the lower left section of the map, a stable region admitting CW/Turing pattern states is clearly identifiable. The radio-frequency spectrum is analysed to identify unstable regions of the map and are marked by a cross. The insets to the right of the map are repeat measurements of the entire scan acquired over a continuous 40 hour period. (b) The wavelength of each spectral mode is plotted for the fixed cavity length of 84 µm (dashed black line in (a)). The pump power increment is 1.3 mW, and the spontaneous transition from a CW state into the single soliton state is clearly identifiable. (c) Example measurements of the lasers optical spectrum, radio-frequency and autocorrelation traces are presented for 347.1 mW, 353.6 mW and 362.7 mW (indicated by the white circles in (a)). Here we observe both single- and two-soliton states, as well as CW operation. 72

5.3 (a) The spectral bandwidth of the laser output, corresponding to the colour scale inset, for various settings of the cavity global parameters - namely cavity length and amplifier pumping voltage. Temperature was kept with a fluctuation of few degrees at 20 °C. The soliton states the largest bandwidth and are clearly identified in the orange/red region in the centre of the map. The radio-frequency spectrum is analysed to identify unstable regions of the map and are marked by a cross. (b) The wavelength of each spectral mode is plotted for the fixed cavity length of 44 µm (dashed black line in (a)). The pump power increment is 1.3 mW (c) Example measurements of the lasers optical spectrum, radio-frequency and autocorrelation traces are presented for 366.8 mW, 392.8 mW and 401.9 mW (indicated by the white circles in (a)). Here we observe three-soliton states, with 5-FSR non-localised Turing patterns. 74

5.4 (a) Wavelength detuning of the central lasing mode in the soliton region versus laser pump power, exceeding the free-spectral range (0.62 pm) of the laser cavity for the case in Fig. 5.2, along with intracavity power at the output drop port of the microcavity. (b) Same for the case in Fig. 5.3. (c) An example of recovery from perturbation of soliton state. Measured drop power (blue line) shows the transition from the laser off-state, after a mechanical perturbation to the stable soliton, and then the recovery of a stable state. The spectra (inset) measured shows the recovered soliton case and corresponding auto-correlation trace. The power of a weak CW probe (red line), coupled in the 1560 nm microresonator resonance, is shown to measure the nonlinear shifting of the microcavity during the formation process. 75

5.5 Dispersion of the oscillating lines within the microcavity. (a) Typical laser scanning spectroscopy measurements of a blue detuned oscillating line (top), red detuned line (centre) and coexistence of two oscillating modes (bottom). The detuning is calculated as the frequency difference between the centre of the microcavity resonance and the oscillating line. (b) Distribution of the detunings for the spectral modes in the example cases of Fig. 5.2(c). The primary oscillating laser lines are marked with a circle, while the secondary resonance, if any, is marked as a cross. (c) Distribution of the detunings for the modes in Fig. 5.3(c). 76

5.6 (a) Schematic of the modulated dispersive Fourier-transform spectroscopy (DFT) setup. The microcomb pulse train passes through an optical isolator and fibre polarisation controller (FPC) before an electro-optic modulator (EOM) is used to window and select a few pulses. The microcomb repetition rate is in the 50 GHz to 100 GHz range, so each 300 ps window contains tens of pulses. These pulses are then propagated through a length of dispersive optical fibre. The temporal separation induced by the dispersive fibre, is orders of magnitude greater than the initial temporal separation of the individual pulses; thus interference between multiple pulses is insignificant in measurement. The signal is amplified before being detected by a fast photodiode (EOT - 16 GHz) and oscilloscope (Teledyne Lecroy - 36 GHz). (b) Illustration of the measurement concept. The microcomb pulse train (black) is windowed by the EOM (red), before passing through a significant length of dispersive fibre to reach the far-field Fourier-transform limit where spectral components are effectively mapped to the temporal domain. 80

5.7 (a) The temporal DFT measurement is plotted in a 2D figure, with the fast-time axis (determined as the period of the EOM) in the y-axis and the slow-time axis on the x-axis. The measurement illustrates the spontaneous formation of a soliton state from the 'off' state. The normalised average energy of the signal is shown above. A period of apparent chaos, the duration of which is in-line with the response time of the microresonator thermo-optical effects, is followed by settling into stable soliton operation. The linear optical spectrum corresponding to this stable state is shown to the right of the 2D plot, with the corresponding autocorrelation shown in the inset. For reference, the log-scale optical spectrum is shown above. . . 81

Chapter 1

Introduction

1.1 The state of precision timing and optical frequency combs

Time is a fundamental component of nature. Its universality facilitates our shared interpretation, and its irreversibility is vital in the emergence of structure [4, 5]. In complex systems, the passage of time enables the emergence of a myriad of phenomena, from the weather to life itself. Historically, the universal standardisation of time measurement has been at the heart of scientific research [6], ultimately enabling global synchronisation and the complex networks and infrastructures around which modern society is built.

Our capability to observe and record our universe with increased precision is a fundamental enabling technology crossing, at different degrees, all fields of research: from the simple pendulum to quartz oscillators, and finally, to the atomic clock, time-keeping has promoted scientific evolution across the centuries. The global primary standard for time and frequency measurements, set in 1967, is currently based on locking to the microwave frequency of a hyperfine transition of caesium [7]. Towards the next generation of time standards, *optical* atomic clocks are the likely successor - with optical transitions in cold atoms or trapped ions constituting reference oscillators that can provide a fractional frequency precision beyond the 10^{-18} level [8–14]. In this regard, modern time-keeping is underpinned by the absolute measurement of frequencies, which lay in the visible spectrum for optical atomic clocks.

The measurement of frequencies in the optical regime was a substantial challenge until the advent of the wide-bandwidth optical frequency comb laser, which enabled the translation of the optical reference stability down to the microwave domain. This coherent link between optical and electronic domains, in the form of optical frequency comb lasers, eventually boasted the progress in high accuracy clocks and precision spectroscopy, and

are discussed in detail in the following sections.

The works presented in this thesis pertain to the ongoing global research effort to the advancement of optical frequency comb lasers and in particular, their miniaturisation. The miniaturisation of these devices aims to enable the next generation of portable photonic technologies, including portable optical atomic clocks for deployment in space. The main topic of my work is in the investigation into novel laser schemes for the miniaturisation of optical frequency combs, and the relevant background will be covered in the following sections.

1.1.1 Optical frequency combs: development and general properties

The Nobel prize in Physics was awarded in 2005 in part to Hall and Hänsch for their work on optical frequency combs (OFCs). As introduced above, this type of pulsed laser enabled a new generation of optical atomic clocks with fractional frequency precisions below 10^{-18} [6, 9, 15–17]. Moreover, the frequency stability of OFCs allowed critical applications in many important sectors, from fundamental measurements of natural constants [18, 19], to ultra-low-noise microwave generation [20, 21], dual-comb spectroscopy [22], and astronomical calibrations [23–25], among others [26].

These pulsed sources, in general, are based on standard mode-locked lasers [27–29], which produce periodic ultrashort optical pulses by establishing a fixed phase relationship between a set equally-spaced frequencies [29]. Because these frequencies are equally spaced, these lasers have a spectrum with a characteristic 'comb' shape, where every ultra-narrow frequency line represents a tooth of a comb. The phase relationship provided by standard mode-locking approaches alone does not, however, guarantee absolute knowledge of each optical frequency, or tooth, in the comb.

Every comb is, in general, defined by two fundamental quantities which must be defined and controlled. Namely, the pulse repetition rate frequency f_{rep} and the carrier-envelope offset frequency f_{ceo} [30, 31]. These quantities are best understood with a time and frequency domain representation of the comb laser (Fig. 1.1). With the proper definition, the repetition rate and carrier-envelope offset frequencies determine the *exact* position of all the modes of the comb.

The inverse repetition rate, $1/f_{rep}$, of the laser is the periodical separation in the time-domain between sequential pulses (the peak of the envelope of the total electric field). In the frequency-domain, this quantity is the separation of the modes of the laser, also called free spectral range (FSR). For mode-locked lasers this value is usually above the 100 MHz

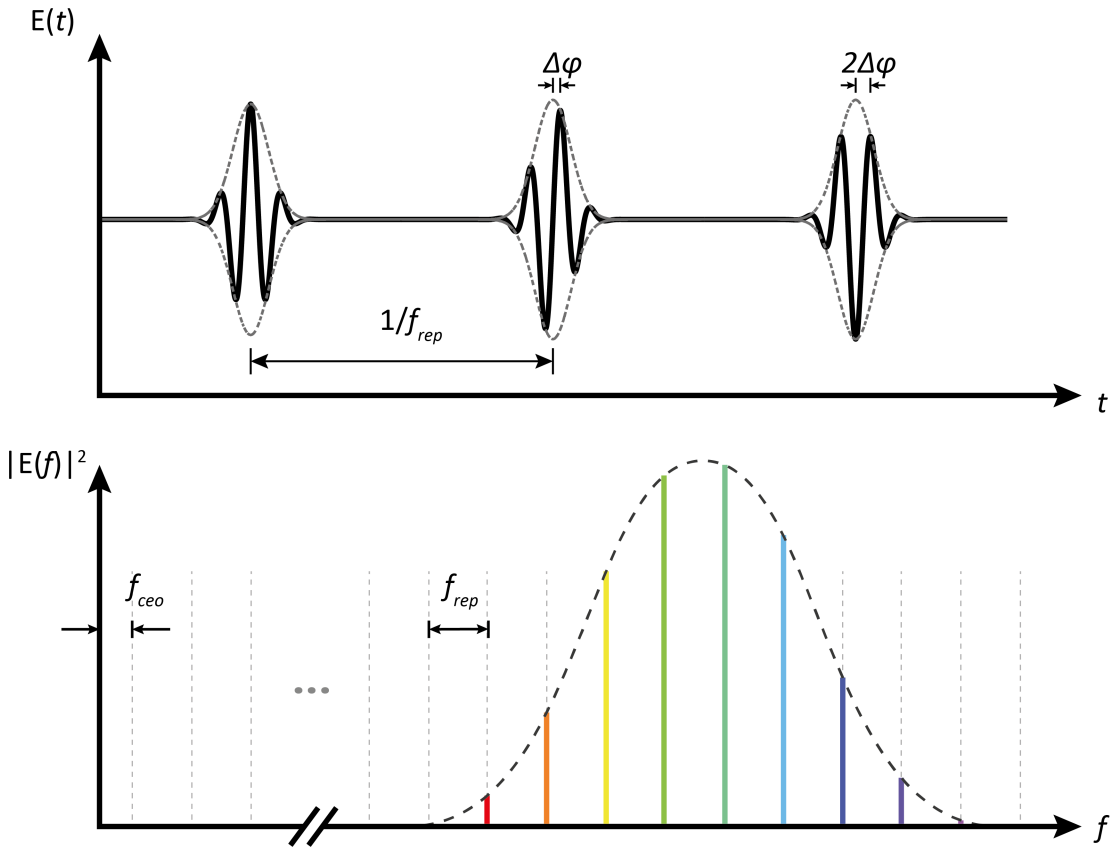

Figure 1.1: Time- and frequency-domain depictions of an optical frequency comb (OFC) emission. Top: The electric field of the OFC (black), under mode-locked operation, manifests as a train of optical pulses that are separated in time by the inverse of the cavity repetition frequency. The pulse-to-pulse phase-slip $\Delta\varphi$ is the difference between the peak of the electric field, and its envelope (grey), for sequential pulses. Bottom: Spectral representation of the OFC. The laser emission is shown as coloured spectral lines (from red to blue) within region of gain from the optical amplifier (black dotted curve). The spectral lines are separated by f_{rep} which is determined by the optical cavity path length. The carrier-envelope offset frequency f_{ceo}, is related to the pulse-to-pulse phase-slip as $f_{ceo} = f_{rep}\Delta\varphi/2\pi$.

range [26] and can be measured with a fast-photodetector as the beatnote between adjacent comb teeth.

The carrier-envelope offset frequency, f_{ceo}, represents the pulse-to-pulse phase shift of the electric field. In the spectral representation this frequency can be seen by extrapolating the comb teeth down towards DC frequencies, where, practically, it defines the frequency of the first tooth of the comb. Together with the repetition rate frequency, it defines the comb completely:

$$f_n = nf_{rep} + f_{ceo} \tag{1.1}$$

where f_n in general indicates the nth mode of the spectrum.

The f_{ceo} is a significantly challenging quantity to measure requiring complex interferometric methods, the development of which has been at the heart of the progress in the field of OFCs.

For the extraction of f_{ceo}, the so-called *f-2f* interference technique is most commonly applied. This method is based on heterodyning a frequency-doubled comb line, of initial frequency f_n, with a comb line at the high-end of the laser spectrum, of frequency f_{2n} [32]. Clearly, this method requires an octave-spanning comb, which is a non-trivial task. Although other approaches have been proposed, and even implemented [33, 34], *f-2f* interference remains the standard. The slight difference between the two heterodyned frequencies permits a direct measurement of the carrier-envelope offset frequency f_{ceo} as:

$$2f_n - f_{2n} = 2(nf_{rep} + f_{ceo}) - (2nf_{rep} + f_{ceo}) = f_{ceo} \tag{1.2}$$

Today, OFC-based technology is a relatively mature field, with a range of companies providing such lasers spanning a vast range of wavelengths. The first implementations utilised high-power Ti:sapphire mode-locked lasers which were capable of generating octave-spanning spectra [35, 36], but the common modern commercial approach is generally based on Erbium-fibre mode-locked lasers with some external spectral broadening to achieve octave-spanning combs [37].

These fibre lasers comprise all polarisation-maintaining elements and are passively mode-locked using a saturable absorber [37]. Complete stabilisation of the comb teeth can be achieved by locking the comb to an optical atomic reference frequency. Measurement of the laser repetition rate, in conjunction with the self-referencing technique, enables all the degrees of freedom of the laser to be fully stabilised. In this case, the OFC is able to provide an output microwave signal with the exact frequency stability of the optical atomic reference. Practically, control and stabilisation of these parameters is often achieved by fast cavity-length actuation by an intracavity piezo-electric delay.

Over these past 20 years, OFCs based on mode-locked lasers have enabled a vast array of ground-breaking research as a result of their precision and versatility. Time and frequency metrology, in particular, has advanced rapidly during this period, with OFCs as a central component for precision frequency measurements [38, 39]. With regard to precision measurement of atomic references, OFCs will be a fundamental element in the upcoming redefinition of the second [11, 26, 40, 41].

The next epoch in precision time measurement will be enabled when portable OFCs and

optical atomic clocks are readily available outside of controlled laboratory environments. For such an application, a dramatic reduction to the physical dimensions as well as the overall power consumption of conventional OFCs and atomic references will be required. Ultra-precise portable optical clocks would reliably provide the necessary timing reference to ensure faster data-transfer rates, as well as an alternative positioning reference - independent from vulnerable satellite networks, when available in conjunction with state-of-the-art quantum sensors [42]. With the aim to enable these revolutionary technologies, there is a significant global research effort towards developing compact, reliable, and robust OFC sources.

1.2 Miniature optical frequency combs and microresonators

Over the last 50 years, there has been a steady drive in developments of novel optical materials. Fibre-optic technologies, particularly at Telecom wavelengths, have seen continuous developments in manufacturing approaches, materials, and novel fibre geometries. Likewise, there have been significant developments to integrated photonic platforms [43–45], especially since the internet revolution, which drove the demand for novel photonics-based technologies to manipulate and filter optical signals [46].

One such component, which has seen applications over a broad range of sectors, are optical microresonators. Such cavities confine light by total internal reflection and have been fabricated in a range of platforms and materials - in both bulk and integrated forms. Many applications of these devices are focussed towards optical signal processing, such as optical filters, switches, and modulators [46–48]. In particular, such a component is significantly attractive for the field of nonlinear optics, where long photon lifetimes in a cavity enables a significant quantity of photon interaction processes to occur. These nonlinear processes and their application towards a compact OFC will be explored in the next sections.

1.2.1 Optical microresonators

Microphotonics advances have enabled the development of high-Q optical micro-cavities in a range of platforms [49–53]. The resonant enhancement of waves confined in a cavity by total internal reflection was studied by Lord Rayleigh, where the total internal reflection of sound waves in a resonator was observed - so-called whispering-gallery modes. Optical microresonators are sub-millimetre-scale optical cavities which have been fabricated with free-spectral ranges (FSR) from 10s to 1000s GHz [50, 52]. In monolithic,

bulk platforms, the optical mode propagates along the resonator side-wall [54], confined by the total internal reflection of light. More recently, integrated microresonators have been developed. These ring-waveguides confine light due to the high contrast between the refractive index of the waveguide to its surrounding materials and are more suited to large-scale manufacturing and integration than their bulk counterparts. Beyond their

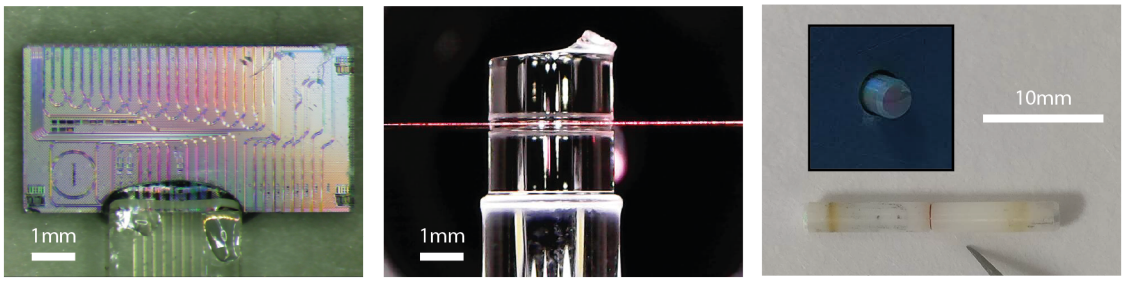

Figure 1.2: Microresonator platforms. Left: Integrated Hydex microresonator [45]. The micro-cavity can be seen at the lower left side of the chip, and has an FSR of 49 GHz and typical Q-factor above 1 million. Middle: Fused-silica micro-rod resonator. Such resonators are fabricated using a CO_2 laser-lathe process [55] and can be fabricated with FSRs ranging 10s to 100s GHz. The intrinsic Q-factor of such devices is $>10^8$. Right: Fabry-Perot style fibre-resonator. Such devices are fabricated using standard single-mode fibre, and undergo an intensive manual polishing process before a high-reflectivity (99.9935%) coating is applied to both ends of the fibre using an ion-beam sputtering deposition technique. Inset: high-reflectivity fibre mirror coating.

linear properties, microresonators with high Q-factors are particularly well suited for nonlinear applications. The Q-factor is a dimensionless quantity used to assess the optical field enhancement factor in resonators and can be defined by the ratio of the resonance frequency f, and its corresponding linewidth δf.

$$Q = \frac{f}{\delta f}. \tag{1.3}$$

This factor is generally influenced by the material bulk and surface absorption and scattering levels, as well as by the level of unwanted nonlinear absorption losses. On integrated platforms, Q-factors of almost one billion have been achieved [56].

It is worth to highlight silicon-oxynitride as a platform, since it is integrated resonators made in this platform which are used in Chapters 2, 3 & 5. These microresonators in particular are fabricated by collaborators at City University Hong Kong and details of the devices may be found in Ref. [45]. The strong resonant enhancement of the optical field in high-Q microresonators enables extremely intense intra-cavity fields, thus unlocking the numerous functionalities of nonlinear optics at relatively low energy levels. Additionally,

silicon-based materials have an extremely large nonlinear coefficient, and utilising these low-threshold nonlinearities has lead to the emergence of the new field of OFCs generated in microresonators: microcombs.

1.3 Microcombs

Optical frequency combs generated from microresonators – or microcombs, have galvanised the international photonics research sector as the platform for an extremely compact optical frequency comb source. Distinct from conventional mode-locked lasers, microcombs operate by utilising the strong optical nonlinear properties of microresonators to generate OFCs [57, 58].

The relevant nonlinear process is four-wave mixing, which is associated with the Kerr effect - an intensity dependant nonlinear interaction of photons that is the dominant nonlinear process in centrosymmetric materials [59]. Although there have been recent advances utilising materials with a non-zero second-order electric susceptibility $\chi^{(2)}$ [60, 61], the main works in the field and the works contained in this thesis regard combs utilising the Kerr effect. This ultrafast interaction enables the generation of photons at new frequencies under the appropriate conditions, and it was shown that by driving a microresonator with an external pump laser, this process could cascade to form a set of spectral comb teeth, separated approximately by the FSR of the microresonator [62–65]. These spectral lines, given the right conditions, can manifest as temporal structures. There has been a significant research effort to enable coherent output of the newly generated spectral lines and to control the emergent temporal structures [66, 67].

Outside the field of microcombs, there is a rich historical background of the emergence of structure in nonlinear dissipative systems in biology and chemistry, with pioneering work by Alan Turing on patterns forming in reaction-diffusion systems [68]. More generally in optics, structures of light in dissipative systems have been under investigation for several decades [69–73].

Some seminal works of the early 1990's studied the formation of dissipative *temporal* structures arising from modulational instabilities of the steady-state in a driven nonlinear ring cavity [74]. The structures presented in this theoretical work are known as Turing patterns; they are non-localised periodical patterns which fill the entire cavity and are modelled with a variation of the nonlinear Schrödinger equation (NLSE) called the Lugiato-Lefever equation (LLE). The LLE is ultimately a NLSE with the addition of a damping term and a driving term (also accounting for the detuning of the driving field frequency from the cav-

ity resonance centre). Prior to this work in the temporal domain, dissipative structures had been mostly studied in the spatial domain, where the LLE was originally formulated to describe the onset of stationary patterns in the planes orthogonal to the propagation direction of light in a driven, damped, Kerr medium [73, 75, 76]. This formulation is a mean-field model, describing the slowly varying envelope of the electromagnetic field in the presence of nonlinearity and diffraction. Such spatially patterned states, which are independent of boundary conditions, were initially observed experimentally in liquid crystals [77, 78] and subsequently in semiconductor resonators [79].

Focussing to the *temporal* patterns that were described in an externally driven ring-cavity by Haelterman et al. in [74], the diffraction term of the LLE is replaced by a term for the group velocity dispersion of the optical fibre. The solutions found, in this case, are dissipative structures that form along the propagation direction of the electric field. These patterned structures were indeed later observed in experimental systems [80].

Further to this work, it is clear that externally driven microresonators are fundamentally analogous to the fibre ring cavity, on a micro-scale. Temporally patterned states have indeed been observed on both platforms [80–83].

Intuitively, one might best understand these temporal patterns in one dimension, where they manifest out of a continuous wave (CW) signal (constant intensity) in a cavity, which naturally experiences an instability in the form of a perturbation. At certain frequencies, this perturbation can be reinforced by nonlinearities in the cavity, leading to its growth and, eventually, the formation of a stable oscillatory signal at the frequency under appropriate conditions. Temporally, this appears as a modulated waveform while spectrally, the optical modes take a comb structure (The generation of these new frequencies originate from the CW signal and are created via nonlinear mixing of the photons forming side-band frequencies). This patterned wave is a stationary solution of the cavity field equation.

Temporal Turing patterns in microresonators do have the comb-like optical spectra sought after for an OFC, however, it is critical to note that these structures specifically tend to be limited in bandwidth owing to the nature of the temporal patterns. The extreme robustness of these patterns generated on a compact platform makes them most suitable for applications requiring low-noise spectral lines [83]. Chapter 3 of this thesis presents results on the formation and stability of Turing patterns in a microresonator-filtered fibre laser.

There is, however, another class of dissipative structures in these systems that are more suited to the requirements of optical atomic clocks - cavity-solitons, that I will introduce,

and describe in the following section.

1.3.1 Cavity-solitons

Solitons have been studied and observed in a wide range of physical contexts, where there is a counter-balancing between dispersive and nonlinear effects. Optical solitons may form in the electromagnetic field in a bistable nonlinear system, under the condition of coexistence, that is, two permitted stable states for a single setting of the global system [84] – one being a stable homogeneous solution of the field equation, and the other being a patterned, or modulated, stationary solution such as the Turing patterns described in the previous section. Dissipative solitons, then, are concentrated structures of light in dissipative systems that constantly and bi-directionally exchange energy with their environment to maintain stability [85]. Temporal dissipative solitons are well studied in established mode-locked lasers [85].

An important class of dissipative soliton are cavity-solitons (CSs) [84, 86]. Cavity-solitons have been sought after for decades, beginning with seminal works by Moloney [71], Firth [87], and Rosanov [88] among others. In particular, CSs refers to a class of *localised* dissipative structures which exist on top of a stable homogeneous background, unlike the dissipative solitons in lasers which intrinsically cannot be localised due to the long gain material recovery timescale [85, 89, 90]. Cavity-solitons are individually addressable and take their form solely from the global settings of the cavity, existing in a state of balance between the opposing effects of nonlinearity and dispersion (see Fig. 1.3(a)).

The first experimental demonstration of temporal CSs was by Leo *et al.* in 2010 [91]. By injecting a continuous wave (CW) laser into a long silica-fibre Kerr cavity, trains of localised pulses could be excited by a short pulse delivered to the passive fibre cavity. Such a system is known to support bistability between a homogeneous, stable solution and a modulated solution - a condition permitting the existence of CSs. The localised nature of these structures could be demonstrated by individually addressing the CSs, encoding binary information into the pulse trains. Subsequent works investigated this in further details as well as exploring a range of dynamics within the system, including spontaneous pulse emergence and dispersive waves [92–97]. The properties of the pulses in this case lend to applications such as signal processing and optical memory buffers [98].

It is important to notice that the passive fibre cavities in which CSs were observed here were several hundred meters long. For OFCs, the spectral lines of such pulses are too close to one another to be individually distinguishable. Additionally, the externally-driven fibre

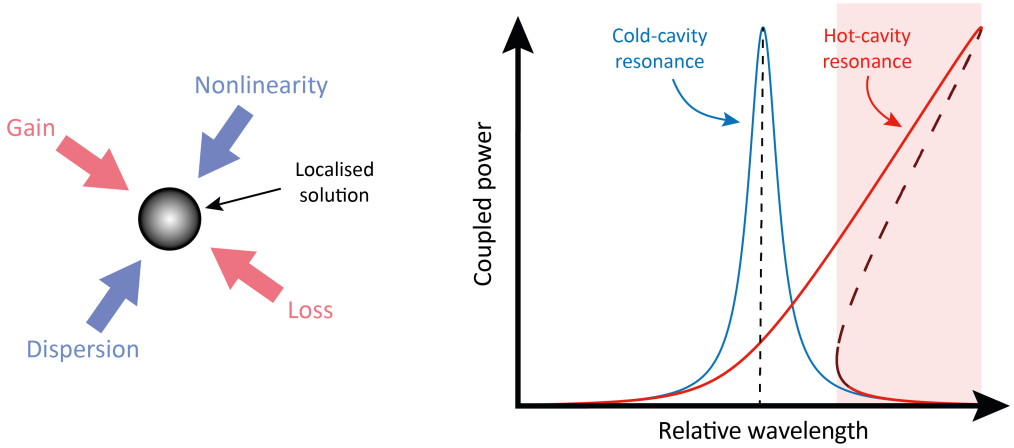

Figure 1.3: Left: Conceptual illustration of the localised soliton solution in a dissipative system. The opposing effects act to balance one another and manifest the localised solution. (b) Illustration of the power coupled to a single cavity resonance as the relative wavelength of an injected field is swept from low-high wavelengths. For an input power below the threshold of nonlinearity, the resonance is static (often termed the cold-cavity condition: the state when no light-induced effects are present - shown in blue). Above the threshold power, however, the resonance is shifted by the nonlinear response of the cavity (termed the hot-cavity condition: when the presence of light in the system significantly modifies the state via nonlinear effects - shown in red). The real and stable states are shown with the solid red line while the unstable state is depicted with the dashed line. It is clear that in the region highlighted with red shading, bistability exists (i.e. more than one stable solution for a fixed relative injection frequency). The asymmetry of the cavity resonance response, due to the focussing nonlinearity of the material, is illustrative of the critical role played by this relative detuning parameter in nonlinear cavity-systems.

loop does nothing to address the issues of compactness or lowing the energy consumption. In this context, the concept to apply the same physical principles, that were demonstrated in fibre-loops, to microcavities with a FSR in the range of 0.01 GHz to 1 GHz, was well acknowledged. Early works in the field had already demonstrated OFC generation in externally-driven monolithic micro-toroids [99], but it was not until after these developments in macroscopic fibre cavities that the field of CS microcombs was truly realised [81].

1.3.2 Temporal cavity-solitons in microcavities

Since the first experimental demonstration of CSs in microresonators [81], there have been numerous subsequent developments and demonstrations across a range of microresonator platforms [100–104]. More recently, alternative schemes to externally-driving the

microresonator with a CW laser have been developed [1, 105, 106], including even integrated devices [107, 108].

The CSs in micro-cavities, like their macroscopic equivalent, exist as a solution on top of a homogeneous CW field. The frequency spacing of the comb-teeth is sufficient that simple wavelength division multiplexers are entirely sufficient for selection of a single comb mode by the output, and the spectral bandwidth of the CSs can be extremely broad given the proper engineering of the micro-cavity [109], even without external spectral broadening. This broad bandwidth is well suited to optical atomic clocks, where it is desirable to create an octave-spanning spectrum, so that self-referencing for full stabilisation of the comb can be achieved. To this aim, external nonlinear broadening methods of the comb spectra are intensity-dependent and as such, a high peak power is essential, necessitating these ultrashort pulses, as compared to Turing patterns which have much smaller bandwidths and lower peak power. A further point is that lower repetition rates are generally desirable for electronic detection eventually, which are achieved by single soliton operation. Turing patterns on the other hand have repetition rates at some multiple of the micro-cavity FSR, as explored in Chapter 3.

There are, however, some significant and novel challenges for these conventional micro-comb devices. It is pertinent now to understand the conditions required for the generation of CSs in micro-cavities in order to address some of the fundamental limitations specifically.

The critical parameter in determining the emergent dissipative structure in these systems is the detuning of the driving field with respect to the central cavity resonance frequency [110–112]. Specifically, it can be shown that for a focussing nonlinearity the cavity-soliton region exists only for red-detuned driving fields, whereas Turing patterns can be permitted at blue-detuned frequencies [81]. Such behaviour can be understood by interpreting the 'folding-over' effect that is observed when measuring the intra-cavity power response of a microresonator as a function of the relative detuning of the driving field, with respect to the resonance centre (see Fig. 1.3(b)). It can be seen that for effectively red-detuned injected frequencies, due to the nonlinear response, there exists a point of bistability, where the coupled power has multiple solutions at a single relative frequency. This regime of coexistence is essential for the formation of CSs, and the role of this detuning parameter will be highlighted when identifying structured light regimes throughout this thesis.

To trigger the formation of CSs, it is not generally sufficient to simply turn-on the driving laser. The main technique used involves tuning the frequency of the driving laser into

the point of CS formation, with a specific speed and direction. This technique has been quite essential, greatly owing to the large thermo-optical effects, which are significant in these devices. Due to the the high field enhancement of the microresonator, detrimental thermo-optical nonlinearities induce a shift in the resonance frequency by affecting the refractive index [113–115]. In order to maintain the proper level of coupling of the external CW pump laser, a precise tuning has to be implemented to account for the magnitude and timescale of the thermal effects. In agreement with the predictions of the LLE, these temporal CS microcombs were found when the injected CW laser was red-detuned with respect to the cavity resonance frequency [81]. Further to this, the CS is not stable when formed due to the impact of these thermal effects. To maintain the CS, an active feedback system is essential. In essence, this lack of stability stems from the sign of the thermal nonlinearity in silica-based microresonators [116]. The sign of the thermo-optical effect acts to shift the resonance towards longer wavelengths. As such, intrinsically, any coupled field cannot thermally 'lock' at the red-detuned side of the resonance centre - the region in which CSs are permitted solutions.

There is a further fundamental limitation regarding the optical efficiency of these devices, an issue that is quite important in the context of creating compact optical sources. Physically, the CSs exist in bistability with the soliton state and a homogeneous state (the CW field), meaning there is always a background field in the cavity. For the case of so-called bright Lugiato-Lefever microcombs, this background constitutes more than 95 % of the total optical power, limited by the temporal overlap between the soliton pulse and the driving field of the CW laser that fills the entire cavity [117]. For portable low-power sources, improved optical efficiencies will be quite beneficial.

It is important to note that, for a practical OFC - especially in regard to optical atomic clocks, there must be some agile control of the comb in order to be able to lock comb lines to an optical source. To control the microcombs of LLE bright-soliton requires complex methods, with the CW pumping power and frequency being the control parameters. The CSs are accessible in a limited range, and as such, the control is limited for the realisation of a microcomb source for applications in optical clocks.

Finally, as already noted, the procedure for starting-up the microcombs systems is complex and requires a precise procedure to ensure CSs are excited. For all practical laser systems, it is important for usability that the laser turn-on process is reliable and robust. For the mature field of mode-locked lasers, elements are specifically integrated to the laser cavity to ensure the laser can start-up naturally from the off-state. If microcombs are to develop

into a mature technology, the limitation imposed by the complex start-up procedure will need to be addressed. In terms of the LLE, the limitation is quite fundamental. Since CSs exist in a region of bistability between two *stable* states, it is not possible to have a self-starting dynamic: this would require an initial instability to grow into a globally stable state. To progress the field of microcombs towards maturity, novel approaches to ensure robust self-starting behaviour will need to be developed.

It is clear that these aspects require a significant research effort to solve, and must be overcome for metrological applications of microcombs and to optical clocks in particular. Since some limitations are quite fundamental to the conventional microcomb scheme described by the LLE, it is clear that in order to overcome them, novel approaches must be conceived. Notably, the latest developments in fully integrated devices have seen soliton microcombs emerge in self-injection locked (SIL) schemes, where the externally driven microresonator is coupled, via light back-scattered from the waveguide-microresonator interface, directly to the driving laser cavity. This SIL approach has yielded battery powered combs [107, 108], and even very recently turn-key combs [118, 119] in which the laser is turned on and directly enters into the soliton regime. Although promising, the low power output per comb mode (sub-µW) and the lack of agile comb mode spacing still are significant limitations to optical atomic clock applications. Higher power comb outputs are often then dominated by thermal instabilities, which destroy the soliton state. A novel approach to address this issue is the use of an auxiliary CW laser, in addition to the driving field, which acts to stabilise the system [120]. The added complexity of a two laser system will inevitably increase the size of any such device, but this approach to stabilisation against thermal instabilities has been implemented successfully. Towards portable OFC devices that can completely meet the requirements of optical atomic clocks, further innovation is certainly required.

1.4 The future of cavity-soliton microcombs?

For inspiration, we can look to progress made in the realm of spatial CSs. Following from the discovery of spatial CSs, these systems were developed to integrate a gain material directly into the cavity. It was demonstrated experimentally that by including a gain medium inside the cavity, it is possible to excite a new class of CSs in a laser [121, 122]. The first prediction of '*Laser solitons*' dates to works of Rosanov [123] in the early 1990's. This new class of solitons, investigated theoretically in the spatial domain, were described as *'islands of lasing'* on a non-lasing background. Laser solitons are a distinct class of

localised pulse, appearing out of spontaneous emission noise in a phase invariant system, without requiring the presence of an injected driving field. In a waveguide-medium, these soliton pulses exist within a nonlinear amplifying media and bear no relation to the input pulse from which they can form, instead, having their shape determined by the parameters of the medium [124].

Experimentally, Laser CSs were demonstrated in the spatial domain by the groups of Giudici [121], and of Ackemann [122]. In both cases, a VCSEL acted as the spatially extended (i.e. a large Fresnel number) nonlinear amplifying media in which the laser CSs formed. The laser CSs were triggered spontaneously as the emitted power from the gain material is increased.

These lasers dramatically simplify the generation of CSs as well as improving their overall robustness. The homogeneous background state here is the trivial, or zero, solution of the system which implies that all of the energy is contained in the CS itself - a vast improvement to the inefficiencies of previous systems. The phase-invariant nature of these pulses also allows for a more simplified and versatile control for writing the CSs into the system, which would be necessary for a spatial optical buffer.

Following on from their works in spatial laser CSs [121], the group at Nice made the first experimental demonstration of laser cavity solitons in a temporal context [90].

1.4.1 Temporal laser cavity-solitons

It is interesting to consider whether the key components that enable the generation of laser cavity-solitons can be translated and applied to the time-domain microresonator-based system. In principle, directly integrating a gain medium into a nonlinear cavity should form the base of such a system.

The integration of a gain medium directly into a microresonator is a significantly challenging task, which has seen some attention [125, 126] and constitutes a significant technological effort. A more accessible scheme, requiring no such developments, would be to nest the nonlinear microresonator inside another amplifying fibre cavity. Such a scheme was proposed by Peccianti *et al.* in 2012, where a coherent pulsed regime was experimentally demonstrated [127]. Practically, the system comprises two coupled cavities (Fig. 1.4). The long main-cavity contains the amplifying gain fibre and any optical control elements that can be useful for diagnostics and polarisation control. The main-cavity loop is closed by nesting the microresonator, in add-drop configuration. In operation, the cavity will then sustain two coupled fields: one in the main-cavity, which experiences gain, and one

in the microresonator, which is subject to intense nonlinear effects. A well-studied system of equations for modelling coupled fields with nonlinearity and gain are the complex cubic-quartic Gintzberg Landau equations [128]. Indeed, for such a system of equations, soliton solutions are well-known and as such, this promising scheme constitutes an interesting framework with the potential to revolutionise the field of microcombs: combining rich physics of multi-mode fibre lasers with the intense nonlinearities of microresonators. More generally, chip-scale OFC sources have seen much development in the last 15 years [26]. Besides microresonator-based platforms, semiconductor lasers, electro-optic comb generators and supercontinuum generators have been receiving much attention. Quantum cascade lasers (QCLs) are electrically pumped semiconductor lasers which exploit intersubband transitions between various layers in an engineered stack, creating multiple levels of quantum well confinement. With the proper design, a population inversion between the subbands, which is required for lasing, can be achieved. Such devices have typically required active approaches to generate pulses, which are typically narrow bandwidth [129]. Very recent results indicate promising potential for cavity-solitons in injected ring-QCLs [130]. Electro-optic comb generators have highly tunable repetition rates compared with alternative approaches, although require external broadening and stabilisation to reach broadband operation [131]. Compared with these other platforms, microresonator-based OFCs, while excelling in miniature-scale, typically fall short due to their low optical efficiency and lack of tunability; both of these issues are directly addressed by our novel approach which will be explored in Chapter 2.

Overall, this thesis sets out to investigate the range of dynamical nonlinear regimes of this system.

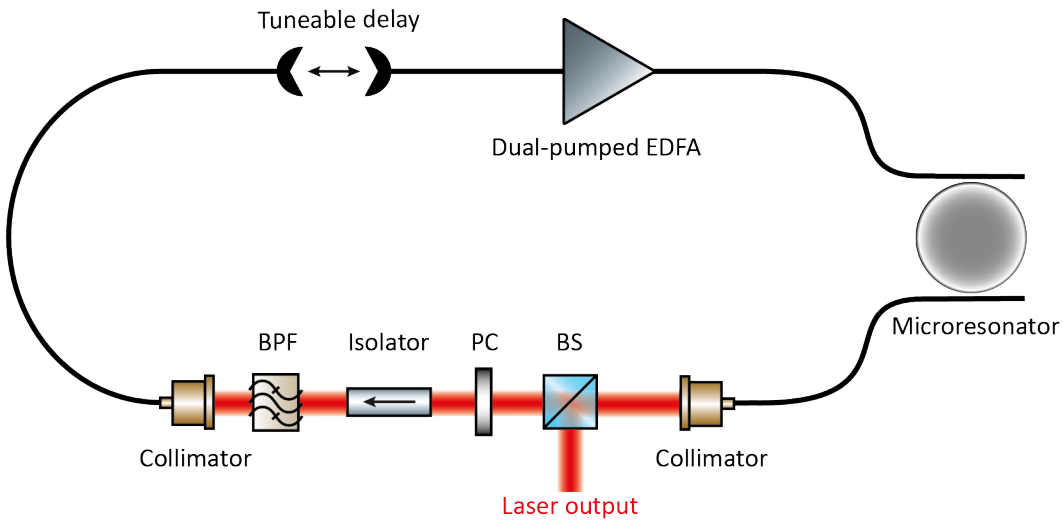

Figure 1.4: Schematic of the microresonator filtered fibre laser. The main fibre cavity (black line) contains the dual-pumped Erbium-doped fibre amplifier (EDFA), a tuneable delay section for adjusting the total optical main-cavity path length, and a free-space section (red-beam). The free space section allows for practical control over parameters of the system in the laboratory and contains a beam splitter (BS) for sampling the intra-cavity field; polarisation control elements (PC) for which we use zero-order half- and quarter-waveplates to control the polarisation and manage losses; an optical isolator to ensure unidirectional operation; and a bandpass filter (BPF) which acts to stabilise the laser operation. The microresonator is nested to close ends of the main-cavity fibres, in a four-port add-drop filter configuration. Practically, the main-cavity fibres are connected to some fibre/ waveguide in order to evanescently couple light from the main-cavity to the microresonator. All fibre components are polarisation-maintaining where possible - the exception is the short fibres directly coupling onto the microresonator chip.

1.5 Outline of the thesis

Chapter 2 presents the results of investigating the regime of localised pulses: laser cavity-solitons. This new class of temporal pulses, observed here for the first time, directly address some of the limitations that have thus far been prevalent in the field of micro-combs. Experimental results are presented along with a mathematical model for the microresonator-filtered fibre laser, and a novel approach to controlling the repetition rate of the microcomb (and as such the spacing of the spectral comb lines) is demonstrated. The optical efficiency of these laser cavity-soliton microcombs greatly exceeds the state-of-the-art. The contents of this Chapter have been published in "Laser cavity-soliton microcombs." *Nature Photonics* **13** 384-389 (2019) [1]. My contribution here was in the identification of steady-state soliton solutions with the numerical model and the numerical fitting of experimental data. I also supported the experiments and the interpretation of

the data.

Chapter 3 presents an investigation into another regime of pulsed laser operation in the microresonator-filtered fibre laser system: Turing patterns. The theoretical study of the system is extended with a comprehensive investigation into the start-up dynamics of the Turing regime. The cavity settings which determine the mode-spacing of the comb are explained. Experimentally, the high degree of stability of the spectral comb lines is investigated with a frequency non-uniformity measurement. The contents of this Chapter have been published in "Turing patterns in a fiber laser with a nested microresonator: Robust and controllable microcomb generation" *Physical Review Research* - **2**, 023395 (2020) [2]. My contribution here was in supporting the experimental activities, interpretation of the data, and the numerical fitting, as well as contributing to writing the manuscript.

Chapter 4 utilises a micro-rod whispering gallery mode resonator, with a very high Q-factor, in the microresonator-filtered fibre laser configuration. The strong thermo-optical nonlinearity of the microresonator in this setup is investigated and a novel self-pulsing operation is revealed. This study presents evidence of the dynamical role played by the thermal nonlinearity in this system. The contents of this Chapter have been published in "Thermo-optical pulsing in a microresonator filtered fiber-laser: a route towards all-optical control and synchronization." *Optics Express* **27**, 19242-19254 (2019) [3]. For this work, I devised and conducted the experiment, performed the analysis, and wrote the manuscript.

The work presented in **Chapter 5** builds upon the results of previous chapters to conduct an in-depth study into the laser cavity-soliton regime of the microresonator-filtered fibre laser. Here, the global conditions of the laser are examined to extensively map the cavity parameter space. Evidence supporting an additional mechanism to support the robust soliton state is presented. The spontaneous start-up mechanisms which govern the emergence of laser-cavity solitons from the laser off-state are investigated by real-time dispersive Fourier-transform measurement. The results pave the way towards a genuinely portable and robust microcomb laser. For the works in this Chapter, I have devised and conducted the experiments, performed the data analysis, and written the Chapter.

Chapter 2

Laser cavity-soliton microcombs

Micro-cavity-based frequency combs, or 'microcombs' [57, 58], have enabled many fundamental breakthroughs [74, 81, 91, 102, 132–146] through the discovery of temporal cavity-solitons. These self-localised waves, described by the Lugiato-Lefever equation [147], are sustained by a background of radiation usually containing 95 % of the total power [117]. Simple methods for their efficient generation and control are currently being investigated to finally establish microcombs as out-of-the-lab tools [148]. Here, we demonstrate microcomb laser cavity-solitons. Laser cavity-solitons are intrinsically background-free and have underpinned key breakthroughs in semiconductor lasers [90, 121, 122, 147, 149]. By merging their properties with the physics of multimode systems [150], we provide a new paradigm for soliton generation and control in microcavities. We demonstrate 50 nm-wide bright soliton combs induced at average powers more than one order of magnitude lower than the Lugiato-Lefever soliton power threshold [147], measuring a mode efficiency of 75 % versus the theoretical limit of 5 % for bright Lugiato-Lefever solitons [117]. Finally, we can tune the repetition rate by well over a mega-hertz without any active feedback.

2.1 Introduction

Optical frequency combs based on microcavity resonators, also called 'microcombs', offer the promise of achieving the full capability of their bulk counterparts, yet in an integrated footprint [57, 58]. They have enabled major breakthroughs in spectroscopy [132, 133], communications [134, 135], microwave photonics [136], frequency synthesis [137], optical ranging [138, 139], quantum sources [140, 141], metrology [102, 142] and astro-combs [143, 144].

Of particular importance has been the discovery of temporal cavity-solitons in microcavities [74, 81, 91, 145, 146]. Temporal cavity-solitons [58, 74, 81, 91, 117, 145–147] are an important example of dissipative solitons - self-confined waves balancing dispersion with the nonlinear phase shift in lossy systems [85]. Practical applications of these pulses for microcombs, however, still face significant challenges. In particular, they achieve a limited 'mode efficiency', defined as the fraction of optical power residing in the comb modes other than the most powerful one. Solitons in microcavities exist as localised states upon a background, usually a continuous wave (CW) [58, 74, 81, 91, 117, 145–147], which results in a dominant mode in the comb spectrum. In this configuration, described by the well known Lugiato-Lefever equation, bright solitons have a mode efficiency theoretically bounded to 5 % [117], limiting the efficiency of state-of-the-art microcombs based on this operating principle [58, 107, 117, 148].

Furthermore, controlling their fundamental parameters, such as repetition rate, has posed a challenge. Currently, tuning the repetition rate either requires complex methods involving fast detection, microwave signal processing and fast cavity actuation, or novel approaches such as pulsed [105, 144] or counter-propagating [151] pumping, or heterodyning with coupled microresonators [152]. Finding a solution to these fundamental issues has attracted significant research effort [107, 148].

Here, we demonstrate a distinct class of solitary pulses in microcombs - temporal 'laser' cavity-solitons - that directly addresses these challenges. Laser cavity-solitons [90, 121, 122, 147, 149] have been largely studied in spatial configurations such as semiconductor lasers [122], where they have enabled breakthroughs such as all-optical reconfigurable memories [149]. More recently, they have been observed in both temporal [90] and spatio-temporal [153] contexts. They are fundamentally different to externally driven cavity-solitons, which are sustained by the energy of the pumping background. Laser cavity-solitons, in contrast, receive energy directly from the gain of the lasing medium. As a result, they exist without any background light and are intrinsically the most energy-

efficient class of cavity-solitons.

By nesting a Kerr microresonator in a fibre loop with gain, we harvest the intrinsic capability of laser cavity-solitons, demonstrating that they can be used to achieve highly efficient, broadband microcomb generation. We excite bright solitons having a bandwidth of more than 50 nm, using average powers less than 6 % of the threshold for Lugiato-Lefever solitons in an equivalent resonator. Our background-free solitons have a mode efficiency of 75 %, with a theoretical maximum predicted to be 96 %. Furthermore, by exploring the properties of multimode systems, recently investigated for spatio-temporal mode-locking [150] and spatial beam self-cleaning [154], we show that the repetition rate of our pulses can be adjusted by reconfiguring simple parameters such as the laser cavity length. Without the use of an active control, we succeed in modifying their repetition rate by more than a megahertz.

2.2 Theoretical model

The principle of operation is shown in Fig. 2.1(a). A nonlinear micro-cavity (Cavity (a)) is embedded within a longer amplifying fibre cavity (Cavity (b)). The pulse propagating in the fibre loop, spectrally limited by the laser-gain bandwidth, sustains in the micro-cavity the existence of a pulse, which is broadened by the Kerr nonlinearity over the gain bandwidth [122, 155]. This architecture is inspired by the concept of a filter-driven four-wave mixing laser [127]. Our present analysis allows us to define the solitary state existence and understand the nature of previous observations [58, 127, 156]. In particular, we show that the relative position of the oscillating modes within the micro-cavity resonances is critical to realise this new class of broadband solitary pulses.

Temporal cavity-solitons can be effectively modelled using mean-field approaches, such as the Lugiato-Lefever equation [74], where the field in the micro-cavity is described as a pulse propagating in time, along with a spatial coordinate periodically looped within the microresonator length. Here, we build a set of multi-component (or 'vectorial') laser mean-field equations [150, 154] by coupling together the micro-cavity field with the main-cavity 'super-mode' fields. A super-mode is an optical radiation formed by a set of equally spaced modes of the main cavity, whose relative spacing (in frequency) is set by the micro-cavity free-spectral range (FSR) F_a. Quantitatively, the mth resonance $f_m^{(b)}$ of a super-mode can be linked to the micro-cavity resonances $f_m^{(a)}$ by the relation

$$f_m^{(b)} = f_m^{(a)} - (\Delta - q - m\delta)F_b \tag{2.1}$$

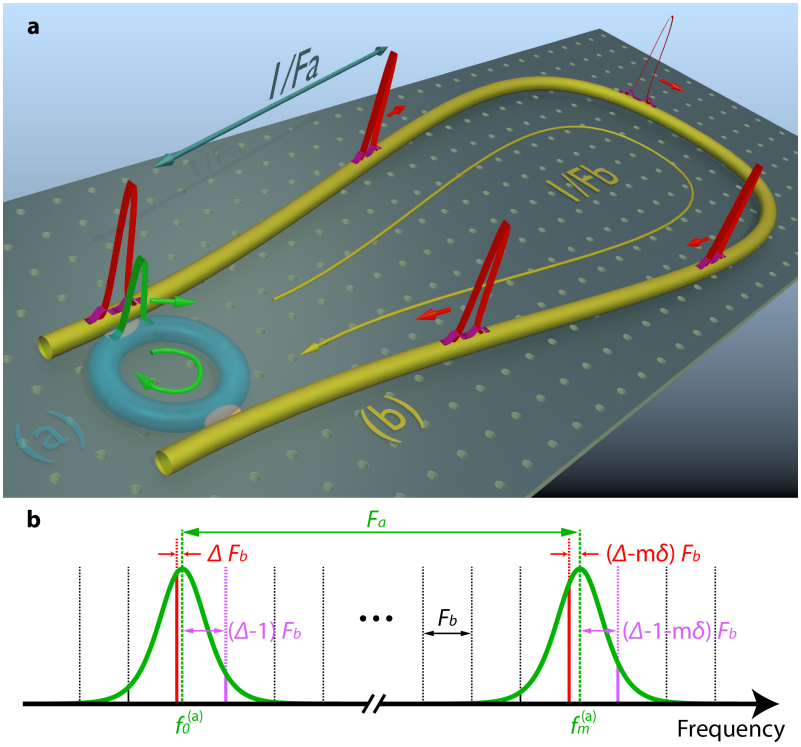

Figure 2.1: Principle of operation of microcomb laser cavity-soliton formation. (a) A short pulse (green) propagates in the micro-cavity (blue) sustained by a longer pulse (red) and a weak higher-order 'super-mode pulse' (purple) in the amplifying loop (yellow). This depicts the fundamental operation of a single soliton per cavity. (b) Cold-cavity spectral distribution. Micro-cavity resonances are depicted in green, amplifying-cavity resonances are in black, with leading and first-order super-modes highlighted in red and purple, respectively. The normalised frequency offset between the central frequency of the leading super-mode and the micro-cavity resonance is Δ; similarly, the frequency offset is $\Delta - 1$ for the central frequency of the first-order super-mode. In the convention used here and in Eq. 2.1, the positive values of Δ correspond to a leading order super-mode red-detuned with respect to the micro-cavity resonances. The variable δ is the normalised FSR detuning, appearing when the two cavities are not commensurate.

where F_b is the main-cavity FSR and q is an integer defining the order of the super-mode (Fig. 2.1). In general, the q-order super-mode is frequency-detuned with respect to the micro-cavity resonance by $(\Delta - q)F_b$, where Δ is the cavity-frequency offset, normalised against F_b. The key features of the laser are determined by the leading-order super-mode, defined for $q = 0$, which possesses the largest spectral overlap with the micro-cavity resonances. Higher-order super-modes ($q \neq 0$) typically experience greater coupling losses. Because F_b is not necessarily an integer divisor of F_a, we introduce the variable δ, normalised against F_b and representing the FSR detuning. Two numerical examples of linear and solitary propagation are reported in Fig. 2.2. We use a spatial coordinate periodically closed over the micro-cavity length because the temporal waveform of every

super-mode is periodic with the micro-cavity round-trip time T_a, with a period slightly detuned by δ (Eq. 2.1). Parameters $\Delta - q$ and δ play the role of the frequency and group velocity mismatches between the micro-cavity and super-mode fields. A key property of solitary waves in vectorial equations, also recently shown for spatio-temporal mode-locking [150], is that all the coupled fields 'lock' to a single group velocity (or repetition rate detuning) v (Fig. 2.2(a,b)) and carrier frequency offset ϕ (Fig. 2.2(c)). Practically, the system provides a well-defined soliton comb, with the nth frequency tooth $f_n^{(S)}$ expressed as

$$f_n^{(S)} = f_n^{(a)} + (\phi - nv)F_b \tag{2.2}$$

Parameters ϕ and v are dictated by Δ and δ, together with the normalised saturated gain g.

The main features of the laser can be obtained by a simple mean-field model that, in its normalised form, reads as

$$\partial_t a = \frac{i\zeta_a}{2}\partial_{xx}a + i|a|^2 a - \kappa a + \sqrt{\kappa}\sum_{q=-N}^{N} b_q, \tag{2.3}$$

$$\partial_t b_q = -\delta\partial_x b_q + \frac{i\zeta_b}{2}\partial_{xx}b_q + 2\pi i(\Delta - q)b_q + \sigma\partial_{xx}b_q + g b_q - \sum_{p=-N}^{N} b_p + \sqrt{\kappa}a \tag{2.4}$$

where a and b_q are the optical field envelopes for the microresonator and amplifying cavities, respectively, and are expressed as a function of the normalised propagation time t and space coordinate x. Here, we have considered a generic interaction with $2N+1$ super-modes b_q, for $|q| \leq N$; the mode with $q = 0$ corresponds to the leading mode. Note that every super-mode b_q is directly coupled with all the other super-modes by the term $\sum_{p=-N}^{N} b_p$, where p is an auxiliary index.

The time t accounts for the propagation over different round-trips and is normalised against the main-cavity round-trip $T_b = 1/F_b = 12.5\,\text{ns}$. The space coordinate x, defined for $|x| < 1/2$, is associated to the frame moving with the pulse and is normalised against the microcavity round-trip length, which corresponds to a round-trip time $T_a = 1/F_a$ =20 ps. The left- and right-hand sides of the equations contain the conservative and dissipative terms: $\zeta_{(a,b)} > 0, \Delta$ and δ are the normalised coefficients for the cavity (anomalous) dispersions, the cavity-frequency offset and the group velocity mismatch. The latter term considers the effective FSR detuning between the two cavities as in Eq. 2.1; κ, g and σ represent the coupling, saturated gain, and bandwidth of the spectral filtering, respectively.

Specifically, the normalised coupling parameter is $\kappa = \pi \Delta F_A T_b \approx 2\pi$, being the microcav-

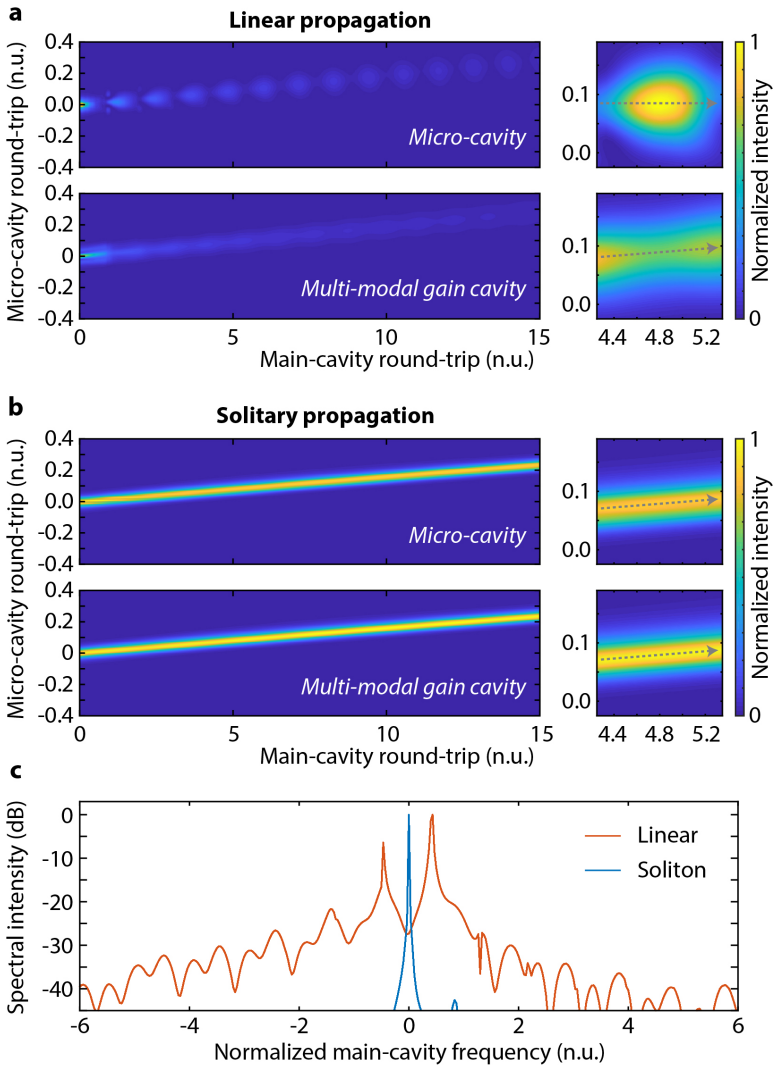

Figure 2.2: Theoretical propagation of linear and solitary pulses. The micro-cavity and gain cavity have a group velocity mismatch of $\delta = 0.03$. In these examples we used $\Delta = 0.47$ and $g = 0.14$. The number of super-modes used in the simulations is 61, as defined in Eqs. 2.3 and 2.4. (a) Evolution of the micro-cavity and multi-modal amplifying-cavity fields in the linear case, in normalised units (n.u.). The quantities in the upper and lower panels are the overall field intensities in the two cavities $|a(t,x)|^2$ and $\sum_{-N}^{N} |b_q(t,x)|^2$ (with reference to Eqs. 2.3 and 2.4). The group velocity of the fields is better shown in the insets, where the direction of the field is marked with an arrow. The mismatch between such group velocities causes a periodical decoupling of the fields. (b) Solitary propagation: both fields lock to the same group velocity v. (c) Equivalent spectral distribution of the super-modes within a resonance of the micro-cavity. Such a spectrum, for the linear case (orange), highlights the presence of several frequency components, one for every super-mode with frequency offset $\Delta - q$. In the case of solitary propagation (blue), conversely, all the modes lock to the frequency ϕ.

ity linewidth ΔF_A approximately twice the FSR of the main cavity (in the experimental

condition). The normalised dispersions are $\zeta_{(a,b)} = -\beta_{(a,b)}\nu_{(a,b)}T_b/T_a^2$, where $\nu_{(a,b)}$ and $\beta_{(a,b)}$ are the group velocities and group velocity dispersions of the two cavities, respectively. In the simulations, we used $\zeta_a = 1.25 \times 10^{-4}$ and $\zeta_b = 3.50 \times 10^{-4}$, obtained with $|\beta_a| \approx -20\,\mathrm{ps^2\,km^{-1}}$ and $|\beta_b| \approx -60\,\mathrm{ps^2\,km^{-1}}$ (within our experimental constraints). We used a gain bandwidth $\sigma = (2\pi T_a \Delta F_F)^{-2} \approx 1.5 \times 10^{-4}$, based on a 650 GHz intracavity spectral filter. The gain g, considered as the saturated gain of the amplifier, is normalised against the main-cavity length and, together with Δ and δ in Eq. 2.1, is an adjustable parameter in our numerical data sets.

The stationary states are defined as $a(t,x) = a_S(x - vt)\exp[-2\pi i\phi t]$, $b(t,x) = b_{q,S}(x - vt)\exp[-2\pi i\phi t]$, where the normalised frequency offset ϕ and the normalised velocity v are as in Eq. 2.2. Solitary solutions are found by numerical continuation considering 11 super-modes (that is, with $N = 5$), while stability is investigated with linear perturbation analysis and propagation considering 61 super-modes (that is, with $N = 30$).

2.3 Experimental results

Figure 2.3 reports the experimental setup. To characterise the microcomb, we use its optical spectrum, the temporal autocorrelation obtained with a second harmonic non-collinear autocorrelator, and the radio-frequency spectrum of the intensity, that allow us to evaluate the quality of the laser amplitude. We used intra-cavity laser-scanning spectroscopy [157] (Figs. 2.3 and 2.4(b,d,f)) to measure the frequency of the oscillating modes and their position within the micro-cavity resonance, obtaining important insights into the solitary nature of the solution. The laser-scanning spectroscopy measurement enables us to extract highly accurate information on the position of the microcomb lines, which is obtained by beating the microcomb with an external scanning CW laser. Such a CW laser is swept in time and its beating with the microcomb is read on an oscilloscope, providing the position of the comb lines. The axis of the oscilloscope is calibrated by beating the scanning CW laser against a reference comb [157]. The scanning laser is also propagated in a Mach-Zehnder interferometer, with an FSR of ∼6.95 MHz, to provide an accuracy on the frequency scale below the MHz level. This approach allows extracting, with high accuracy, the frequency distances between the microcomb lines.

To gain information on their relative position with respect to the microresonator resonances, the CW scanning laser can be coupled directly into the microresonator, as in Ref. [157], where this same approach was used in an external pumping microcomb configur-

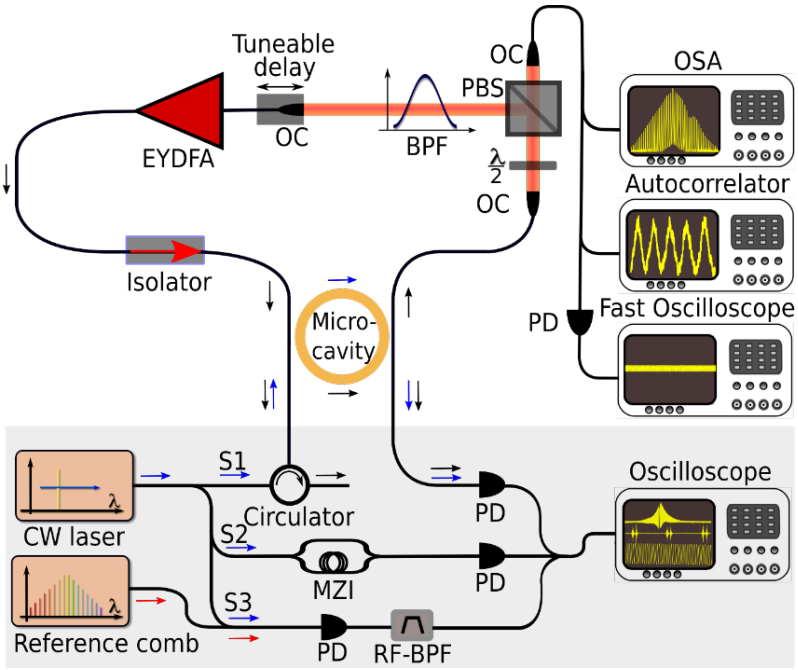

Figure 2.3: Experimental setup for microcomb cavity-solitons' generation and laser-scanning spectroscopy detection of a hot resonator. The setup is composed of a nonlinear microresonator, an erbium-ytterbium co-doped fibre amplifier (EYDFA), an optical isolator, an optical bandpass filter (BPF), a tunable delay line, a half-wave plate ($\lambda/2$), a polarising beam splitter (PBS) and two optical collimators (OCs). The output signals from the rejection port of the polarising beam splitter were detected with an optical spectrum analyser (OSA), an autocorrelator, and a fast photodetector (PD) connected to an oscilloscope. For the laser-scanning spectroscopy, a scanning CW laser was split into three signals, S1, S2, and S3. S1 was used to probe the resonances' profile and oscillating microcomb lines in the hot microresonator, while S2 and S3 were simultaneously used to perform frequency calibration. This was achieved by beating the external CW source with a reference comb (Menlo Systems, 250 MHz repetition rate). The resulting signal was passed through a radio-frequency bandpass filter (RF-BPF) before detection. In this way, it was possible to generate a set of calibration markers with a spacing of ~250 MHz. We created an additional set of finer markers by coupling the signal S2 to an unbalanced Mach-Zehnder interferometer (MZI) with an FSR of ~6.95 MHz.

ation. In our case, the CW laser cannot be propagated together with the microcomb, because it would be also injected into the amplifier, destabilising the system. For this reason, we characterise the small backscattered signal in the microresonator, which is expected to be equivalent to the microcomb oscillation. To achieve this, the CW scanning laser is coupled counter-propagating within the micro-cavity, as shown in Fig. 2.3. The measurements of laser cavity-soliton microcombs at different intra-cavity powers are presented in Fig. 2.4(a-f). The spectra exhibit a bandwidth of up to 50 nm - comparable to the cavity-solitons observed in resonators with similar dispersion properties [117, 138,

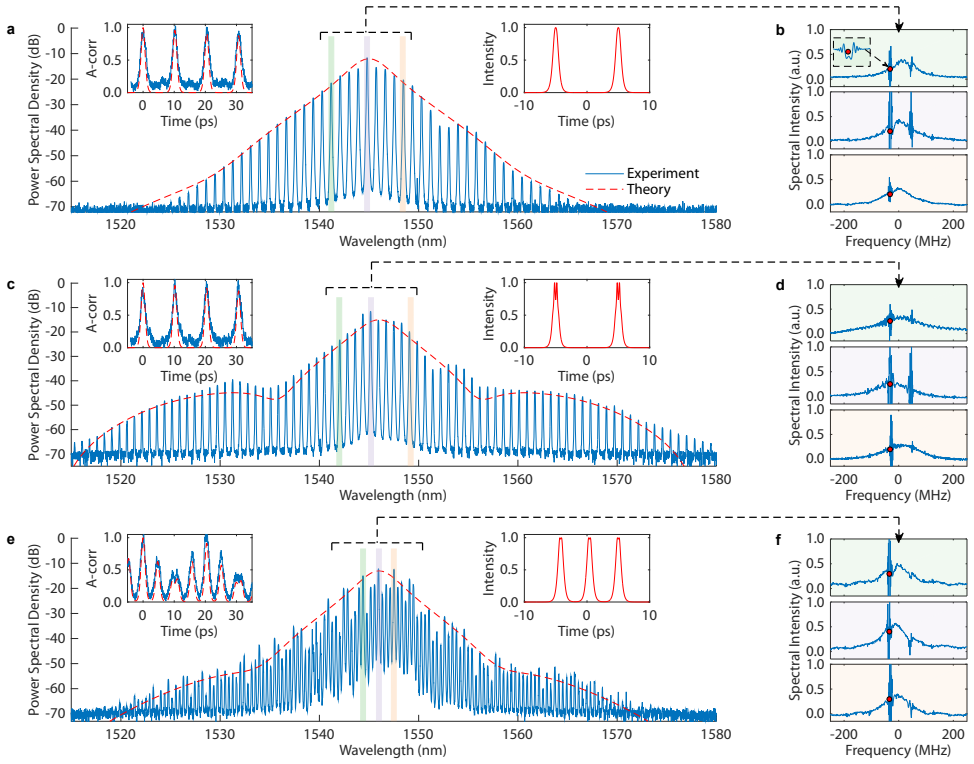

Figure 2.4: Temporal laser cavity-soliton measurement. (a) Soliton generation, for two equidistant solitons per round-trip. The intra-cavity power at the output of the amplifier is 100 mW and at the output of the micro-cavity is 20 mW. Spectrum (in logarithmic scale) and autocorrelation (A-corr, left inset) with measurements (blue) and theoretical solitary state (red). Fit parameters are $\Delta = 0.49$ and $g = 0.1$, resulting in $\phi = -0.475$, corresponding to a red-shifted frequency of 35 MHz (Eq. 2.2). Right inset: theoretical intensity. (b) Intra-cavity spectrum (blue), showing within each micro-cavity resonance the lasing modes (red dots, red-shifted by ∼32 MHz from the resonance centre). The three plots correspond to the wavelengths highlighted in (a) by coloured shading. (c, d) The same measurements at higher fibre gain for two equidistant solitons per round-trip, leading to a 150 mW intra-cavity power at the output of the amplifier and 30 mW at the output of the ring. Here, $\Delta = 0.47$ and $g = 0.14$, with $\phi = -0.474$. (e, f) The same measurements for three solitons per round-trip. The intra-cavity power is the same as in case (c,d). Here, $\Delta = 0.49$ and $g = 0.11$, with $\phi = -0.474$. The autocorrelation shows that the solitons are not equidistant, highlighting the localised nature of the solution.

145] - and, together with the corresponding autocorrelations (Fig. 2.4(a,c,e) and inset), are in excellent agreement with theory.

The spectrum of the stationary states, found using the model described in Eqs. 2.3 and 2.4, can take the form of a classical sech-like, triangular shape, as in the cases shown in Fig. 2.4(a,b). Different spectral shapes are, however, possible. For instance, the spectrum

in Fig. 2.4(c,d) shows lateral wings. This feature can be qualitatively related to the MI on the peak of the pulse, shown in the theoretical pulses depicted in the right inset in Fig. 2.4(c).

In general, the bandwidth of the soliton increases with the gain. This can be seen by comparing the experiments in Fig. 2.4(a-d). Both measurements feature two solitons per cavity. The experiments in Fig. 2.4(c,d) have been performed at higher fibre gain and the soliton has a larger bandwidth. The measurement in Fig. 2.4(e,f) has the same intracavity power as in Fig. 2.4(c,d), although it highlights the presence of three solitons in the cavity. Because there is an additional soliton in the cavity, the energy per soliton is lower than the case in Fig. 2.4(c,d), leading to a narrower spectrum.

The theoretical normalised soliton frequency in Fig. 2.4(a,b) is $\phi = -0.475$, corresponding to a red-shifted frequency of 36 MHz. This value can be calculated with Eq. 2.2 using the FSR of the main-cavity, $F_b = 77$ MHz. The calculated red-shifted frequency is in excellent agreement with the lasing mode measured by intracavity laser-scanning spectroscopy in Fig. 2.4(b), which is red-shifted by $\sim$32 MHz from the centre of the microcavity resonance. Similar agreement is also obtained for the measurements displayed in Fig. 2.4(c-f).

A bistable system can display both localised and non-localised coherent waves [147]. Solitons are localised states that can appear in groups of non-equidistant pulses, such as the triplet seen in Fig. 2.4(e-f). The stability of their tails requires stability of the background, which is theoretically expected for oscillating modes that are red-detuned with respect to the micro-cavity resonance (Fig. 2.7(a)). These facts are in excellent agreement with the measurements shown in Fig. 2.4(b,d,f). We attribute the small, blue detuned mode found only in the central resonance to a perturbation on the soliton tails, against which localised pulses are robust.

This measurement allows us to highlight another difference of our system supporting laser cavity-solitons with respect to the Lugiato-Lefever system. As observed before, the Lugiato-Lefever equation is a driven system. All the waveforms in the microcavity are necessarily locked to the frequency of the input laser, both for solitons and perturbations. Because our system is homogeneous, conversely, the oscillating frequency is a characteristic of the solution. Solitons and their perturbations have, for this reason, different frequencies. To better explain this point, here we report a numerical example where we inject into the system a waveform consisting of two or three solitons, as observed for the experiments in Fig. 2.4. We tested the propagation of the calculated solution which matches the experiments for $\Delta = 0.49, g = 0.1$; for $\Delta = 0.47, g = 0.14$; and finally, for $\Delta = 0.49, g = 0.11$

corresponding to the cases of Fig. 2.4(a), (c), and (e) respectively. The propagations are reported in Fig. 2.5(a), (d), and (g) to better visualise the low energy component of the solution.

Figure 2.5(b), (e), and (h) report an evaluation of the effective propagating frequency (normalised, as the detuning Δ, against the main-cavity FSR) at the peak ($x = -0.25$, blue line) and at the minimum ($x = -0.5$, orange line) of the propagating intensity. Such a spectrum is calculated as the Fourier transform [1] along the propagating slow axis t at those specific x. The frequency axis ξ is centred along the soliton frequency ϕ. This approach reveals the radio-frequency spectrum of the solution and it is also used for the examples of Fig. 2.1, allowing to visualise the presence of unlocked higher-order super-modes.

Here, the numerical analysis shows that, in both cases, injecting the stationary states into the system also excited a very small background. The unlocked high-order super-modes are found in such a background, while are absent on the peak of the solitons. Although such a background fades away in propagation because the solitons are stable in such a range of parameters, this analysis shows that the perturbations of the background can coexist with solitary propagation. Very interestingly, this calculation also highlights that the solitary states are very robust to perturbations on their tails.

Because such unlocked components are excited around the cold cavity frequency of the leading order mode ($\xi = -0.05$) and first-order ($\xi = -1$), which are the two dominating super-modes of the interaction, we could find a direct frequency match with the experimentally observed radio-frequency spectrum and laser-scanning spectroscopy measurement. Considering that the frequency axis ξ is normalised against the main-cavity FSR F_b =77 MHz, the cold cavity frequency of the leading order mode ($\xi = -0.05$) and first order ($\xi = -1$) mode correspond to approximately 4 MHz and 77 MHz respectively.

The weak beat-notes in the radio-frequency spectrum can be then attributed to a perturbation of the background. Such a perturbation has frequency components well distinct by the soliton frequency. Specifically, in our experimental cases, we found a perturbation on the first order super-mode (−20 dB component at 77 MHz in Fig. 2.5(c), (f), and (i)). This perturbation is also visible in the laser-scanning spectroscopy measurement which reveals a small, blue-detuned frequency found in the central resonances, yet absent in the comb wings of Fig. 2.4(b),(d), and (f). Figure 2.5(f) also shows the presence of a perturbation on the leading order super-mode (−20 dB component at 6 MHz). Conversely to the red-detuned solitons, coherent patterns are non-localised, periodic waves that fill the entire

[1] Formally, $\tilde{a}(\xi, x) = \int a(t, x) \exp[-2i\pi\xi t] dt$ where ξ is the propagation (slow) frequency axis.

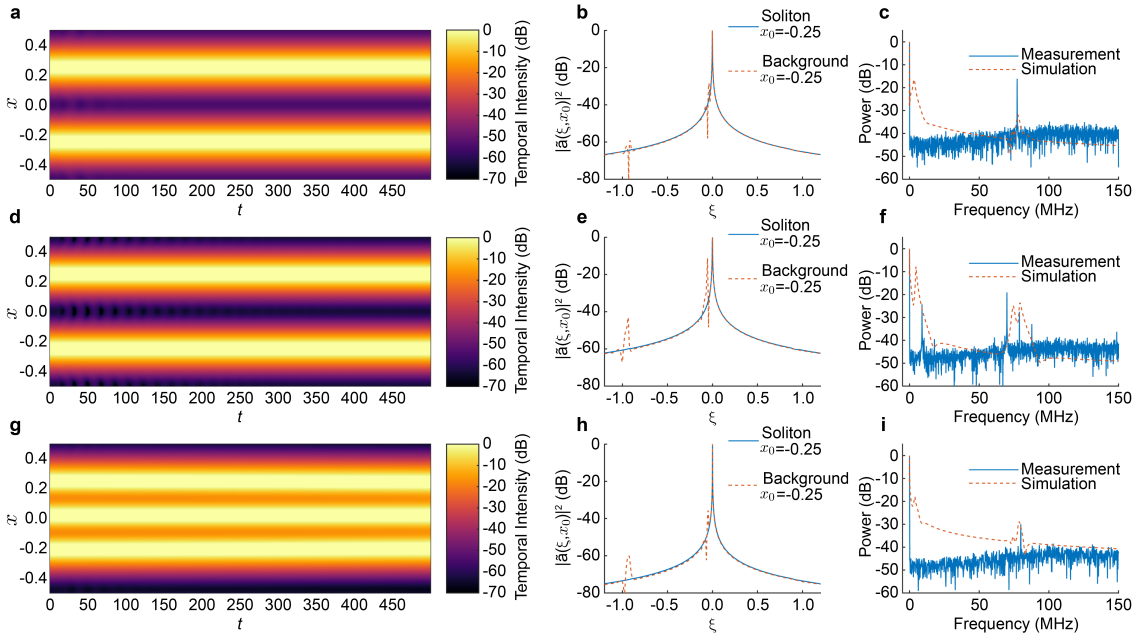

Figure 2.5: Experimental propagation of soliton pulses. Here, $\zeta_a = 1.25 \times 10^{-4}, \sigma = 1.5 \times 10^{-4}, \kappa = 2\pi$. We have $\Delta = 0.49, g = 0.1; \Delta = 0.47, g = 0.14$; and $\Delta = 0.49, g = 0.11$ for (a-c); (d-f), and (g-i), respectively. (a) Propagation of two soliton pulses, the intensity is displayed in false colours and logarithmic scale to better visualise the spectrum low energy components. (b) Slow temporal scale (radio-frequency) spectra obtained as the Fourier transform $\tilde{a}(\xi, x_0) = \int a(t, x_0) e^{-2\pi\xi t} dt$ of the propagating solution at the peak (blue, $x_0 = -0.25$) and at the tail (orange, $x_0 = -0.5$) of the pulse along the propagating time axis. Note that the spectra are normalised to obtain a maximum at 0 dB. The frequency axis is normalised with respect to the main-cavity FSR. (c) Comparison of the experimental radio-frequency spectrum (blue) with the background radio-frequency spectrum calculated in the simulations as $\tilde{a}(\xi, x_0) = \int |a(t, x_0)|^2 e^{-2\pi\xi t} dt$.

cavity. Type I and II combs in the Lugiato-Lefever system [58] are characteristic examples of patterns that typically have a narrower bandwidth than solitons. Earlier observations [58, 127, 156, 158], limited to picosecond pulse durations and displaying type I [156] and II [158] comb shapes, are consistent with this picture. Furthermore, laser-scanning spectroscopy measurements [158] on these types of pulses reveal blue-detuned modes, for which the theory forbids stable solitons while allowing patterns originating from the modulational instability of the background state [147].

Figure 2.6 reports a set of stable, coherent states with a narrower spectral bandwidth. This kind of state can be obtained in the same setup used for generating solitons. To reproduce the experimental conditions of Refs. [127, 156], which employed a narrower passband filter in the setup, we used a passband filter with a 6 nm bandwidth. Similar to Ref. [156], we observe states at multiples of the repetition rate, with comb lines from

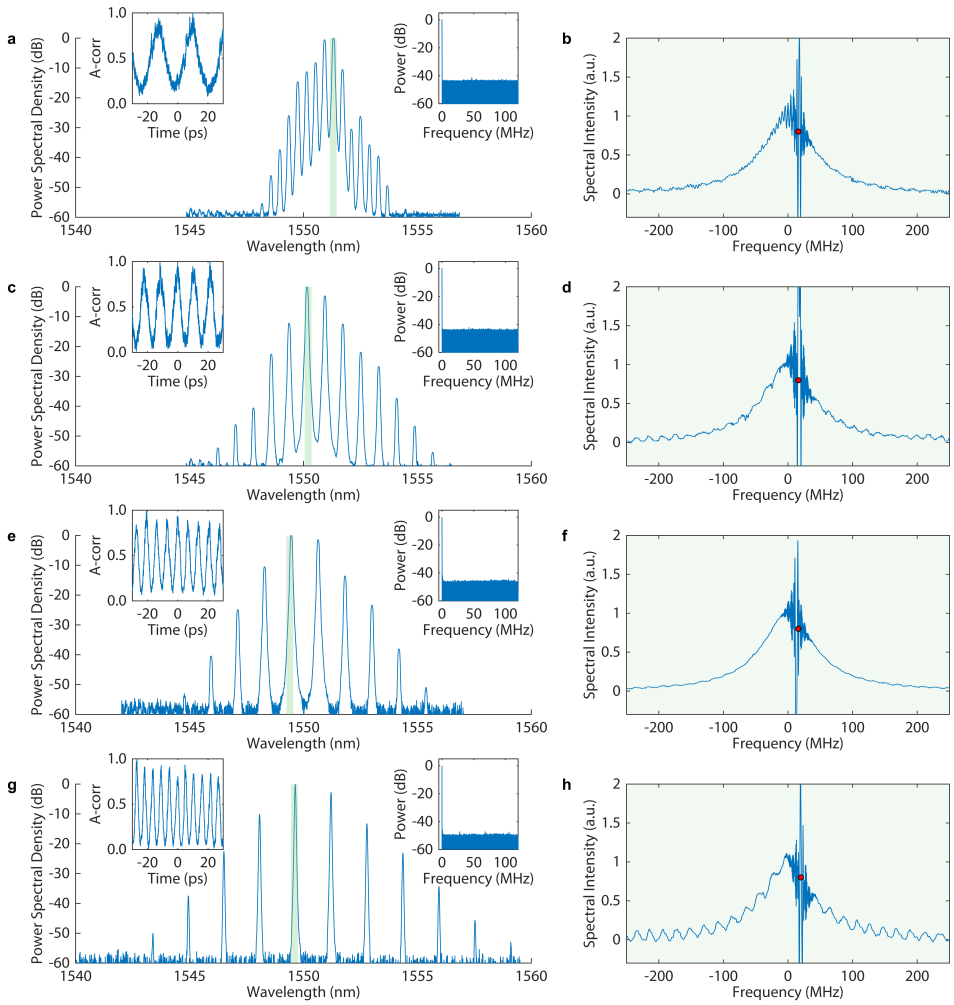

Figure 2.6: Stable non-localised states. Coherent state obtained with a setup similar to that of Refs. [127, 156]. States with different FSR are obtained by adjusting the cavity length with a similar procedure to that used in Refs. [156, 158]. (a) Optical spectrum, autocorrelation (left inset) and radio-frequency spectrum (right inset) of a coherent state at repetition rate equivalent to a single microring FSR (approximately 50 GHz). (b) Laser-scanning spectroscopy measurement for the most powerful spectral line, marked by a green line in panel (a). The measurement clearly shows a blue-detuned oscillation (c, d) Same measurement as in (a,b), for a coherent state at the repetition rate twice the microring FSR (approximately 100 GHz). (g,h) Same measurement as in (a,b), for a coherent state at a repetition rate equivalent to four-times the microring FSR (approximately 200 GHz).

one to four FSRs apart. Such states have been obtained for different main-cavity lengths, with a similar procedure to Refs. [156, 158]. The autocorrelation shows a very low background which, together with the clean radio-frequency spectrum, indicates the coherence of the state. The intracavity laser-scanning spectroscopy of the most powerful, central

lines shows that they oscillate in a blue-detuned position with respect to the microcavity resonance. A more detailed analysis of these non-localised states is presented in Chapter 3.

Our experiments demonstrate the inherently higher efficiency of laser cavity-solitons compared to Lugiato-Lefever solitons, which feature a dominant comb mode (located at the pump wavelength) comprising the energy of the CW background (Fig. 2.7(b,c)). For Luigato-Lefever solitons, the mode efficiency has a theoretical limit of 5 % and 50 % for bright and dark solitons, respectively [117]. Our mode efficiency in the experiments of Fig. 2.4 is greater than 75 % for bright solitons. Furthermore, we theoretically predict a maximum mode efficiency of 96 % for bright laser cavity-solitons. This contrasts with state-of-the-art devices based on bright Lugiato-Lefever solitons, which have mode efficiencies on the order of 1.6 % to 5 % (refs. [107, 117]). Lugiato-Lefever solitons feature a minimum power excitation threshold above which the Kerr nonlinearity induces bistability, yielding the two CW states necessary for the solitons existence (Fig. 2.7). Our laser cavity-solitons, in contrast, require a zero background with a single CW state and exist below the Kerr bistability threshold. By comparing experiments with theory, we find that the peak powers injected into the micro-cavity are, in our case, below 50 % of the input power threshold of a Lugiato-Lefever soliton for the same microresonator. Because our injected field is pulsed, the input average power to the microresonator is less than 6 % of this threshold power.

The input average power to the microresonator, calculated as $\sum_{q=-N}^{N} \int |b_q(x)|^2 dx$ from the numerical fitting in Fig. 2.4(a) and 2.4(b) is 3.1 and 3.8 for the two cases, respectively. Compared to the formation threshold of Lugiato-Lefever bright solitons $8/(3\sqrt{3})\kappa^2 = 60.8$, they represent a fractional power of 5.1 % and 6.3 %, respectively. To demonstrate the capability of changing the soliton repetition rate using simple methods, we varied the main-cavity FSR detuning δ with a delay line that modified the fibre cavity length and, hence, the mode spacing F_b. Gain and loss were also adjusted to maintain the solitary state. Figure 2.8 shows the variations in the repetition rate for the three cases (Fig. 2.8(a)). We measured the frequency position of the comb modes against the mode number using laser-scanning spectroscopy. We then calculated the best fit for the first case (comb 1) and subtracted the frequency positions for the three cases, obtaining the residual frequency versus mode number in Fig. 2.8(b). This shows a change in the repetition rate of over a megahertz. The theoretical results (Fig. 2.8(c)) demonstrate that, by changing δ within the experimentally achievable range, the soliton stability is maintained while its velocity

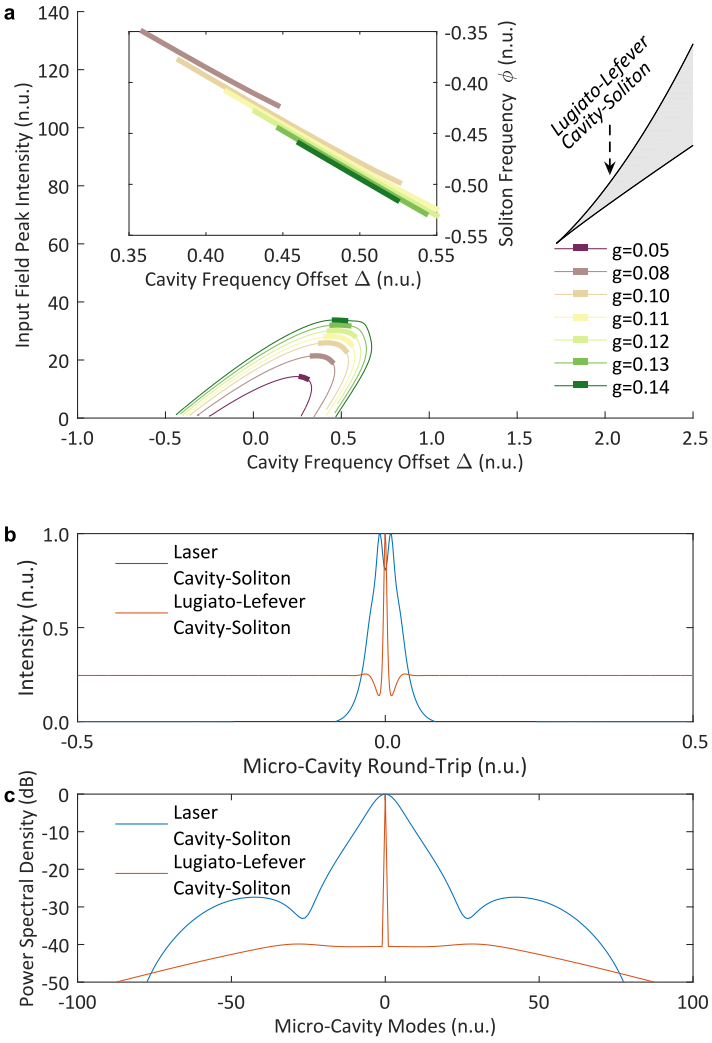

Figure 2.7: Temporal laser cavity-soliton and Lugiato-Lefever cavity-soliton comparison. (a) Plot of laser cavity-soliton input field peak power versus normalised offset Δ, calculated for various gain values ($g = 0.05$ to 0.14 for plots from purple to green). Thick lines mark the stable self-localised solutions, both in the main graph and the inset, where the soliton frequency ϕ is reported. Note that negative values of ϕ correspond to frequencies red-shifted with respect to the micro-cavity centre, in agreement with the experiments. The grey area marks the region of existence for Lugiato-Lefever bright solitons. (b) Intensity profile on the micro-cavity for a laser cavity-soliton ($\Delta = 0.47$ and $g = 0.14$, blue line) and a Lugiato-Lefever cavity-soliton at the power threshold (orange line), highlighting the presence of a strong background in the latter case. (c) Spectrum of the theoretical cases in (b). The strong background of the Lugiato-Lefever cavity-soliton results in a dominant comb mode at the centre of the spectrum. Laser cavity-soliton lines generally possess a higher power spectral density.

is modified, thus varying the repetition rate.

We achieved these localised states by manual adjustment of the fibre cavity parameters, such as cavity length, gain current and polarisation losses, in a similar fashion to passively mode-locked lasers. This approach enables the use of versatile methods, such as genetic algorithms, that have been instrumental in achieving adaptive control of the soliton properties and self-starting operation in passive mode-locking [159].

In conclusion, we report the observation of temporal laser cavity-solitons in optical microcombs. Our results merge the rich physics of optical Kerr microcombs and their ability to generate large bandwidths with the unique properties of laser cavity-solitons and multimode systems. In contrast to conventional coherently driven cavity-solitons, this new class of cavity-solitons is intrinsically background-free, making them extremely energy efficient. Furthermore, thanks to a tailored two-cavity configuration, crucial properties such as the repetition rate, can be controlled with simple elements such as a delay line. Such critical control of these properties is more akin to the control elements of conventional OFC sources. Compared to these tabletop devices, which consume more than 500 W and have repetition rates in the range of 250 MHz, microcombs look to provide a much more portable solution. Practically, a microcomb repetition rate in the range of 10 GHz is desirable for electronic detection, and such sources have indeed been successfully fabricated. Future work will be done to demonstrate the stability of laser cavity-solitons. Laser cavity-solitons represent a new and powerful mode of operation for microcombs, offering many advantages that will help these devices to move out of the laboratory towards real-world applications.

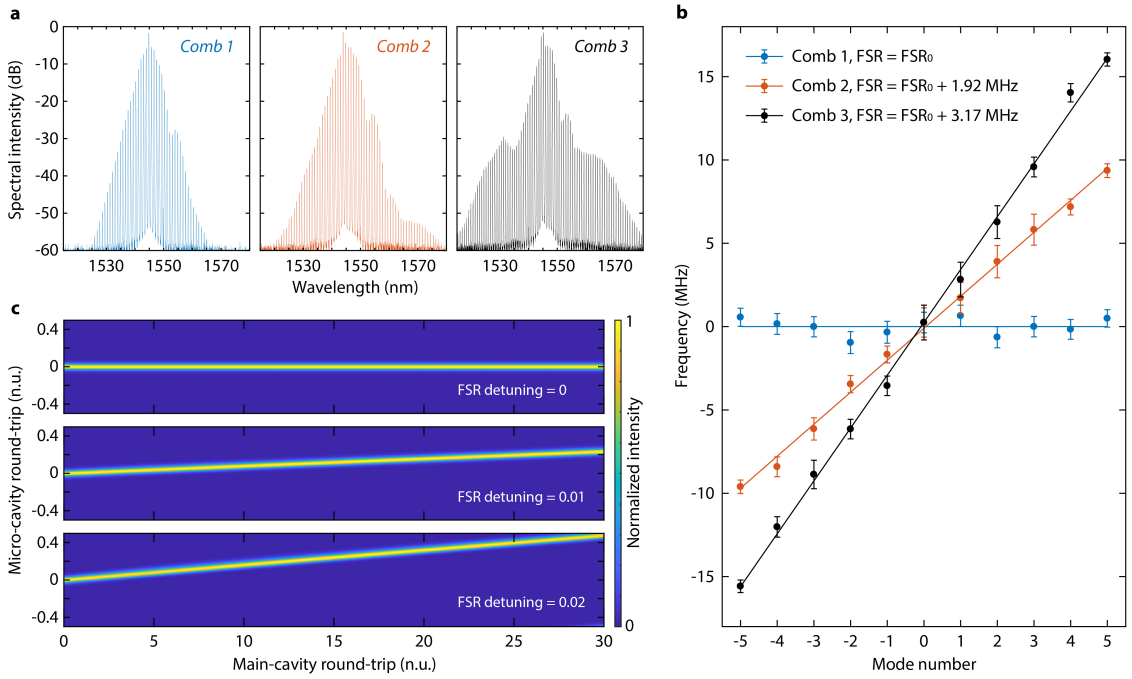

Figure 2.8: Control of the repetition rate of temporal laser cavity-solitons. (a) Specta for three combs as the fibre cavity length is changed within a broad range of 150 µm. Gain and losses have been readjusted to maintain the solitary state showing two equidistant solitons per round-trip. Intra-cavity powers are 20 (blue), 25 (orange), and 30 mW (black), respectively. (b) Residual frequency shift against mode number with respect to the best fit for the comb 1 case (blue). Error bars are defined as the size (10 %–90 %) of the slope associated to the Hilbert transform phase in the laser-scanning spectroscopy interferogram. Combs 2 and 3 show a change in FSR and, hence, repetition rate variations of 1.9 MHz and 3.2 MHz with respect to comb 1. (c) Calculated propagation of a stationary solitary solution when $\Delta = 0.49$ and $g = 0.1$, for $\delta = 0$, 0.01 and 0.02. The solitary wave is maintained in all three cases.

Chapter 3

Turing Patterns in a microresonator-filtered fibre laser: robust and controllable microcomb generation

Microcombs based on Turing patterns have been extensively studied in configurations that can be modelled by the Lugiato-Lefever equation. Typically, such schemes are implemented experimentally by resonant coupling of a continuous wave laser to a Kerr micro-cavity in order to generate highly coherent and robust waves. Here, we study the formation of such patterns in a system comprised of a micro-resonator nested in an amplifying laser cavity, a scheme recently used to demonstrate laser cavity-solitons with high optical efficiency and easy repetition rate control. Utilising this concept, we study different regimes of Turing patterns, unveiling their formation dynamics and demonstrating their controllability and robustness. By conducting a comprehensive modulational instability study with a mean-field model of the system, we explain the pattern formation in terms of its evolution from background noise, paving the way towards complete self-starting operation. Our theoretical and experimental study provides a clear pathway for repetition rate control of these waves over both fine (megahertz) and large (gigahertz) scales, featuring a fractional frequency non-uniformity better than 7.4×10^{-14} with a 100 ms time gate and without the need for active stabilisation.

3.1 Introduction

The formation of patterns in nonlinear dissipative systems is ubiquitous in nature [147]. The emergence of such self-organised periodic patterns on top of a homogeneous background, which was pioneered by Alan Turing, as been observed and investigated in many realms of science including chemistry, biology, and statistical mechanics [68, 147].

In particular, with regard to optics, patterns in nonlinear dissipative systems have been studied in both the spatial and temporal domains [73–75, 82, 90, 91, 160–166]. The temporal study of such patterns in bistable optical systems [74, 82, 90, 91, 165, 166] has received increasing attention in the last decade, in part due to the strong drive to develop optical frequency combs based on micro-cavities [57, 58, 105, 107, 120, 167–172], referred to as 'microcombs'. Typical implementations of such microcombs sources involve externally driving a nonlinear Kerr cavity with a continuous wave (CW) laser. This scheme has also emerged as an interesting scenario to study nonlinear systems far from equilibrium [76], where localised states such as cavity solitons, or the modulational instability (MI) of homogeneous states, can appear [168]. This configuration has been extensively studied theoretically and can be efficiently modelled with the Lugiato-Lefever equation [73, 112].

Bistable systems, in general, sustain different types of waveforms [147]. Of particular interest for microcombs are localised pulses, namely soliton, as well as periodic waveforms, usually referred to as patterns, Turing rolls, or cnoidal waves. Solitons are localised waves that can appear as either single or multiple pulses. Because these pulses are highly confined in time, solitons can achieve broad and smooth spectra and have, as such, been of significant interest to the microcomb community for applications in spectroscopy, optical ranging, and communications [102, 132–137, 139, 173, 174]. On the other hand, patterns are non-localised waves which, in contrast to solitons, are periodic within the cavity space and, in general, achieve fewer optical frequency modes. Nonetheless, the intrinsic nature of periodic waves leads to patterns that exhibit a more robust type of phase-locking and, for this reason, they are better suited to applications that require high-quality mode-locking of a high repetition rate source, such as pure micro-wave Terahertz generation or low-noise ultrafast telecommunications [83, 135, 175, 176].

Turing rolls can appear in Lugiato-Lefever systems that are pumped in either the normal or the anomalous dispersion regime [58, 73, 111, 147]. These different cases have an effect on the transition from Turing patterns to higher complex nonlinear regimes and/ or to spatio-temporal chaos. Anomalous dispersion configurations, for instance, are known for being prone to a limited regime of stability for Turing patterns. The transition to

spatio-temporal chaos has been recently studied in the monostable regime of the Lugiato-Lefever equation, highlighting the evolution of the states into a turbulent regime [177]. The transition to chaos, in general, is what limits the maximum conversion efficiency of the system. In the normal dispersion regime, local mode hybridisation has been implemented to enhance the pump conversion efficiency by increasing the region of existence of the Turing patterns, thus avoiding the emergence of sub-combs [175]. This technique has demonstrated combs with a fractional frequency non-uniformity measured at 7.3×10^{-14} with a 1 second time gate, and allows one to design a sample that produces an oscillator with a single, well defined repetition rate.

Looking more generally at alternative approaches for microcomb generation, we introduced a scheme based on nesting a high-Q, nonlinear micro-cavity into an amplifying fibre loop [127, 158, 178]. Such a scheme allows for coherent pulsed states [127, 158] and, as recently demonstrated, also sustains a class of temporal cavity-solitons, namely laser cavity-solitons [1]. Microcomb laser cavity-solitons are intrinsically background-free bright solitons, with a mode-efficiency exceeding 96 %, compared to the theoretical limit of 5 % for bright Lugiato-Lefever solitons. Remarkably, these solitons are reconfigurable in terms of repetition rate by simply acting on the cavity length of the fibre loop.

Here, we focus our attention on a different set of solutions of this laser: non-localised Turing pattern waves. Revisiting our original results for stable pulsed solutions [127] and implementing a comprehensive mean-field model, in conjunction with our new measurements, we explain the generation dynamics of these waves via a MI process. We examine the range of parameters for which it is possible to select the repetition rate, for some multiple of the micro-cavity FSR [156], and show that it can in fact be continuously tuned by up to 10 MHz. Finally, we demonstrate extremely robust and high-quality mode-locking, obtaining a repetition rate frequency variation well below the Hertz level, making such patterns particularly attractive for the generation of ultra-stable micro-wave sources. Our approach achieves a deviation in the repetition rate less than 7.4×10^{-14} for gate times of 100 ms, with the ability to tune the repetition rate by adjusting a simple parameter (or component i.e. a delay line). We verify experimentally continuous tuning of up to 10 MHz and Turing pattern generation with a repetition rate of approximately 100 GHz, 150 GHz and 200 GHz.

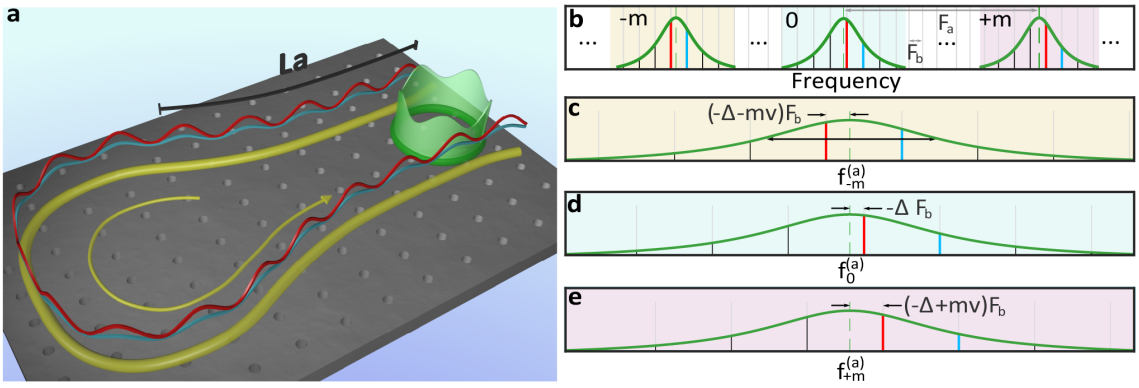

Figure 3.1: (a) Depiction of the laser operation. A Kerr microresonator (green ring) is nested into an amplifying fibre loop (yellow). A Turing pattern waveform (light-green) is excited in the micro-cavity and is sustained by leading order (red) and first-order (blue) 'super-mode' waveforms from the amplifying loop. These super-modes are periodical with the micro-cavity length, highlighted by a line segment L_a. (b) Spectral distribution of the modes in the cold-cavity condition. The micro-cavity resonances (green) have a free spectral range (FSR) denoted F_a while the FSR of the amplifying main-cavity modes (black) is denoted F_b. The leading order and first-order super-modes are plotted in red and blue, respectively. (c)-(e) Zoom of the m^{th}, central, and $-m^{th}$ resonances. Δ is the normalised frequency offset between the central frequency of the leading super-mode and the micro-cavity resonance. δ is the normalised FSR detuning, appearing when the two cavities are not commensurate.

3.2 Theoretical background

We begin by describing the two travelling-wave resonator system depicted in Fig.3.1, which features a Kerr cavity, such as a micro-ring (green ring), nested in a main amplifying cavity (e.g. a gain fibre loop (yellow loop)). Their round-trip time and length, expressed in standard units, are $T_{(a,b)}$ and $L_{(a,b)}$, with FSRs $F_{(a,b)} = T_{(a,b)}^{-1}$ respectively. We consider $T_b >> T_a$ and define an integer M such that

$$F_a = (M - \delta)F_b. \tag{3.1}$$

The relative cavity-period mismatch $|\delta| < 1/2$, that allows for modelling non-commensurate loops, is of particular importance. As we will see below, the FSR mismatch between the two cavities regulates the region of existence of solitons and patterns. In the latter case, we will show that δ has a fundamental role also in defining the properties of the MI of a constant stationary state, which defines the typical features of pattern formation and their FSR.

We define the spatial coordinates $X_{(a,b)}$ and assume that the optical fields in the two

cavities $A(T, X_a)$ and $B(T, X_b)$, in $[\sqrt{\mathrm{W}}]$, are slowly varying in time T, in seconds. It is important to derive an expression for the field in the main-cavity that permits an easy manipulation in terms of 'super-modes', also determining the existence and stability of several different stationary states in the system. A super-mode is a wave formed by a set of equally-spaced modes of the main-cavity, the relative spacing of which is given by the micro-cavity FSR F_a. This concept is depicted in Figs. 3.1(b - e). It is useful, then, to first expand the field $B(T, X_b)$ within the fibre cavity in the set of cavity modes $b_n(T)$,

$$B(T, X_b) = \sum_{n=-\infty}^{\infty} b_n(T) exp[2\pi i n \frac{X_b}{L_b}]. \tag{3.2}$$

The frequency of these modes, spaced by the main-cavity FSR F_b, is depicted by the grey lines in Fig. 3.1(b). We can now group together all the modes spaced by the micro-cavity FSR, which, as expressed by Eq. 3.1, is approximately M times larger than the main-cavity FSR. To this aim, we express the index n of the set b_n, as

$$n = mM + q, \tag{3.3}$$

where the integer m can take an arbitrary value while the integer q is given such that $|q| < M$ and defines the order of the super-mode. Figure 3.1(d) visually depicts those modes in red for the leading order mode with $q = 0$ and in blue for the first order mode $q = 1$. We can now focus our attention on the modes $b_n = b_{mM+q}$ featuring the same q. These modes are Fourier transformed in the space X_a of the micro-cavity,

$$B_q(T, X_a) = \sum_{n=-\infty}^{\infty} b_{mM+q}(T) exp[2\pi i m \frac{X_a}{L_a}]. \tag{3.4}$$

Here, the super-mode with $q = 0$ has the best spectral overlap with the micro-cavity resonance. The fields B_q in the direct space are summarised in Fig. 3.1(a), where the line segment L_a covers a length X_a equal to the micro-cavity round-trip.

As we have demonstrated in [1], the two-cavity system can be represented by a set of mean-field equations in terms of the field in the micro-cavity, A, and a total number of N super-mode fields, B_q, in the main-cavity (where $N << M$). As such, we consider the following parameter definitions: the waveguide first and second order dispersion $\beta_{(a,b)}^{(1,2)}$, in $[\mathrm{sm}^{-1}]$ and $[\mathrm{s}^2\mathrm{m}^{-1}]$ respectively; the amplifying gain within the main-cavity G, in $[\mathrm{m}^{-1}]$; the corresponding bandwidth ΔF_F, dictated by a band-pass filter, in Hertz; the Kerr waveguide coefficient γ, in $[\mathrm{W}^{-1}\mathrm{m}^{-1}]$ [110]; the $-3\,\mathrm{dB}$ linewidth of the micro-cavity

resonance ΔF_A, in Hertz, which is directly related to the coupling coefficient of the two cavities $\Theta = \pi\Delta F_A T_A$ [179]. Further, Δ is the cavity-frequency offset, normalised with F_b. The dimensionless system reads:

$$\partial_t a = \frac{i\zeta_a}{2}\partial_{xx}a + i|a|^2 a - \kappa a + \sqrt{\kappa}\sum_{q=-N}^{N} b_q, \tag{3.5}$$

$$\partial_t b_q = -\delta\partial_x b_q + (\frac{i\zeta_b}{2} + \sigma)\partial_{xx}b_q + 2\pi i(\Delta - q)b_q + g b_q - \sum_{p=-N}^{N} b_p + \sqrt{\kappa}a. \tag{3.6}$$

Here, the equations have been normalised as in [1]. Specifically, we make the normalisation of the propagating time against the main-cavity period in the moving pulses frame, $t = TT_b^{-1}$, while the fast cavity-time, defined as $x = X_a L_a^{-1} - TT_a^{-1}$, is normalised against the micro-cavity round-trip. Further normalisation of the system properties are for the micro-cavity field $a = A\sqrt{\gamma T_b L_a T_a^{-1}}$, the main-cavity field $b_q = B_q T_b T_a^{-1}\sqrt{\gamma L_a}$, and the filtered main-cavity bandwidth $\sigma = (2\pi\Delta F_F T_a)^{-2}$. The normalised coupling between the two cavities is defined such that $\kappa = \Theta T_b F_a = \pi\Delta F_A T_b$, which directly provides the number $\kappa\pi^{-1}$ of main-cavity modes per micro-ring resonance. Similar equations have also been studied for coupled waveguide laser configurations [128, 180, 181] and frequency selective feedback lasers [155].

It is important to stress that the system does not involve any form of fast gain saturation [90], which is not necessary for sustaining the types of waves studied here. We note, however, that slow saturation of the lasing material (in Ytterbium-Erbium doped fibre this value is of the order of 10 ms [182]) does play a role in setting the optical field energy within the system. The analysis reported here, then, is focused on explaining the nature of the stationary states and the ultrafast wave dynamics, such as MI, which are instrumental in defining the different types of stable states.

Since patterns may arise from the instability of a CW solution, it is useful to find the homogeneous solution, $a(t) = \sqrt{I}exp[-2\pi\phi t]$ and $b_q(t) = \bar{b}_q exp[-2\pi\phi t]$, where I is the constant intensity of the micro-cavity field, $\bar{b}_q$ is the constant field for the super-mode q, and ϕ is the normalised frequency of the stationary state. Among this class of solutions, the system also admits the trivial solutions $a(t) = 0$ and $b_q(t) = 0$.

For $N > 0$, we find $2N + 1$ states which are approximated by the formulas:

$$\phi_{\pm}^{(q)} = -(\Delta - q \pm (2\pi)^{-1}\sqrt{(1-g)g}), \tag{3.7}$$

$$I_{\pm}^{(q)} = (2\pi(\Delta - q)) \pm \frac{\sqrt{g}(1 - g + \kappa)}{\sqrt{1-g}}, \tag{3.8}$$

with q spanning from $-N$ to N and the field in the micro-resonator resulting in $a_{\pm}^{(q)}(t) = \sqrt{I_{\pm}^{(q)}} exp[-2\pi i \phi_{\pm}^{(q)} t]$ and $b_{p,\pm}^{(q)} \approx 0$ for $p \neq q$.

3.3 Modulational instability of the homogeneous, stationary states

Equations 3.5 and 3.6 define a homogeneous system which is solved by the trivial state solution $a = 0$ and $b_q = 0$. The MI of such a state provides important information on the region of existence of localised and non-localised solutions, as discussed in [1] for the formation of solitons. Here, we mostly focus our attention towards non-localised solutions, which can arise from the MI of the zero-energy background. The MI gain of the system is obtained by calculating the real part of the eigenvalues associated to the linear perturbation of the stationary state [147]. Such perturbation is a monochromatic wave with frequency f. We will refer to this frequency as the dynamical, or perturbation frequency.

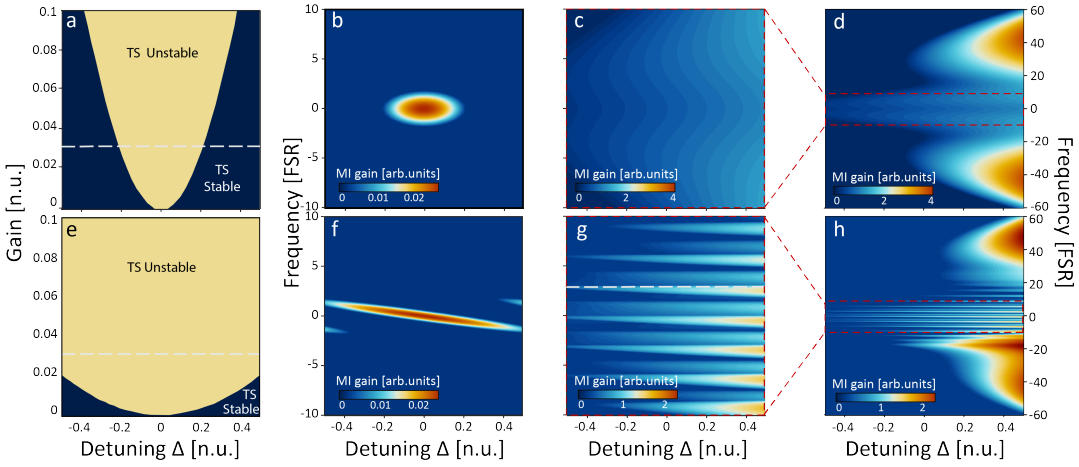

Figure 3.2: Modulation instability (MI) maps for the stationary states. For the calculations: $\zeta_a = 1.7 \times 10^{-4}, \zeta_b = 3.5 \times 10^{-4}, \sigma = 2.5 \times 10^{-4}, \sqrt{\kappa} = 2.5$, which are compatible with the experimental regime discussed in the sections below. Here we used $N = 7$, corresponding to a total of 15 super-modes.(a) MI map for the trivial solution (TS) showing the regions of instability as a function of the cavity gain g and detuning Δ, with $\delta = 0$. (b) MI gain of the zero solution with $g = 0.03$ (indicated by a white dashed line) and $\delta = 0$. (c) MI gain of the low energy CW state I_0^+. (d) Zoom out of (c). (e,f,g,h) same as (a,b,c,d) with $\delta = 1/3$.

Figure 3.2 summarises some significant results from the MI analysis as a function of the detuning parameter Δ. Since the system is periodic, with period 2π, we focus our attention on the base range $-\frac{1}{2} < \Delta < \frac{1}{2}$. Figures 3.2(a-d) and 3.2(e-h) show the results for the

matched cavities ($\delta = 0$) and for cavities with a period mismatch ($\delta = 1/3$), respectively. The maps in Figs. 3.2(a) and 3.2(e) generally summarise the stability regions for the trivial state as a function of the detuning Δ and cavity gain g. In the unstable regions (yellow shading) it is implied that the MI gain is positive for at least one perturbation frequency. Here, we notice that the zero-energy state is always unstable for perfectly matched cavities ($\Delta = 0$). Examining the MI gain over the range of perturbation frequencies (reported in Figs. 3.2(b) and 3.2(f)), at a specific value of the cavity gain: $g = 0.03$, we note that the maximum MI gain is observed for the perturbation frequency $f = 0$, resulting in a growth of a CW perturbation from the trivial state.

It is also important to properly evaluate the MI spectrum for homogeneous, non-trivial states. Within the set of parameters studied here, the MI analysis suggests that all CW states can be unstable within the base range. We focus our attention on the state $I_{+}^{(0)}$. As can be verified with Eq. 3.8, this state represents the lowest energy CW solution across the region $\Delta < 0$. A plot of the intensities of the CW states as a function of Δ is also reported in Fig. 3.3(c) for better visualisation. The MI for the matched cavities ($\delta = 0$) and for cavities with a period mismatch ($\delta = 1/3$), are reported in Figs. 3.2(c) and 3.2(g), which cover the lower dynamical frequency range of the complete MI spectrum presented in Figs. 3.2(d) and 3.2(h). The latter plots show that this MI gain is very wide for $\Delta > 0$ (red-detuned cavities) and extends towards very high frequencies. We recall that this is the region where solitons exist [1]. The MI gain for the range $\Delta < 0$ (blue-detuned cavities), conversely, can be more limited in bandwidth and hence it is easier to induce and control non-localised patterns.

In more detail, Figs. 3.2(g) and 3.2(h) show that the cavity-period mismatch δ can actually induce a set of new 'tongues' in the lower frequency spectrum of the MI gain. This can be understood considering that the presence of a filter within a laser cavity is known to allow the selection of pulsed states at multiples of the FSR associated with the filter cavity by means of the Vernier effect [156, 183]. In the formalism of this paper, when the mismatch δ is the inverse of some integer number K (i.e. $\delta = 1/K$), the frequency of the main-cavity mode can align to every K^{th} micro-ring resonance mode. This feature has also been shown, in some cases, to force the oscillation at every K^{th} FSR of the intracavity filter [156, 183] and in fact, stable oscillation has previously been obtained in configurations similar to that of our study, which a nonlinear micro-cavity was employed as a filter [156, 158].

Our analysis here allows us to clearly interpret the origin of the set of Turing pattern states in terms of a cascading MI. Indeed, the MI spectrum of the CW states can present

a sharp maximum around the dynamic frequency $f = K$. Figure 3.2(g) shows an example for the case $\delta = 1/3$, where the normalised frequency $f = 3$ is highlighted with a white dashed line. Figures 3.2(f) and 3.2(g), then, reveal the existence of a self-starting regime of the Turing pattern state defined for a set of values where $\Delta < 0$, an example of which is presented in Fig. 3.3. Here the MI gain of the trivial state initially seeds the growth of a CW state, which, once generated within the cavity, will have its dynamics regulated by the homogeneous states MI gain. In this case, the sharp peaks at $f = 3$ induce the formation of a stable Turing pattern at this frequency.

These considerations explain why this set of Turing patterns are very commonly observed [127, 156, 158, 178]. They are a set of intrinsically self-starting solutions that can be readily reformed if the energy in the cavity is lost through some perturbation. The presence of sharply localised tongues in the MI spectrum allows for a very clean selection of the dynamic frequency f, which is controlled directly by the cavity mismatch δ. We will discuss this, along with the effect of small changes of the cavity mismatch, δ, along with our experiments, in section 3.4.

Finally, the strong skew in the MI spectrum induced by the period mismatch δ (as shown in Figs. 3.2(e-h)), shifting the higher frequencies towards the border of the base range of the detuning Δ, may be indicative that the system can support Faraday instabilities, which have been recently studied in resonators with regions of differing group velocity dispersion [184, 185].

3.4 Experimental implementation

A schematic of our experimental setup is shown in Fig. 3.4(a). It is composed of a high-Q ($>10^6$) integrated Hydex microresonator [45], an Erbium-Ytterbium doped fibre amplifier (EYDFA), a free space delay line, a tunable passband filter, and an optical isolator. The micro-resonator FSR is ∼49 GHz with a linewidth of ∼100 MHz. The EYDFA provides a relatively large gain over a short fibre length (<1.5 m), the gain profile being shaped by the tunable passband filter (6 nm, 3 dB bandwidth) centered at ∼1550 nm. The free space delay line is used for controlling the phase of the main-cavity modes with respect to the micro-cavity modes. The total main-cavity length is ∼3.5 m, resulting in a mode spacing of ∼55 MHz. The use of fully polarisation maintaining fibre components prevents any nonlinear polarisation rotation effects [168].

Laser scanning spectroscopy [1, 157, 158] is performed in order to extract the exact positions of the oscillating microcomb lines in the hot resonator (i.e. during operation). A

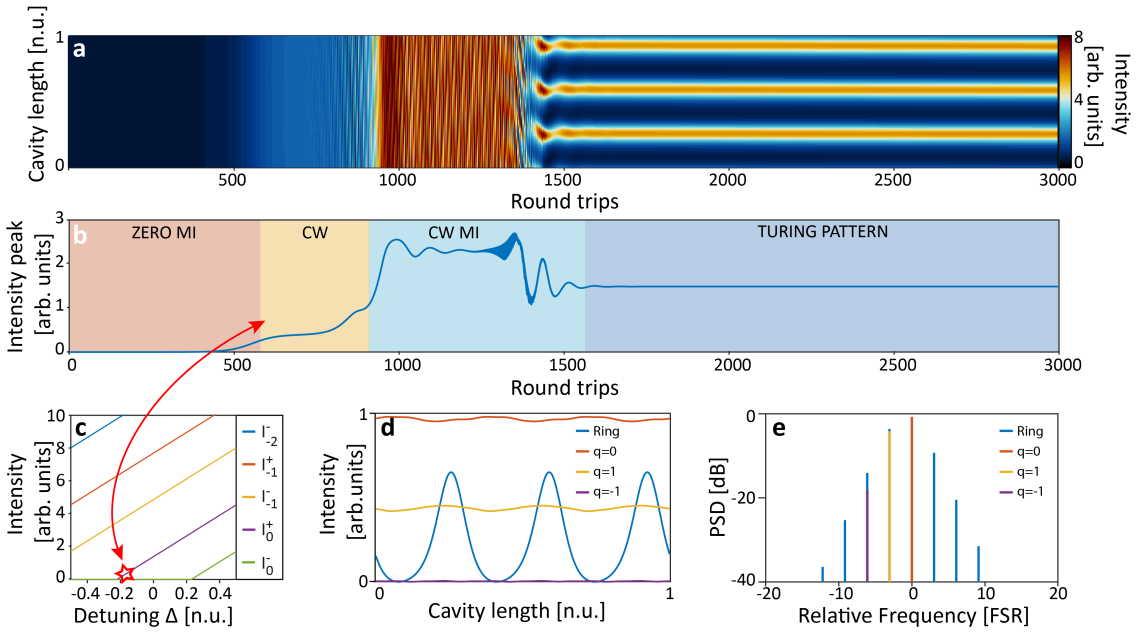

Figure 3.3: Self-starting Turing pattern states. The zero solution evolves into the state $I_{+}^{(0)}$, which is also unstable and gives rise to a Turing pattern. The simulation parameters are: $\zeta_a = 1.7 \times 10^{-4}, \zeta_b = 3.5 \times 10^{-4}, \sigma = 2.5 \times 10^{-4}, \Delta = -0.17, \sqrt{\kappa} = 2.5, g = 0.0365, \delta = -0.3342$ and $N = 7$. (a) Evolution of the temporal profile of the field in the micro-cavity with the y-axis normalised to the micro-cavity length. (b) Maximum intensity of the evolution in the micro-cavity. (c) Low energy stationary states. (d) Output time profile of the fields in the micro- and main-cavities. (e) Output spectral profiles of the fields within the micro- and main-cavities, with power spectral density (PSD) as a function of the normalised relative frequency.

scanning CW laser probes the resonance profiles and oscillating micro-comb lines while a reference frequency comb (Menlo Systems) and a Mach-Zehnder interferometer (MZI) are used to perform highly accurate frequency calibrations, as illustrated in Fig. 3.4(b).

A frequency uniformity measurement setup [99, 175, 186] is used to extract the microcomb repetition rate deviation. Here, three adjacent microcomb lines are selected and beat with three adjacent lines of a reference frequency comb. The three beat notes, B1, B2, and B3 are combined (B1-B2 and B2-B3) through two frequency mixers. We retained only the repetition rate frequency signal which was detected by a high-resolution frequency counter in the ratio counting mode (10 mHz frequency error at 1 s).

The optical spectrum and autocorrelation from the system are monitored with the intracavity optical coupler at the microresonator drop port. In particular, the laser scanning spectroscopy measurements utilise the small back-reflected signal from the input port, while the frequency non-uniformity measurement uses the microresonator through port signal.

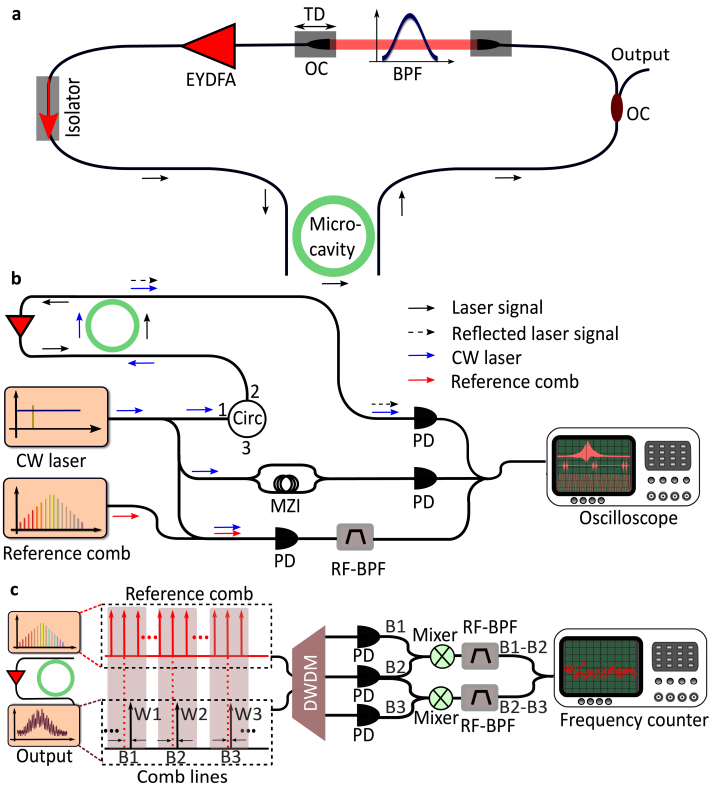

Figure 3.4: (a) Experimental setup of the micro-resonator filtered fibre laser. EYDFA, Erbium-Ytterbium doped fibre amplifier; TD, translation delay-stage; BPF, bandpass filter; OC, output coupler. (b) Diagnostic setup for the laser scanning spectroscopy. PD, photodiode; MZI, Mach-Zehnder interferometer; RF-BPF, radio-frequency bandpass filter. (c) Diagnostic setup for the frequency non-uniformity measurement. The beat notes B1, B2, and B3 between the three desired comb lines W1, W2, and W3 and their adjacent reference frequency comb lines are selected using a dense wavelength division multiplexer (DWDM). They are then mixed and counted by a high-resolution frequency counter.

3.5 Turing pattern selection via the Vernier effect

We first verified the properties of the Turing pattern states controlled by the Vernier effect, that is, the periodical spectral alignment of transmission resonances that occurs in systems where there are two or more coupled cavities – in our case, the micro-cavity and the amplifying fibre cavity. As discussed in Fig. 3.3, the cavity detuning and mismatch parameters, respectively Δ and δ, need to be carefully adjusted in order to access this regime. Experimentally, this control is obtained by acting on the delay line in the fibre cavity. The position of the oscillation microcomb lines can be verified by means of the intra-cavity laser scanning spectroscopy setup. The experimental results shown in Fig. 3.5 display a range of cases, with comb teeth spaced by 2, 3, and 4 FSRs. A numerical fitting is performed on these measurements using Eqs. 3.5 and 3.6, with simulation parameters:

$\zeta_a = 1.7 \times 10^{-4}, \zeta_b = 3.5 \times 10^{-4}, \sigma = 2.5 \times 10^{-4}, \sqrt{\kappa} = 2.5, N = 7$, and values $|\beta^{(2)}_{(a)}| = 20\,\mathrm{ps}^2/\mathrm{km}$ and $|\beta^{(2)}_{(b)}| = 60\,\mathrm{ps}^2/\mathrm{km}$ (within our experimental constraints).

Figures 3.5(a), 3.5(d), and 3.5(g) show the experimental optical spectra, as well as autocorrelation traces and the position of the central oscillating comb line (i.e. the mode with the highest PSD). The corresponding simulated spectral traces are presented in Figs. 3.5(b), 3.5(e), and 3.5(h) for a set of Turing patterns with frequency spacing at 2, 3, and 4 FSRs. The high contrast autocorrelation traces are indicative of the coherence of the waveform. The intra-cavity spectrum shows an oscillation line within the micro-cavity resonance blue-detuned by 13.9 MHz, 12.4 MHz and 22.1 MHz. For the numerical fitting in Figs. 3.5(b), 3.5(e), and 3.5(h), settings of $\Delta = -0.36, \Delta = -0.17, and \Delta = -0.54$ were used, along with mismatch parameters $\delta = 1/2, \delta = 1/3$, and $\delta = 1/4$. The analysis around Fig. 3.2 has indicated that, for these parameters, the MI of the trivial solution leads to the emergence of a homogeneous state. Figures 3.5(c), 3.5(f), and 3.5(i) depict the MI gain spectrum of such a state, given each set of parameters. The related gain spectrum shows a clear maximum around the perturbation frequency at approximately 2, 3, and 4 FSRs, which is consistent with the experimentally observed comb line spacings.

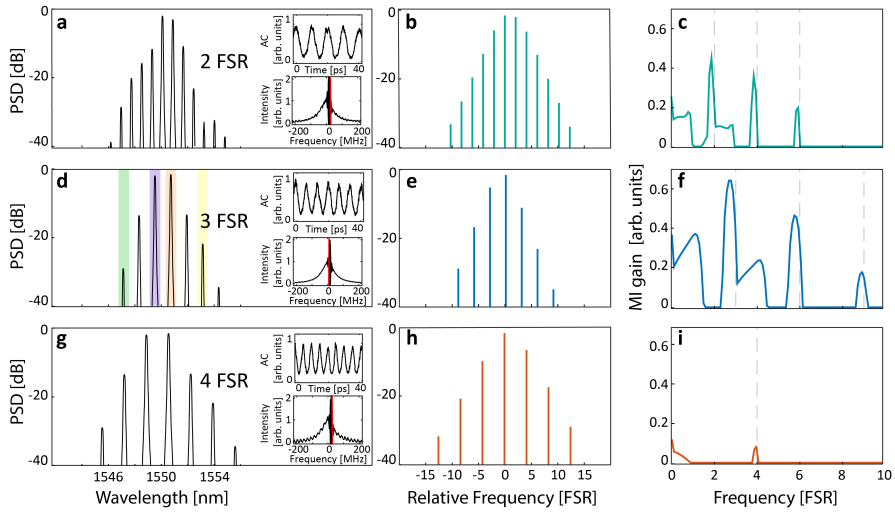

Figure 3.5: (a,d,g) Experimental optical power spectral density (PSD) for the micro-comb modes. The inserts depict the autocorrelation and the intra-cavity spectrum of the oscillating spectral mode with the highest power. The red line here shows the position of detuning Δ used in the respective simulations. The colour shadings in (d) are in reference to the resonance profiles presented in Fig. 3.6. (b,e,h) Simulated optical spectra calculated a $\delta = 1/2, 1/3$, and $1/4$ respectively, with corresponding gain settings and cavity detunings of (b) $g = 0.0400, \Delta = -0.36$, (e) $g = 0.0320, \Delta = -0.17$, and (h) $g = 0.0501, \Delta = -0.54$. (c,f,i) MI gain spectrum of the CW states. In the calculations: $\zeta_a = 1.7 \times 10^{-4}, \zeta_b = 3.5 \times 10^{-4}, \sigma = 2.5 \times 10^{-4}, \sqrt{\kappa} = 2.5$, and $N = 7$.

3.6 Fine tuning and phase locking of the Turing patterns

Experimentally, the fine tunability of the repetition rate can be obtained by slight modification of the main-cavity length via a tunable delay line. Stable laser oscillation is observed throughout the whole tuning process, highlighting the capability of the system to maintain this state. We present an example of this tunability, with intra-cavity spectroscopy measurements of a Turing pattern with a period equal to 3 times the FSR of the nested micro-resonator. Similar tunability has been verified on all the cases presented above. We use five different fibre cavity lengths covering a range of 400 μm. The intra-cavity spectroscopy measurements allow us to visualise the shift of the resonating lines within the micro-cavity resonances and is summarised in Fig. 3.6. Note that in all these cases we observe that the line with the highest PSD (highlighted with orange shading) remains in almost the same position with respect to the central resonance (the variations are within a few megahertz), while side-band modes experience much larger shifts which are indicative of a change in the repetition rate. From these lines, we extract a normalised detuning parameter $\Delta = -0.35$ for all the cases, while the mismatch parameter δ, varies by 0.044, 0.064, 0.076, 0.092 and 0.106 around the value of $\delta = 1/3$, for respective main-cavity lengths.

Figure 3.7 shows further simulations that agree well with the experimental observations on the tunability of the repetition rate. The numerical parameters are the same as in previous simulations shown in Fig. 3.3, where the mismatch δ was changed from -0.33 to -0.39: corresponding to an experimental change in cavity length of 400 µm. The stability that is maintained over this range in our simulations emphasises the strong agreement between our theoretical model and experiments. The change in group velocity of the pattern obtained in Fig. 3.7, compared to Fig. 3.3, indicated the fine tuning of the repetition rate. This is visible from the clear inclination of the patterns in Fig. 3.7(a), which is better shown in the inset of the figure. These simulations also confirm the strong phase locking of the Turing pattern states, as already discussed within the context of the Lugiato-Lefever combs [83]. To highlight this, the differential phase evolution of the absolute phase for three of the modes is presented in Fig. 3.7(d), demonstrating the strong phase-locking of the repetition rate. For a more accurate measurement of the repetition rate detuning and stability we employ a frequency non-uniformity measurement technique, as illustrated in Fig. 3.4(c) [99, 175, 186], in order to probe the equidistance of the comb lines. The recorded mixed frequencies for the experiment in Fig. 3.6 are shown in Fig. 3.8(a) for cases where the differential length of the delay line varies from 0 µm to -400 µm. The resulting

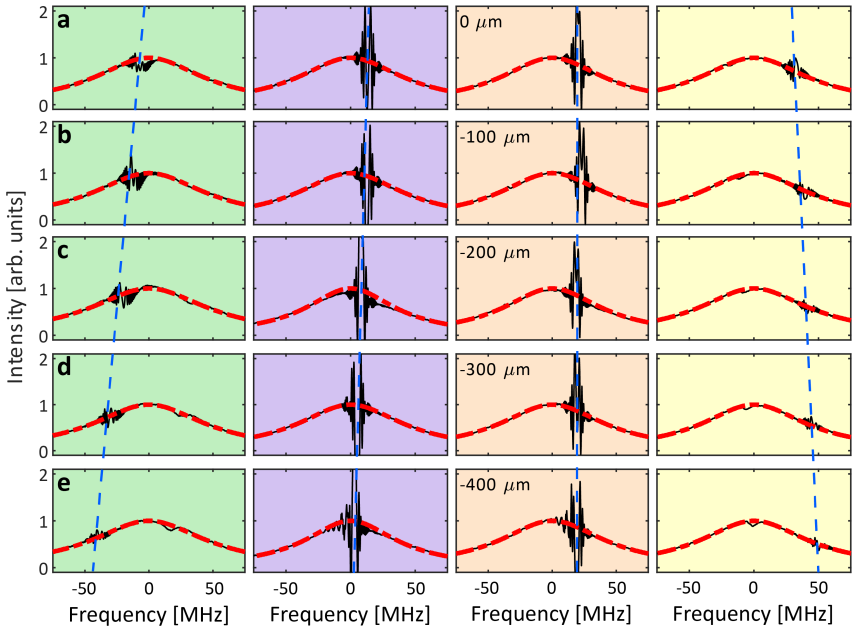

Figure 3.6: Experimental resonance profiles and beat note signals obtained with the probe laser scanning oscillating comb lines. (a-e) Descending rows correspond to a relative change in the main-cavity length of 0 µm, −100 µm, −200 µm, −300 µm and −400 µm. The four sequential colour-shaded plots correspond to different comb line wavelengths: 1547.13 nm, 1549.47 nm, 1550.64 nm and 1553.01 nm from the left to the right panels, as indicated by the colour shadings in Fig. 3.5(d). The dashed red line is a Lorentzian fit to the profile of the hot resonance while the vertical dashed-blue lines indicate the relative shift of the oscillating comb lines within their respective resonances.

average change in repetition rate is plotted for the various cavity delay lengths, with the raw frequency data displayed in blue. The linear increase in the repetition rate by up to 10 MHz as the fibre cavity is clearly visible as the length is decreased. The quality of the phase-locking for these Turing pattern states can then be evaluated. A typical distribution of the frequency deviation stemming from an equidistant mode spacing, for a gate time of 100 ms, is shown in Fig. 3.8(b). This measurement was obtained by setting the reference comb repetition rate as a non-integer sub-multiple of the microcomb repetition rate. As such, the beating signals (indicated as 'B1-B2' and 'B2-B3' in Fig. 3.4(c)) were centred around a frequency of 18 MHz, which was passband filtered. We collected the ratio between the two signals in order to extract the stability of the repetition rate. Since our measurement system was not further phase-locked, we observed slips of the measurement towards other beat notes, which have been removed from the dataset by setting a threshold at ±5 Hz. The mean and standard deviation of the frequency distributions in Fig. 3.8 are presented in Table 3.1.

Our mean values are consistently in the same order of magnitude as the standard error,

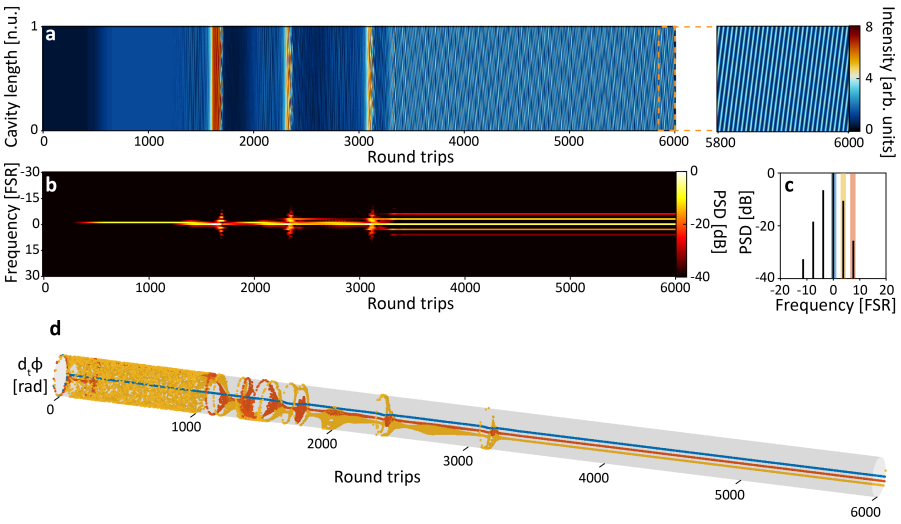

Figure 3.7: (a,b) Numerical results showing the evolution of the temporal (a) and the spectral (b) profile of the field. The temporal evolution has a corresponding zoom of the stable operation to illustrate more clearly the pattern. For the simulations: $\zeta_a = 1.7 \times 10^{-4}, \zeta_b = 3.5 \times 10^{-4}, \sigma = 2.5 \times 10^{-4}, \Delta = -0.17, \sqrt{\kappa} = 2.5, g = 0.0365, \delta = -0.3942$, and $N = 7$. (c) Optical spectrum of the stable pattern state. (d) Differential phase evolution of three comb modes, indicated by the coloured shading in (c). The differential phase is calculated as the derivative of the absolute phase ψ_n over the temporal evolution and it is indicative of the stability intrinsic to the repetition rate of the comb.

which are all in the range of 10 mHz, indicating that even with short time gates of 100 ms we can claim a stability better than 7×10^{-14} for the 150 GHz state. Our electronics unlocked several times during the measurement of the case at -200 µm, which has a low number of counts and, for this reason, the highest standard error.

Typical values for the stability of the repetition rate associated with free-running micro-comb sources range from 10^{-9} to 10^{-12} for solitons states measured with these level of time gates [187, 188]. Free-running Turing pattern-based sources, which are known for having a stronger phase-lock, have been demonstrated in the same order of magnitude

Table 3.1: Results of the frequency non-uniformity measurements of the data in Fig. 3.6 and Fig. 3.8 for a time gate of 100 ms

Relative delay (µm)	Mean (MHz)	Standard deviation (mHz)	Approved counts (-)	Relative deviation (-)
−400	-5.5 ± 8.3	213	655	5.5×10^{-14}
−300	-10.0 ± 11.0	219	432	6.7×10^{-14}
−200	-12.0 ± 20.0	172	74	1.3×10^{-14}
−100	-3.5 ± 9.5	228	580	6.3×10^{-14}
0	-8.1 ± 9.7	235	588	6.4×10^{-14}

(7×10^{-14}) as our measurement, but were obtained with time gates of one second [175]. This shows the remarkable performances of our system, which can achieve the same level of stability averaging on gate times shorter by one order of magnitude. We believe that this enhanced stability is due to the intrinsic feedback of our nested cavity design. In addition, we maintain this excellent stability continuously over a tuning range of 10 MHz, while designs such as that proposed in [175] requires fixing the repetition rate to a specific value. Our tuning capabilities are in good agreement with the theoretical calculation in Fig. 3.7(d), which shows the strong locking of the Turing pattern state also when the group velocity is detuned.

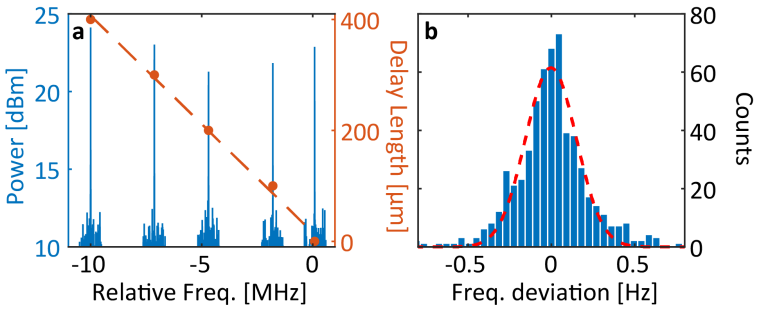

Figure 3.8: (a) The average beat note frequencies between two selected microcomb lines and their adjacent reference frequency comb teeth (recorded by an oscilloscope) as a function of the decreasing main-cavity length. The raw frequency measurement (in megahertz), relative to the frequency for 0 µm delay, is shown in blue. (b) Distribution of the microcomb output spectrum stemming from an equidistant mode spacing, including a Gaussian fit (dashed red line). Here, we consider the −300 µm delay case, with a frequency counter gate time of 100 ms.

3.7 Conclusion

In conclusion, we study the formation of non-localised Turing patterns in a system where a nonlinear high-Q micro-resonator is nested into an active fibre loop. By using a comprehensive mean-field model, we develop a MI analysis which explains the nature of these waves, revealing the dynamics of their formation from noise and explaining the ease with which they are observed. We demonstrate that these waves possess strong phase locking, with frequency deviations of the repetition rate frequency below the 1 Hz level. Further, we show that the repetition rate can in fact be controlled by simply acting on the main-cavity length: affecting the MI spectrum while maintaining the pulse quality. In this regard, the experimental results demonstrate that the repetition rate of these waves can be controlled over both fine (megahertz) and large (gigahertz) scales, with a continuous tuning of up to

10 MHz verified experimentally. This work has practical implications, offering a simple yet powerful method to control the repetition rate. From a theoretical point of view, it will help to increase our understanding of nonlinear processes in nested micro cavity systems. Our results provide a pathway for designing practical microcomb devices that can be easily initiated and tuned by the end-user: a fundamental requirement for the widespread use of these devices outside of the laboratory environment.

Chapter 4

Thermo-optical pulsing in a microresonator-filtered fiber laser: a route towards all-optical control and synchronisation

We report on 'slow' pulsing dynamics in a silica resonator-based laser system: by nesting a high-Q rod-resonator inside an amplifying fibre cavity, we demonstrate that trains of microsecond pulses can be generated with repetition rates in the hundreds of kilohertz. We show that such pulses are produced with a period equivalent to several hundreds of laser cavity round-trips via the interaction between the gain dynamics in the fibre cavity and the thermo-optical effects in the high-Q resonator. Experiments reveal that the pulsing properties can be controlled by adjusting the amplifying fibre cavity parameters. Our results, confirmed by numerical simulations, provide useful insights on the dynamical onset of complex self-organisation phenomena in resonator-based laser systems where thermo-optical effects play an active role. In addition, we show how the thermal state of the resonator can be probed and even modified by an external, counter-propagating optical field, thus hinting towards novel approaches for all-optical control and sensing applications.

4.1 Introduction

Within the field of nonlinear optics, the long cavity lifetime and reduced mode-area provided by high-Q whispering gallery mode (WGM) resonators have been demonstrated as an efficient way to achieve important Kerr nonlinearity enhancement, and thus unlock numerous functionalities, at reasonable power levels compatible with continuous-wave (CW) operation [57]. Besides the rather conventional excitation of microresonators using an external optical field [62, 63, 189], there have been significant efforts over the last few years to utilise microcavities for the development of novel laser configurations [58], especially with the prospect of system miniaturisation. Applications of these embedded resonator systems include compact frequency comb generation [81, 91, 99, 102, 127, 190], including self-injection locking schemes [107, 108, 191, 192], passively mode-locked nanosecond pulsing [193], microdisk lasers development [125, 126], or even the generation of quantum frequency combs [141].

Such applications are possible due to strong and desirable nonlinear effects in these devices (e.g. Kerr nonlinearity), which can be effectively paired with more complex dynamics. Indeed, in these resonant structures, the strong field enhancement is usually associated with additional intensity-dependent effects which can be considered detrimental: free carrier absorption in silicon [44], Raman and Brillouin scattering [194], as well as thermo-optical [113] and opto-mechanical [195] effects can play a disruptive role in numerous dynamical processes.

Of particular interest here is the temperature-dependent modification of the optical refractive index and/ or mode volume, ubiquitous in all WGM resonators. Understanding and controlling this thermally-induced frequency drift has been key in the generation of cavity solitons by externally seeding WGM cavities with a CW field [81]. Indeed, such a scheme typically requires a form of active monitoring and feedback control to ensure stable operation. There are however examples of the beneficial use of these adverse nonlinear effects, notably for the demonstration of opto-mechanical chaos transfer [196], the generation of giant pulses [197], thermal sensing [198], regenerative pulsation [199] and self-sustained pulsation [200–202], also controlled by parametric nonlinearity [203].

Interestingly, using an external amplifying cavity structure to passively stabilise slow temperature drifts and circumvent thermo-optical effects was already proposed and demonstrated in microresonators [127]. Yet, to date, the dynamical interactions between these two non-instantaneous physical processes still remain widely unexplored beyond their stabilisation capabilities.

Here we report on a thermo-optically driven pulsing mechanism demonstrated in a laser system consisting of a fused-silica WGM resonator [55] directly nested in an external fibre amplifying loop. In our system, the complex dynamical interaction between the thermo-optical effect in the resonator and the slow response of the gain medium leads to a sustained self-pulsing. Such dynamical behaviour, typically encountered in nonlinear optical cavities exhibiting a nonlinear relaxation time significantly longer than the cavity round trip time [204], is here observed experimentally. We reveal that the observed pulse train characteristics can be directly controlled by adjusting the laser cavity parameters. Additionally, we show a thermo-optically mediated transfer of the dynamics of this lasing mode to an externally coupled probe field in the microresonator. The experimental results, exhibiting a variety of self-organisation effects and multistable dynamics, are supported by numerical simulations exhibiting good qualitative agreement. Our results pave the way towards non-instantaneous all-optical control of the resonator dynamics along with potentially wavelength- and/ or spatial-mode-independent signal processing and synchronisation features.

4.2 Experimental setup

Our experimental setup is shown in Fig. 4.1(a): we nest a high-Q ($>10^6$) fused-silica rod resonator coupled via tapered fibres (see inset) inside an Erbium-doped fibre amplifier (EDFA) loop cavity. The EDFA is a fibre optical amplifier which provides amplification to light in the Telecom band via stimulated emission. EDFA technology has been selected as it is a standardised optical component and underpins the optics of the Telecom industry and can provide high output powers, which are sufficient to induce strong thermo-optical effects in WGM resonators. An isolator is incorporated within the fibre cavity to ensure unidirectional operation (see blue arrows). The overall intra-cavity power can be adjusted by the EDFA pump current, as well as additional losses induced by a variable optical attenuator (VOA). The 4-port resonator transmission properties can additionally be probed via a continuous wave laser with tunable wavelength (Tunics-plus), counter-propagating within the resonator. Both the intra-cavity field (blue) and optional counter-propagating CW probe properties can be measured temporally using a fast oscilloscope and photodiodes (200 MHz oscilloscope bandwidth) and spectrally using and optical spectrum analyser (Anritsu MS9740A with 70 pm resolution). The intra-cavity field is probed using a 10 % output fibre coupler (90:10) and eventual back-reflections between the frequency-detuned counter-propagating fields are avoided by the presence of isolators and a wavelength divi-

sion multiplexer.

The broadband EDFA spectrum transmitted by the resonator is shown in Fig. 4.1(b), and further filtered by a bandpass filter, consisting of a fibre Bragg grating and a circulator. The bandpass filter is centered at 1545.064 nm and exhibits a 33.7 GHz bandwidth (see blue shading in Fig. 4.1(b)). As illustrated in Fig. 4.1(c), this bandwidth is slightly larger than the resonator free spectral range (FSR) of 24.1 GHz. The fine transmission spectrum reveals a structure featured with multiple spatial modes. However, as seen in Figs. 4.1(d) and 4.1(e), a careful selection of the resonator input polarisation allows for the selection of only one (or few) predominant resonances to oscillate in the cavity within the bandpass filter bandwidth, and thus minimises mode competition (see Fig. 4.1(f)). In the main cavity, all components are polarisation-maintaining (PM) besides two fibre polarisation controllers before and after the tapers coupled to the resonator, to respectively select the main coupled resonance and minimise the losses between the resonator and PM cavity components. Figure 4.1(g) shows the selected TM resonance (purple) and the Lorentzian fit (dashed black) obtained by accounting for the 400 kHz linewidth of our CW sweeping laser. We found a coupled full with half maximum (FWHM) linewidth of 27.2 MHz thus yielding a 7.1 million loaded Q-factor at 1545 nm (the intrinsic Q-factor is around 10^8) and encompassing a single mode of the 6.7 m main amplifying fibre cavity (i.e. 30.9 MHz FSR).

4.3 Results and discussion

When the system operation is suitably adjusted, stable and sustained self-pulsing is observed, as illustrated in Fig. 4.2(a). In this lasing regime, the average pulsing period is typically 15 µs with a pulse duration on the order of a microsecond (see below for details). Here, the pulsing operation is rather stable with a peak intensity relative noise below 5 % RMS deviation. Figure 4.2(b) shows a slight pulse asymmetry, where an elongation is observed in the trailing edge, a feature typical of dynamics associated with long timescales relative to the cavity lifetime. The corresponding spectrum, shown in Fig. 4.2(c), features a single spectral line with a linewidth in agreement with a single mode resonance oscillation (when considering the limited OSA spectral resolution) while the phase space portrait, represented in Fig. 4.2(d), illustrated the presence of an attractor associated with the self-pulsing behaviour observed in this system.

In fact, such self-pulsing dynamics are notorious in many complex and nonlinear systems, and are typically encountered in optical lasing architectures exhibiting bistability, where

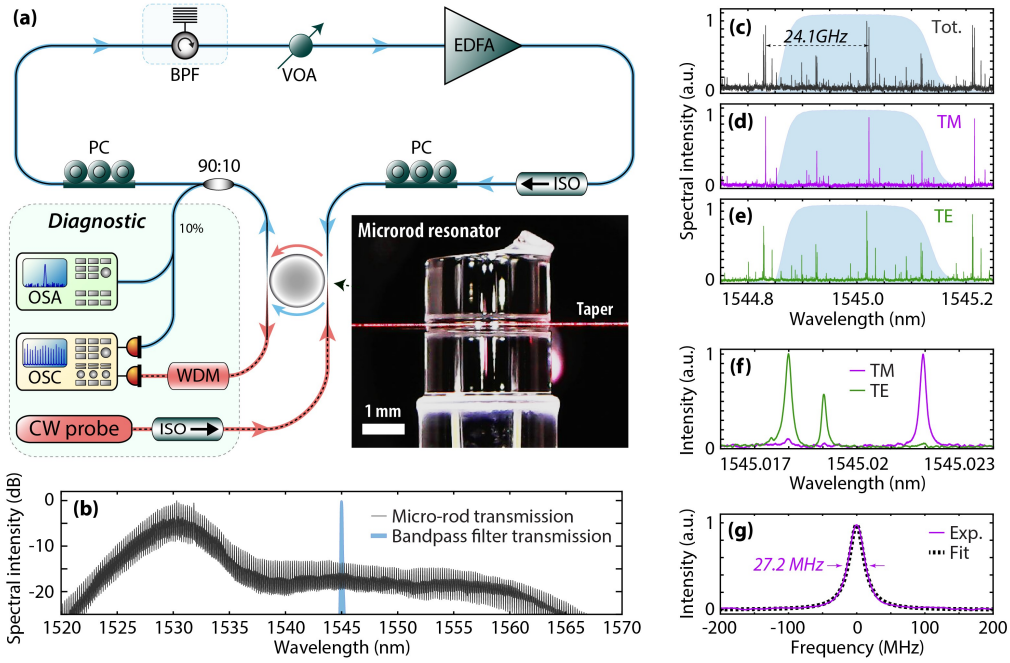

Figure 4.1: (a) Schematic of the experimental setup. PC, fibre polarisation controller; VOA, variable optical attenuator; BPF; bandpass filter; EDFA, Erbium-doped fibre amplifier; OSC, oscilloscope; OSA, optical spectrum analyser. Inset: Side view of the silica rod resonator and coupled fibre used for optical injection. (b) OSA transmission spectra of the resonator (grey) and BPF (blue shading) when seeded by the EDFA. (c-e) High-resolution transmission spectra obtained by CW wavelength sweep using either unpolarised (c) or polarised transverse magnetic (TM) (d) and transverse electric (TE) (e) light. (f) Zoom on the predominant spatial modes oscillating for each polarisation. (g) Spectrum of the selected TM main resonance and Lorentzian fit (dashed black line) used experimentally.

the relaxation time of the nonlinear effect is significantly longer than the cavity round-trip time [201, 202, 204]. In our case, the pulse train period (15 µs) corresponds to over 450 cavity roundtrips but is, conversely, in the order of magnitude of the dynamical timescales at play within our system, namely primarily the thermo-optical effects in the resonator but also the slower gain recovery in the main fibre cavity. In order to obtain insight into the dynamics observed experimentally, we employ a numerical model based on coupled-mode theory [205], using standard approaches outlined in [1, 58, 111, 205–208]. In particular, we follow the field evolution in both the resonator and fibre cavities, assuming a single scalar longitudinal mode seeding an intensity-dependent frequency shift induced thermally in the resonator. This themo-optical behaviour is schematically illustrated in Fig. 4.3(a)

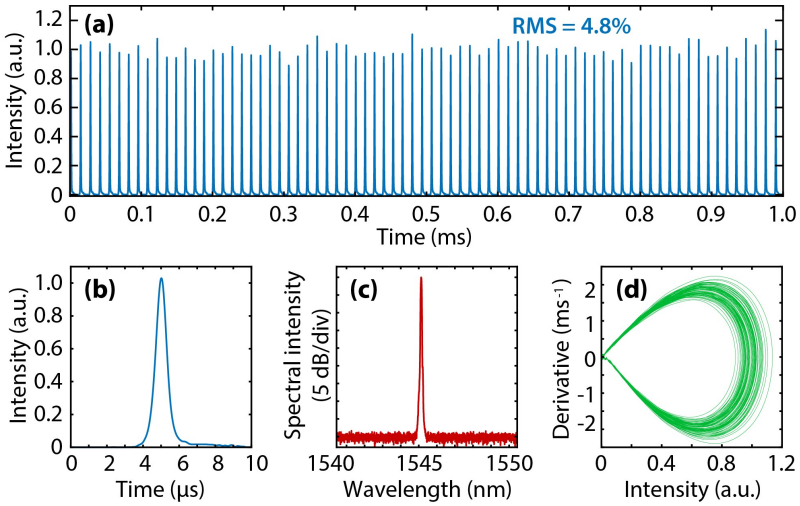

Figure 4.2: (a) Typical pulse trace measured experimentally using the setup shown in Fig. 4.1 in TM polarisation. (b) Zoom on a single pulse period. (c) Corresponding OSA spectrum. (d) Phase space portrait depicting the intensity versus the derivative of the intensity of the pulse train in panel (a).

and the overall evolution of the system is expressed as:

$$\partial_t a = -\pi \Delta F_A a + i|a|^2 a + i\Delta\omega_T a + \sqrt{\theta}\frac{b}{\sqrt{T_A T_B}} \tag{4.1}$$

$$\partial_t b = -i\Delta\omega b + (g - \alpha - \frac{1}{T_B})b + \sqrt{\theta}\frac{a}{\sqrt{T_A T_B}} \tag{4.2}$$

$$\partial_t g = \frac{(g_0 - g)}{T_g} - R_g|b|^2 g \tag{4.3}$$

$$\partial_t \Delta\omega_T = -\frac{1}{T_T}(\Delta\omega_T - R_T|a|^2) \tag{4.4}$$

Here, a and b are the normalised mode amplitudes in the resonator and the main cavity, respectively [1, 58, 206]. We model the EDFA in terms of a standard first order equation in the gain g of the main cavity, derived from a set of Maxwell-Bloch (MB) equations for a two-level system by adiabatical elimination of the polarisation field [206, 208]. Here, the estimated population relaxation time is $T_g = 900\,\mu s$ [209]. The thermo-optical frequency shift of the resonator $\Delta\omega_T = 2\pi\Delta\nu$ is intensity-dependent with an estimated relaxation time constant $T_T = 3\,\mu s$ [113]. The resonator and main cavity round-trip times used in our simulations correspond to the experimental values and respectively $T_A = 1/F_A = 41.5\,ps$ and $T_B = 1/F_B = 29.8\,ns$. Similarly, we assume a resonator with a FWHM linewidth of $\Delta F_A = 27.2\,MHz$, which is strongly dominated by the coupling to the two tapered fibres, so that the coupling constant between the main cavity and the resonator can be estimated as $\theta = \pi\Delta F_A T_A$. It is worth mentioning that, in our equations, the mode amplitudes are normalised with respect to the Kerr nonlinear mode coefficient $\Gamma_K = 4.82 \times 10^{15}\,J^{-1}s^{-1}$

estimated in the resonator. Specifically, the normalised amplitude in the resonator a can be derived from the dimensional mode energy A [in Joules] so that $|a|^2 = \Gamma_K A$. The main cavity mode follows the same normalisation where $|b|^2 = \Gamma_k B$ and the strength of the intensity-dependent thermal nonlinearity Γ_T is estimated to be approximately two orders of magnitude larger than the instantaneous Kerr effect in the resonator, thus yielding $R_T = \Gamma_T/\Gamma_K = 100$ [210]. The gain-main cavity field coupling constant, corresponding to the inverse of the saturation power, is given as $R_g = \eta_g/\Gamma_K = 69.6$ where we estimated a gain coefficient $\eta_g = 3.35 \times 10^{17}\,\mathrm{J^{-1}s^{-1}}$ assuming a fast decay time of 400 fs for the EDFA doping concentration used in our experiment [206]. In our simulations, we can observe a wide variety of dynamics depending on the static cavity parameters, namely the main cavity losses α and the initial gain g_0 as well as the cold-cavity angular frequency mismatch $\Delta\omega$ between the central resonance and the main-cavity mode, which, in single mode operation, is assumed to be within the resonance FWHM and thus bounded as $|\Delta\omega| < \Delta F_A/2$. For selected parameters, numerical simulations of the system display sustained self-pulsing in good agreement with the dynamical behaviour observed in our experiments. In particular, we selected $\Delta\omega = -\Delta F/5$ to best match the self-pulsing dynamics observed experimentally.

The numerical results are illustrated in Fig 4.3(b), where the formation of pulses (solid blue line) is associated with a rapid frequency shift $\Delta\nu$ of the seeded resonance (dashed purple line), followed by a slower recovery of the initial (blue-detuned) resonance frequency during the absence of pulse emission. Physically, the dynamical mechanisms responsible for such operation are qualitatively described in Fig. 4.3(a): the length of the main cavity, combined with the band-pass filter (see Fig. 4.1(b)), ensures that only one predominant cavity mode lies within the resonator linewidth ΔF_A. The oscillation of such a mode induces a thermo-optical refractive index variation in the resonator, associated with a varying detuning of the main cavity mode within the shifting resonance. This, in turn, gives rise to a thermo-optically modulated loss mechanism, with a characteristic timescale much longer than the round-trip time of the laser cavity. The dynamical interaction between the gain recovery mechanisms and the relaxation of the thermo-optically induced losses - both in the microseconds regime - can therefore lead to the sustained self-pulsing behaviour observed in Fig. 4.3(b).

Experimentally, the dynamical frequency shift of the resonator (and associated cavity losses) can be readily measured using a weak (<100 µW) counter-propagating CW probe laser, as illustrated in Fig. 4.1(a). In our case, depending on the spectral detuning of the

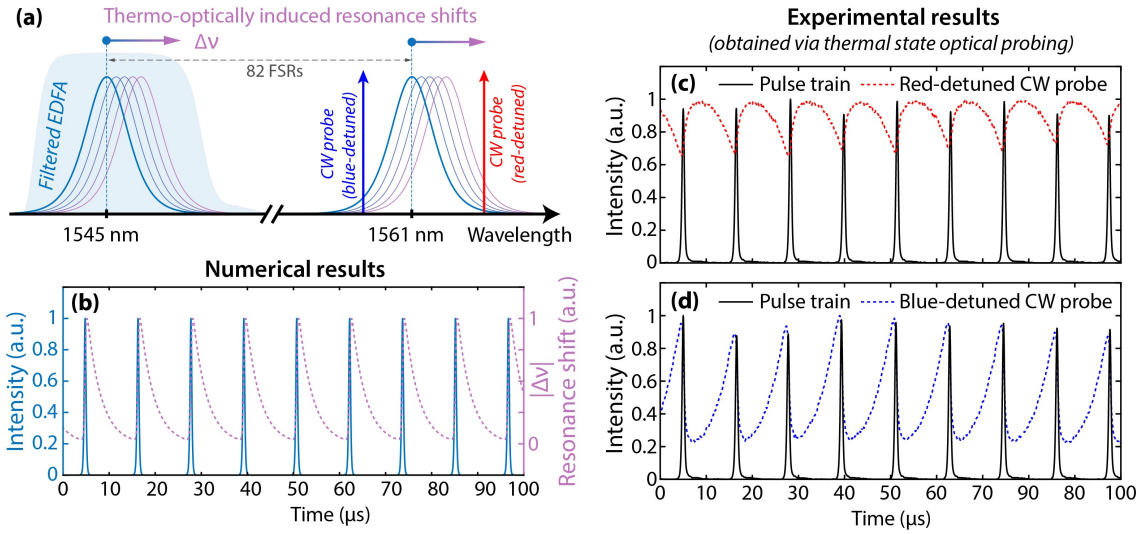

Figure 4.3: (a) Schematic of the physical process that leads to a thermo-optically induced slow self-pulsing emission of the laser. The thermo-optical nonlinearity of the microrod modifies the refractive index, and thus the resonance frequency of the micro-cavity, as the laser intracavity power increases. As the resonance shifts, the cavity transmission is reduced, leading to a reduction in power and eventually the repetition of the process, resulting in the pulsed emission. The loaded Lorentzian resonator mode within the filtered bandwidth of the EDFA (shaded blue region around 1545 nm) dynamically shifts by an amount $\Delta\nu$ via the thermo-optical effect (see gradient arrow and coloured shadings). This shift is also expected across all resonances and as such, can be readily measured experimentally using a CW probe weakly coupled and slightly detuned from a resonance far outside the main cavity gain bandwidth (see e.g. red and blue arrows around 1561 nm). (b) Numerical results obtained using the coupled mode equations of Eqs. 4.1-4.4 for parameters yielding self-pulsing $|a|^2$ (solid blue line - see Eq. 4.1) shows a train of pulses associated with a periodic resonance frequency shift $\Delta\nu$, induced by thermo-optical effects (dashed purple line - see Eq. 4.4). (c) Example of pulse train obtained experimentally (solid black line) and corresponding transmission of a red-detuned (dashed red line) CW field, used to retrieve the dynamical resonance spectral shift as shown in (a). (d) Same measurements using a blue-detuned CW probe (dashed blue line).

CW probe weakly coupled to the resonance around 1561 nm, a variation in the transmitted power is expected to be observed. In particular, as illustrated in Fig. 4.3(a), depending on whether the CW probe is red- or blue-detuned with respect to the resonance, one would respectively assume an increase or decrease of the transmitted power when the resonance is thermo-optically frequency shifted by the pulses emitted within the laser cavity. This behaviour has been experimentally measured in our setup, and reported in Fig 4.3(c) and 4.3(d), respectively. Stable self-pulsing is observed in the cavity (black line) while the CW probe exhibits a synchronous and periodic variation in the transmission whose sign and magnitude depend on its spectral position compared to the resonance (dashed red and blue

lines). In fact, the measured variation of the CW probe transmission here corresponds to the spectral convolution of the CW linewidth with the dynamically shifting resonance. Assuming a Lorentzian shape with a linewidth of 27 MHz (FWHM), and repeating these measurements for various CW detunings, we estimated that a typical 10 MHz spectral shift was observed for pulses circulating within the external gain cavity with an approximate 10 mW peak power. This corresponds to a thermo-optical frequency shift of approximately 1 MHz/mW, a value in line with the measurements reported in the literature for the spectral shift observed for fused silica rod resonators [211] and extrapolated to the 24 GHz FSR of the resonator used in our experiments. The spectral shift is dependent on the resonator's physical geometry as well as the Q-factor which directly affects the attainable field enhancement and, therefore, the impact of the nonlinear thermo-optical effect.

In order to gain further insights on the pulse formation mechanism, we perform an analysis of the generated pulse train properties depending on the main cavity static parameters. These results, obtained by varying the transmission (i.e. losses) and gain of the laser cavity both experimentally and numerically, are summarised in Fig. 4.4. From Fig. 4.4(a) and 4.4(b), respectively obtained by first setting the cavity transmission value using the VOA, and then increasing and decreasing the EDFA gain before repeating the process for a new transmission condition, one can notice a hint towards multistable behaviour: in this case, the pulse properties (i.e. durations and peak powers) not only depend on the current cavity parameters, but also on the previous state (i.e. gain increase/ decrease). Although various pulsing properties can be achieved for different transmission/ gain conditions, we have observed that higher cavity gain resulted in more intense pulses with a shorter duration. This result is in fact not surprising, as higher gain intrinsically implies a reduction of the load time required to induce a sufficient thermo-optical frequency shift of the resonance (responsible for additional losses in the cavity, and thus defining the overall pulse duration). This observation was confirmed experimentally by replacing the previous EDFA (Amonics, with length of 1.2 m and 23 dBm output saturation power) with a longer, higher power amplifier (HP-EDFA - MENLO P250, with length of 5.7 m and a higher saturation power of 27 dBm). In this case, the overall cavity round-trip was significantly longer but with similar losses and an FSR of 16.4 MHz for the HP-EDFA compared to 30.9 MHz with the previous EDFA. The reduction of the FSR below the resonator linewidth invited the possibility of multiple longitudinal modes lasing within one resonance. Experimentally, this effect was not observed, which is indicative that the mode competition favoured a single mode oscillation. The thermo-optical self-pulsing is achievable independently

of the cavity length, within this experimental range, with a suitable adjustment of the polarisation in the cavity.

Yet, as seen in the inset of Fig. 4.4(a), the higher gain accessible with the HP-EDFA further enables the generation of pulses with superior peak powers (and correspondingly reduced durations). Indeed, increasing the system losses also leads to a reduction of the pulse duration, as the thermo-optically induced frequency drift is dissipated faster by the higher losses in the main cavity. Interestingly, however, in the experiments reported here, the overall variation in the cavity losses are relatively small (within a single order of magnitude) and intrinsically limited by the gain range of the EDFAs used to observe self-pulsing. Within this experimental regime shown in Fig. 4.4(c), we can observe that the self-pulsing period is indeed directly related to the associated pulse duration, in a manner almost independent of the selected amplifier (and length, within this experimental range) but mainly depending on the gain value itself. These results are confirmed by numerical simulations as reported in Fig. 4.4(d), where we have observed that, for a fixed loss parameter α, the pulse duration and self-pulsing period were indeed correlated and readily controllable by adjusting the system parameters on the gain recovery time with respect to the resonator linewidth and its susceptibility to thermo-optical effects. In our numerical simulation, we observe stable self-pulsing behaviour for pulse periods between 6 µs and 14 µs, which agrees qualitatively with the experimentally observed range of parameters, spanning from 10 µs to 19 µs. The small discrepancy can be attributed to the absence of higher order effects such as the presence of the fibre nonlinearity in the model and slight discrepancies in the simulation parameters. Interestingly, the numerical simulations point out that the system still shows some self-pulsing behaviour also for pulses longer than 14 µs. These simulations were characterised by a long-term disappearance of the self-pulsing after thermalisation of the system, a condition which cannot be easily met in the experiment due to the presence of noise. Besides demonstrating the intrinsic control of the pulse properties dynamics, the clustering of the peak powers versus pulse periods shown by Figs. 4.4(a) and 4.4(b) and the dependence of the response to its previous state suggest the possible presence of multistable dynamics. Such a behaviour is investigated in more detail across our tunable parameter space in 4.5. As can be seen in Figs. 4.4(a) and 4.5(b), a greater amplifier gain does not necessarily correspond to an increase in the lasing intra-cavity power, which is in fact dependent on the history of the system. More importantly, this multistable behaviour can directly impact the operation mode of the laser. This can be observed by comparing the average power shown in Figs. 4.5(a) and 4.5(b) with the

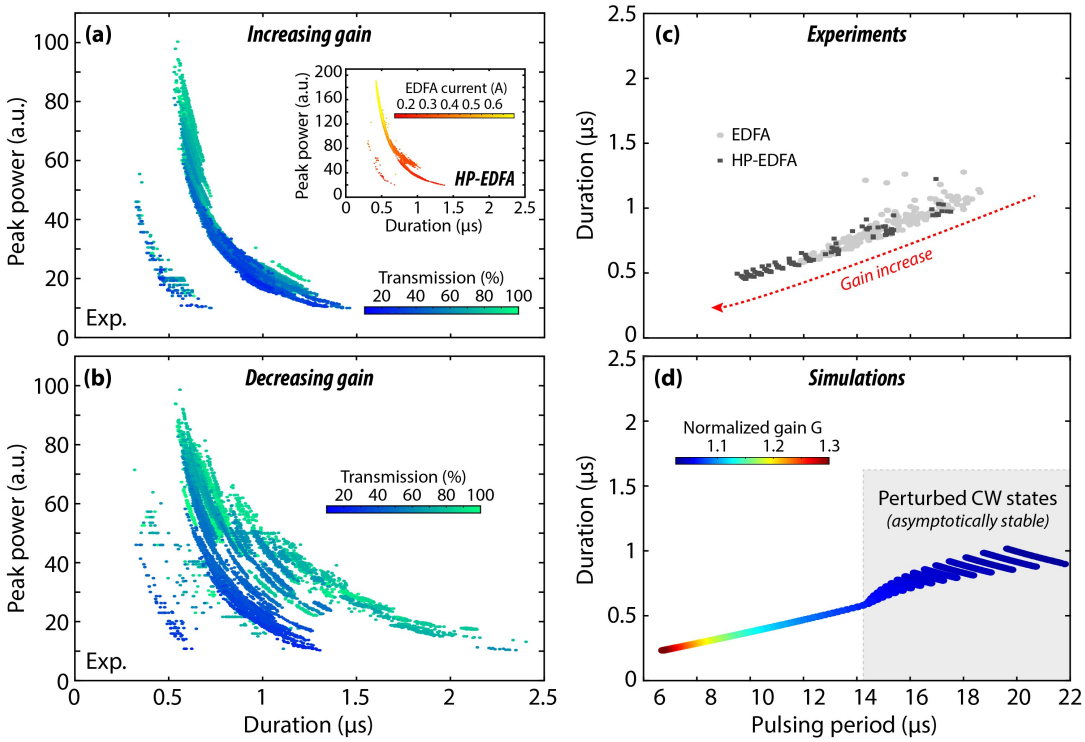

Figure 4.4: (a, b) Scatter plots of pulse peak power and duration obtained experimentally using the setup shown in Fig. 4.1(a). Here, data are extracted for various cavity transmission values (see colour scale, where 100 % transmission represents the minimum attenuation state of the VOA) and the EDFA gain settings, while increasing (a) or decreasing (b) the EDFA gain by adjustment of its pump current. The inset in (a) corresponds to the same scatter plot, obtained experimentally by replacing the initial EDFA in the setup by a longer and higher power gain medium (HP-EDFA). Here, the data are also obtained for various cavity transmission values while increasing the EDFA gain, but the colour scale instead represents the gain medium pumping current. (c) Scatter plot of the mean pulse duration and period obtained experimentally for various loss values and upward tuning of the gain. This analysis was performed using both available amplifiers (see legend) and by averaging the properties extracted from each ms-long experimental trace. (d) Corresponding properties retrieved from numerical simulations using a selected loss parameter α. Scatter points of the pulse properties are displayed for various values of normalised gain $G = g_0/\alpha$ (see colour scale). The numerical results are obtained using the coupled-mode equations of Eqs. 4.1-4.4 for selected parameters yielding self-pulsing behaviour. The pulse properties were extracted from the numerical field intensity via the same post-processing used on the experimental data sets. The grey shading region (featuring clusters of points instead of a point), corresponds to a dynamical regime where simulations exhibit self-pulsing only sustained for a limited period (i.e. in a slow transient ultimately leading to a stable CW solution).

corresponding peak power maps illustrated in Figs. 4.5(c) and 4.5(d): even when using the same set of loss and gain parameters, self-pulsing cannot be observed as easily when

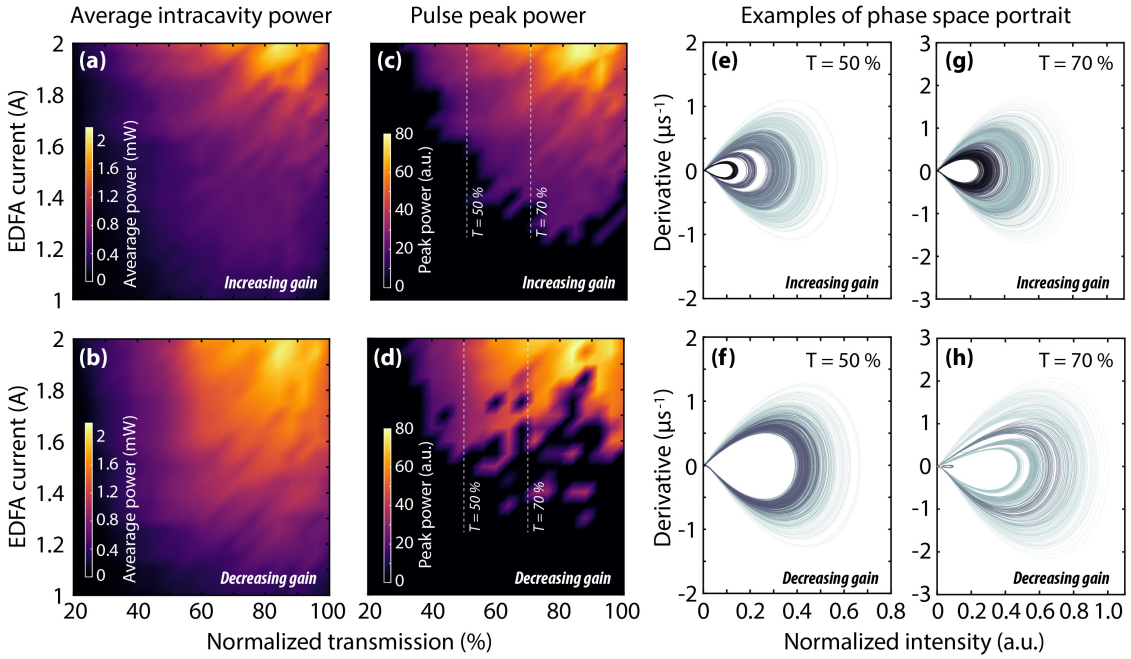

Figure 4.5: (a-b) False colour maps showing the average intra-cavity power (see colour scale) for experimental measurement of the laser cavity operation. Measurements are performed for a range of loss values while increasing (a) or decreasing (b) the gain. (c-d) Corresponding map of the pulse peak powers displaying clear regions of self-pulsing operation (i.e. black areas are representative of parameters for which self-pulsing is absent - see colour scale). (e-h) Examples of phase space portraits retrieved from experimental data measured at selected transmission of 50 % (e,f) and 70 % (g,h), respectively. As these panels show, we observe different self-pulsing conditions around the attractor when increasing (e,g) and decreasing (f,h) the gain, even for the same cavity parameters, thus attesting to a variety of multistable regimes.

approaching particular operation regimes with a decreasing gain; in this case, self-pulsing is lost early on, even though the cavity oscillation is featured with a higher average power - see Figs. 4.5(b) and 4.5(d). Such behaviours have been observed experimentally for a wide variety of conditions, leading to different discretisation of the pulsing dynamics around the attractor of the system, as illustrated in the phase portraits reported in Figs. 4.5(e) and 4.5(h). Physically, and besides small polarisation-dependent parasitic effects in our experiments, we attribute this behaviour to be predominantly associated with the known bistability of optically-injected resonators [147]. In fact, we have observed similar dynamics in our simulations, further suggesting that all-optical control of the pulsing operation can be reached, and the intrinsic multistability of the system further exploited.

To assess this possibility, we have conducted a proof of principle experiment using the same setup as the one shown in Fig. 4.1(a) but inserting a high-power counter-propagating

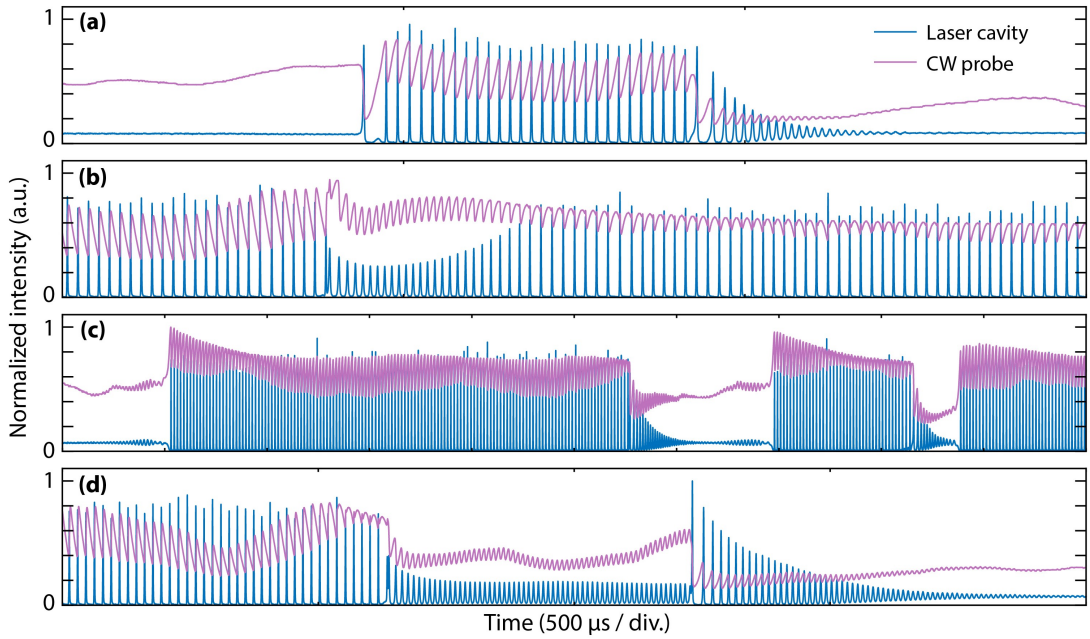

Figure 4.6: (a-d) Examples of experimental laser cavity dynamics observed when using a strong counter-propagating CW field (purple line) to both probe and influence the main cavity pulsing properties (blue line). The parameters of the main amplifying cavity are kept constant and a 15 mW CW probe around 1560 nm is coupled to the resonance but not frequency-stabilised. The drift of the CW around this resonance leads to a variety of slow-fast and multistable dynamics observed in self-pulsing and correlated to the CW field coupling, whose induced thermo-optical effects on the resonator properties can no longer be neglected. The panels show different regimes. (a) The CW detuning and associated coupled power initiates the self-pulsing. (b) A transient behaviour due to the passage from blue to red frequency detuning from the resonance. (c) Slow-fast dynamics associated with complex and threshold-like coupling behaviour. (d) Frequency doubling of the self-pulsing operation.

CW probe in the resonator. Differently from the previous configuration, the effect of the CW probe on the thermal and optical state of the resonator can no longer be considered negligible and it is expected to have a significant impact on the properties and dynamics of the main laser cavity. In particular, we used a 15 mW CW field to seed the resonance around 1560 nm while the main laser cavity was oscillating within the resonance located at 1545 nm and operating in a self-pulsing regime with an average power of 30 mW. Although the CW field possessed a power with the same order of magnitude as the lasing cavity (and thus expected to have a similar impact in terms of thermo-optical effects), we observed that similar self-pulsing properties could be maintained or recovered (via e.g. polarisation adjustments) over a large range of parameters when the CW coupling properties (i.e. frequency detuning and power) were experimentally stabilised. This can be understood by the fact that the thermo-optical shift induced by the CW field might, in this case, be

constant and only lead to an additional offset detuning in the laser-resonator coupling and operation (as long as the interaction between the CW and self-pulsing thermo-optical effects are small enough to avoid crossing any stability boundaries in the dynamical system - i.e. the typical cases shown in Figs. 4.3(c) and 4.3(d). However, when the frequency stabilisation of the CW probe is turned off, the CW laser can drift in and out of the resonance at the typical microsecond timescales at play in our system self-pulsing dynamics. Examples of such behaviours are shown in Fig. 4.6, where one can see that the fast modification of the CW probe coupling (purple line) drastically influences the main laser cavity self-pulsing dynamics (blue line). Depending on the conditions, variations on the CW detuning and associated coupled power can initiate self-pulsing (Fig. 4.6(a)), exhibit transient behaviour due to the passage from blue to red frequency detuning from the resonance (Fig. 4.6(b)), display slow-fast dynamics associated with complex and threshold-like coupling behaviour (Fig. 4.6(c)), or even yield frequency doubling of the self-pulsing operation (Fig. 4.6(d)).

These results clearly underline the capability of an external field to drastically influence the resonator state via the thermo-optical effect, and thus impact the pulsing dynamics of the system in a non-trivial manner. In this framework, we expect this architecture, displaying multistability with widely adjustable pulsing properties, to provide an excellent testbed for the experimental study of complexity in nonlinear optical systems, with timescales easily handled by conventional electronic systems. Considering the universal nature of the thermo-optical effect in microresonator devices, we anticipate that the self-pulsing dynamics observed here in fused silica should be achievable across other microresonator platforms when ensuring a correct and suitable selection of the cavity parameters. Additionally, our experimental observations using a CW probe have demonstrated the ability to transfer dynamics between multiple wavelengths and modify the pulsing state. This influence appears to be accurately controllable, thus opening up potential pathways for the wavelength-independent control and synchronisation of puling in multiple systems. For instance, by the CW laser acting as an optical control to mediate the interaction between two cavities to produce synchronised multicolour self-pulsing emissions and possibly taking advantage of multistabilities for wavelength-independent memory states.

4.4 Conclusion

We have experimentally demonstrated sustained self-pulsing driven by the complex interaction between the thermo-optical effect in a microresonator and the gain of an external

amplifying fibre loop. Numerical simulations provide direct insight on the dynamics of the thermo-optical frequency shift in the resonator and are in good qualitative agreement with experimental measurements made with an auxiliary probe laser coupled to the microresonator. The all-optical probe has been demonstrated to be a powerful tool for sensing the slow dynamics present in the micro-cavity, even during operation. In the future, we envision that this approach will be useful in monitoring and diagnosis for operating states of such a laser, especially as a simple approach for monitoring stability of such a device. Our system exhibits a multitude of interesting multistable dynamics and we have experimentally investigated the effect of a probe field with non-negligible power, with results hinting towards possible applications in complex lasing and nonlinear dynamics, with modes that can be linked by thermally-dependent and adjustable effects.

Chapter 5

Spontaneous emergence of laser cavity-soliton microcombs

The processes that govern the formation of nonlinear dissipative structures are, by their very nature, complex. Such structures have been studied in many biological, chemical, and physical systems. In photonics, the formation of microcombs is of significant interest for the development of modern optical technologies with applications spanning spectroscopy, telecommunications, and metrology, among others.

A key open problem in the field is in the development of agile protocols for the start-up procedure to generate and stabilise soliton microcombs. In their typical implementation, which is based on externally-driven microresonators and described by the Lugiato-Lefever model, microcombs require an active and precise perturbation to the external pump laser in order to trigger their formation. In stark contrast to well-established modern frequency combs, based on passively mode-locked lasers, these solitons do not spontaneously appear from noise, nor can they be recovered after being destroyed by a perturbation.

Here, we show that laser cavity-soliton microcombs in a microresonator-filtered fibre laser can emerge and recover directly from noise. We experimentally define and map their existence region against a simple set of static cavity control parameters, namely the optical amplifier pump level and the main fibre-cavity length - in direct resemblance to existence maps of pulsed regimes in passively mode-locked lasers. Such a map is remarkably repeatable and underpins a robust set of soliton states, which are always recovered after being disrupted, when the system is properly set.

We verify the spontaneous start-up and recovery mechanism exhibited by our system with real-time measurements of the microcomb output during the transition, and present evidence supporting the role of nonlocal thermo-optical nonlinearity in enabling the spon-

taneous emergence of soliton waves.

5.1 Introduction

In nonlinear dissipative systems, far from equilibrium, self-organisation can lead to the formation of complex structures [85, 147]. This macroscopic behaviour is governed by decentralised, global conditions, and as such the emergent state is typically robust to localised perturbations. Passively mode-locked lasers are an important physical example of such a dissipative system [85]. Understanding the global parameter settings and proper start-up protocols required to access the region of existence of these states has been crucial to the development of modern ultrafast laser technologies [212].

A well-known problem to this development has been in how to reliably enter the pulsed regime in lasers that are mode-locked by a fast saturable absorber. To ensure reliable start-up, these lasers often incorporate an additional slow saturable absorber to help to force the system into the desired state during the start-up procedure [37]. This problem remains open, however, in the field of microcombs. The realisation of a robust, repeatable approach for self-starting operation into the temporal cavity-soliton (CS) regime is a focus of present research in the field [105, 107, 118, 120, 136, 191, 213]. Cavity-solitons [147, 214] are a unique and important class of dissipative soliton which harness the high optical field enhancement of microresonators to balance dispersion with the nonlinear phase shift at low average powers, and are consequently seen as key components for important developments to metrology, telecommunications and quantum science [102, 132, 134, 137, 139, 173]. Within this class, temporal laser cavity-solitons [90, 121, 122, 149, 153, 214] are the most efficient type solitary wave and have been recently implemented in a microresonator-filtered fibre laser [1]. These broadband solitary pulses are sustained by the gain of the laser, in contrast to standard configurations where CSs are sustained on top of a strong background by an external driving laser.

The phase and group velocity mismatch between the two cavities of the microresonator-filtered fibre laser, as well as the gain level of the amplifying fibre are the experimental global parameters across which we may define a region of existence of these solitary waves. For microresonators with focusing Kerr nonlinearity and anomalous dispersion, CSs are only found for comb lines oscillating on the red-detuned slope of the microresonator resonances [2, 215].

A red-detuned configuration alone is, unfortunately, not sufficient to induce the formation of stable solitary pulses. Since CSs are *localised pulses*, a large portion of the nonlin-

ear microcavity remains in a stable background state. The implication here is that it is impossible to find a single set of global parameters which allow for CSs to start-up spontaneously from the background state and then be maintained. Instead, the soliton must be 'written' into the cavity by a direct perturbation to one of the cavity parameters [90, 91, 214]. A complex start-up procedure is necessary in standard Lugiato-Lefever systems to pass-by this fundamental limitation. One possible solution here is to use a succession of solitary peaks, soliton crystals or period successions, which are allowed to start from noise in certain regions of the Lugiato-Lefever equation or in modified versions of it [215] although, strictly, single soliton states are not allowed in these configurations.

In principle, an additional, slow and energy-dependent nonlinearity could break this deadlock with the benefit of adding robustness to the system in a similar manner to the slow saturable absorber used in passively mode-locked lasers for start-up. In simple terms, the microcomb would be configured with a set of starting parameters where the background is unstable and hence the noise can grow, starting-up the oscillation. As the energy of the state increases, however, the parameters are nonlocally modified by the energy-dependent nonlinearity; if such a change moves the system into their region of existence and stability, solitons are eventually formed and maintained.

Controlling such an effect in externally driven configurations, however, is not trivial - only very recently has soliton start-up been observed in lithium niobate resonators: this material naturally displays a nonlocal, defocusing, photorefractive nonlinearity which pushes the system into a red detuned configuration [216]. Many common microcavities, conversely, are dominated by a focusing thermal nonlinearity, which pushes the system into a very well-known, strongly locked configuration on the blue detuned slope of the microresonator [168]. Here, unfortunately, solitons do not exist, and only Turing patterns are admitted.

While microcomb designs integrating both laser and microcavities are becoming increasingly popular [118, 127, 136, 191], the mechanism of temporal CS formation in these systems is still under intense study [119, 217] and, in particular, the mechanism which drives the formation of laser CSs in the microresonator-filtered fibre laser, has been, so far, unknown.

The results of the following section detail how, experimentally, laser CS states are accessed, as well as presenting results to demonstrate the impact of the cavity global control parameters on the accessible regimes.

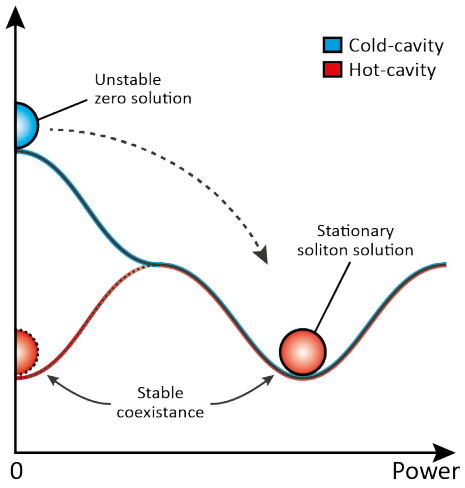

Figure 5.1: Illustration of the concept of a nonlocal nonlinearity permitting a self-starting, globally stable system. The change in stability of the stationary states for 'cold' and 'hot' cavities. The oscillating field grows from the initial modulational instability (MI) present in the zero energy state, and under the proper setting of global cavity parameters, evolves towards the stable soliton state. In this energetic regime, the global cavity settings are impacted by the nonlinearity such that the zero energy solution is shifted to detuning away from the MI region where the background state is stable and soliton solution is maintained.

5.2 Mapping the soliton regime

The experimental setup is built by nesting a silicon-oxynitride integrated ring-resonator, with ∼49 GHz FSR and a 1.3 million Q-factor, in add-drop configuration into a remotely controllable amplifying fibre cavity. This main-cavity comprises a polarisation maintaining optical amplifier and a free-space section containing a motorised delay line, polarisation control optics, and a 12 nm bandpass filter. The polarisation optics are set to minimise the cavity losses for the map presented in Fig 5.3. The FSR of this cavity is 77 MHz.

The operating state of our microcomb laser is characterised simultaneously by measuring its optical and radio-frequency spectra, respectively by an optical spectrum-analyser (Anritsu) and a fast oscilloscope. The average pulse envelope is measured by a second-harmonic non-collinear temporal auto-correlator (Femtochrome). Furthermore, the absolute frequency of the oscillating microcomb laser lines is measured using the laser-scanning spectroscopy technique, in the same configuration to that described in Chapters 2 and 3, with the addition of a gas-cell for referencing the absolute frequency axis. Each instrument is interfaced with a computer-controlled program for synchronised and automated acquisition.

The parameter space is spanned in order to map the microcomb states against the 980 nm pump power of the Erbium-doped fibre amplifier (EDFA) and the relative length of the main-cavity (by the motorised delay line), while monitoring temperature and losses of the system. Such a systematic analysis was possible thanks to an automated laser setup which permitted repeatable scanning and measurement.

The scan is conducted by first setting the cavity detuning position, with the EDFA pump turned off, and then ramping the pump power up to the region of interest. Here, the cavity regime for the mapped set of input pump powers is measured, using all characterisation techniques described previously. The pump laser power is then increased by 1.3 mW and the process is repeated until reaching the maximum setting. Upon completion of the set, the amplifier is turned off, and the procedure is repeated for the next cavity-length setting. The entire scan is performed over several hours, during which time the setup is isolated to environmental perturbations and, in particular, the temperature of the environment around the microresonator is maintained by a PID controlled heater, which is stable to $\pm 1\,^{\circ}\mathrm{C}$.

The experimental results presented here clearly shows a region within the cavity global parameters (cavity length, laser pump power, temperature and losses), where the solitons are spontaneously formed and robustly locked against perturbation without any additional external feedback (Fig. 5.2 and Fig. 5.3). Very importantly, this mechanism appears phase independent, implying that it is robust to small changes of the optical path and does not require to adjust the position of the resonances in the order of the optical wavelength.

For a given temperature and set of losses, this region is found by harmonically matching the free-spectral ranges of the micro- and main-cavities and appears for a well-defined range of pump power levels of the fibre amplifier. The laser, configured in the proper state of global parameters, always generates, and recovers after perturbation, temporal CS whose number is practically determined by the saturation energy of the gain. Importantly, this means that direct access to single solitons is permitted.

We are able to clearly identify a region in which the system is always admitting soliton states. This region persists across a variation of the main cavity path length well-above its FSR, with soliton states always displaying a clear red-detuned central comb line. It is worth noting that the states found in this region are not necessarily composed of the same number of solitons.

Figure 5.2(a) reports a typical map, which was obtained by increasing the gain pump power from low to high values. The maximum spectral bandwidth obtained by the OSA is

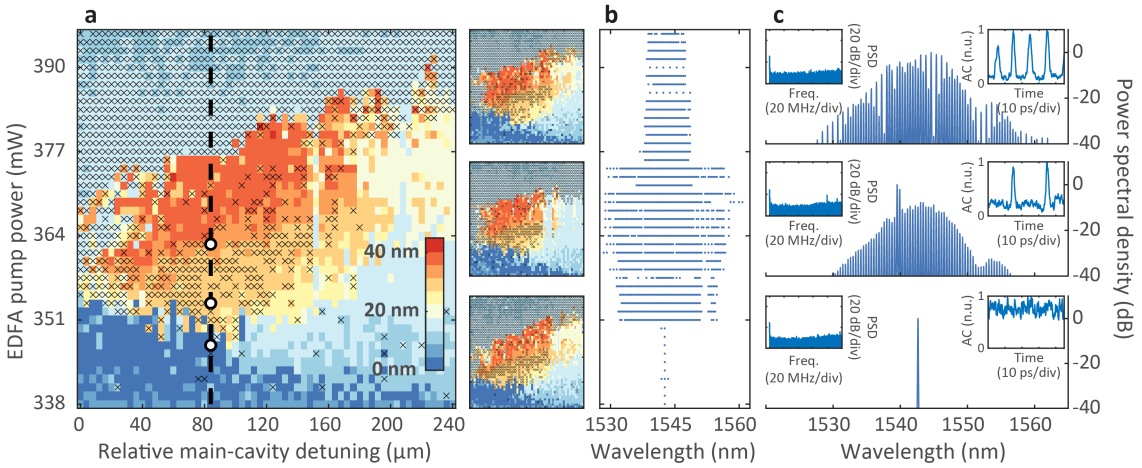

Figure 5.2: (a) The spectral bandwidth of the laser output, corresponding to the colour scale inset, for various settings of the cavity global parameters - namely cavity length and amplifier pumping voltage. The temperature was kept within a fluctuation of few degrees at 20 °C. The soliton states with the largest bandwidth and are clearly identified in the orange/red region in the centre of the map. In the lower left section of the map, a stable region admitting CW/Turing pattern states is clearly identifiable. The radio-frequency spectrum is analysed to identify unstable regions of the map and are marked by a cross. The insets to the right of the map are repeat measurements of the entire scan acquired over a continuous 40 hour period. (b) The wavelength of each spectral mode is plotted for the fixed cavity length of 84 μm (dashed black line in (a)). The pump power increment is 1.3 mW, and the spontaneous transition from a CW state into the single soliton state is clearly identifiable. (c) Example measurements of the lasers optical spectrum, radio-frequency and autocorrelation traces are presented for 347.1 mW, 353.6 mW and 362.7 mW (indicated by the white circles in (a)). Here we observe both single- and two-soliton states, as well as CW operation.

represented in this parameter space as indicated by the corresponding colour bar. Regions where the DC bandwidth of the signal exceeds a threshold of 500 kHz or the beat note at the super-mode frequency exceeds 1 MHz (which indicates that the system is in a slow pulsing regime), are marked by a cross. Among this set of unstable states, which we will not further investigate here, we could clearly identify two distinct regions that were always admitting CW/Turing states and soliton states.

Practically, a range of environmental factors can impact the operating state of a laser - commercial devices incorporate active cavity stabilisation techniques such as piezo-controlled fast cavity-length actuation for locking desired regimes. It is important here to highlight that presently, the microresonator-filtered fibre laser is completely free-running. Even still, we observe a remarkable level of repeatability in our measurements. The measurements presented in Fig. 5.2(a) were conducted a total of four times with the same

scanning acquisition script. It is clear from theses repetitions (See the three insets directly to the right of Fig. 5.2(a)) that the soliton region is consistently present and is generally admitting the same number solitons.

These measurements were acquired over a continuous 40-hour period, with each dataset taking approximately 10 hours to complete. The length of such measurements means that the system is subject to fluctuations of the laboratory temperature across the full day-night cycle, which practically fluctuates by a few degrees Celsius around 20 °C.

As the EDFA pump power is increased, we observe the laser state evolving directly from CW operation into the single-soliton state, then into the two-soliton state. The optical spectra, taken along a single setting of the main-cavity length, are presented in Fig. 5.2(b). Here we see a dot to indicate each detected peak in the optical spectrum. The state evolves freely from a blue-detuned CW state, with very few spectral lines, directly into a stable single soliton state. As the EDFA pumping power is increased, the spectral bandwidth appears to increase and eventually the saturation power reaches a level that is sufficient to sustain two solitons, which manifest spontaneously. The spectra of example cases of the CW, single soliton, and two soliton regimes are presented in Fig. 5.2(c). The insets detail the corresponding RF spectrum and the auto-correlation trace. The clean RF spectrum and high extinction ratio of the background in the auto-correlation traces is indicative of the strong coherence of these states.

Figure 5.3 reports a similar set obtained for a different setting of the cavity losses in which the soliton regime is observed for higher intracavity powers. We observe the laser state evolving directly from Turing pattern operation, with lines five free-spectral ranges apart, into three-soliton states. The first clear distinction between the two maps of Figs. 5.2 and 5.3 is the difference in the number of solitons that are admitted in the cavity. The map of Fig. 5.2 admits only single- and two-soliton states, whereas the map of Fig. 5.3 shows both two- and three-soliton cases. The number of solitons can be identified by the number of peaks in the autocorrelation traces, in conjunction with the spacing and modulated patter of the comb lines in the optical spectra. In fact, the modulation of the optical spectra (seen clearly in the top spectra in Fig. 5.2(c)) makes it quite apparent that the spacing between multiple soliton pulses in the cavity are not perfectly equidistant, which is illustrative of the localised nature of solitons. In the case where multiple solitons are maximally separated, one would expect a corresponding optical spectra with a modulation period equal to the N time the micro-cavity FSR, where N is the number of pulses. This is indeed the case shown in the middle spectra of Fig. 5.3(c) for $N = 3$. For the cases where

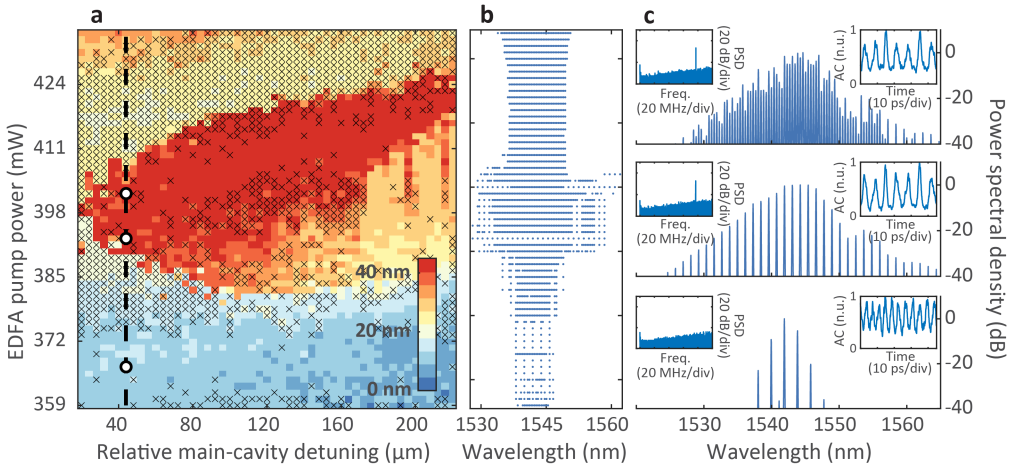

Figure 5.3: (a) The spectral bandwidth of the laser output, corresponding to the colour scale inset, for various settings of the cavity global parameters - namely cavity length and amplifier pumping voltage. Temperature was kept with a fluctuation of few degrees at 20 °C. The soliton states the largest bandwidth and are clearly identified in the orange/red region in the centre of the map. The radio-frequency spectrum is analysed to identify unstable regions of the map and are marked by a cross. (b) The wavelength of each spectral mode is plotted for the fixed cavity length of 44 µm (dashed black line in (a)). The pump power increment is 1.3 mW (c) Example measurements of the lasers optical spectrum, radio-frequency and autocorrelation traces are presented for 366.8 mW, 392.8 mW and 401.9 mW (indicated by the white circles in (a)). Here we observe three-soliton states, with 5-FSR non-localised Turing patterns.

the solitons have an uneven temporal separation, the optical spectra present interference fringes such as those in the top spectra of Fig. 5.2(c).

5.3 Phase resilience of the solitary solutions

These results highlight a strong resilience of the system on the initial phase mismatch between the two cavities. The amount of phase detuning covered in these maps over the range of the delay line is exceptionally large. The detuning is, however, also subject to the thermo-optical effect [3]. Due to the large thermal coefficient of the microresonator ($1.7 \times 10^{-5}\,\mathrm{K}^{-1}$ - equating to a spectral shift of 14 pm °C^{-1} [218]), the detuning is changed as the intracavity power is increased. Across the soliton region, such a shift well exceeds the FSR of the main cavity (77 MHz or 0.62 pm), as shown in Fig. 5.4(a) and 5.4(b). The implication here is that in order for the soliton region to be so large, there must be some dynamical mechanism which is always maintaining the red-detuning of the lasing main-cavity modes as the micro-resonance is significantly thermally detuned. This mechanism

must, in-part, pertain to an energy dependent effect acting on the main-cavity such as a thermo-optical effect or the refractive index response to the amplifier gain [219–222].

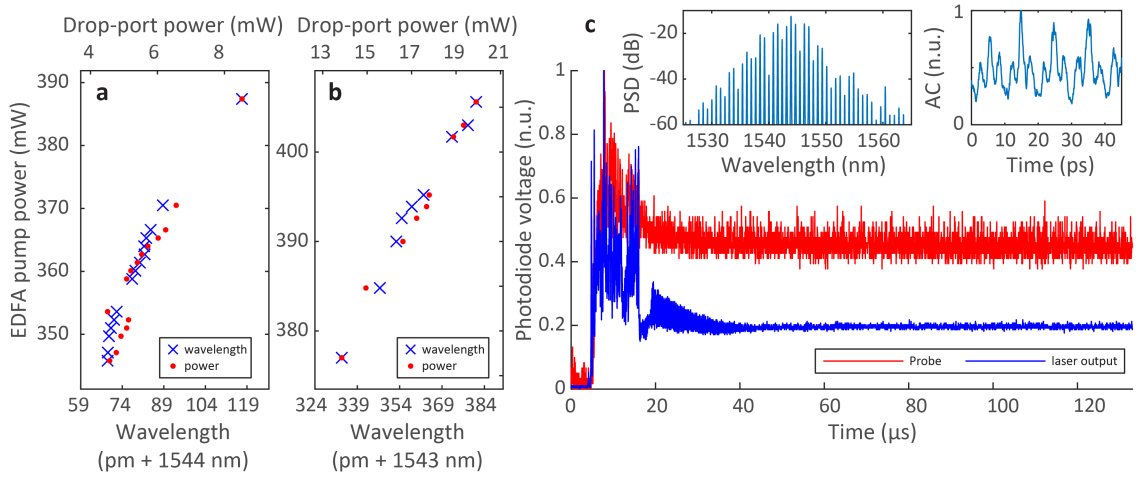

Figure 5.4: (a) Wavelength detuning of the central lasing mode in the soliton region versus laser pump power, exceeding the free-spectral range (0.62 pm) of the laser cavity for the case in Fig. 5.2, along with intracavity power at the output drop port of the microcavity. (b) Same for the case in Fig. 5.3. (c) An example of recovery from perturbation of soliton state. Measured drop power (blue line) shows the transition from the laser off-state, after a mechanical perturbation to the stable soliton, and then the recovery of a stable state. The spectra (inset) measured shows the recovered soliton case and corresponding auto-correlation trace. The power of a weak CW probe (red line), coupled in the 1560 nm microresonator resonance, is shown to measure the nonlinear shifting of the microcavity during the formation process.

This effect is quite apparent in Fig. 5.4(a) and Fig. 5.4(b), which show the position of the central spectral mode, at fixed delay line settings, as the EDFA pump is increased. The wavelength of this central mode increases by over 30 pm while the soliton state is maintained. The corresponding measured intracavity power is indicative of the energy dependence of this phenomenon.

Moreover, the soliton states were very likely to be recovered after a perturbation (e.g. mechanical) to the system. A typical variation of the output power of the laser after the perturbation of a soliton state is reported in Fig. 5.4(c). To measure the change of the physical property of the microcavity resonance, we probed a resonance with a weak CW laser in order to observe the change in coupled probe power (In a manner similar to the works of Chapter 4). The variation of the transmitted power, along with the formation of the soliton state, shows clearly that the microcavity resonances are strongly detuned during the soliton formation process before passively self-locking into the soliton state. The insets show the optical spectra and auto-correlation trace of this soliton.

Within the scope of the relative cavity detuning parameter, the implication is that the delay line is prevalently controlling the free-spectral range mismatch between the two cavities. The existence region of the solitons is wider when the main fibre cavity is an exact multiple of the microresonator length and is completely extinguished for significant changes of cavity length. Turing patterns, conversely, appear for mismatched cavities and are well spread even beyond this map (As seen in the works presented in Chapter 3). The soliton range moves towards higher pump powers when the relative main-cavity length is increased. This indicates a decrease of the refractive index with pump power, which appears to be dominated by the gain response of the Erbium over the focusing thermo-optic effect [219–222].

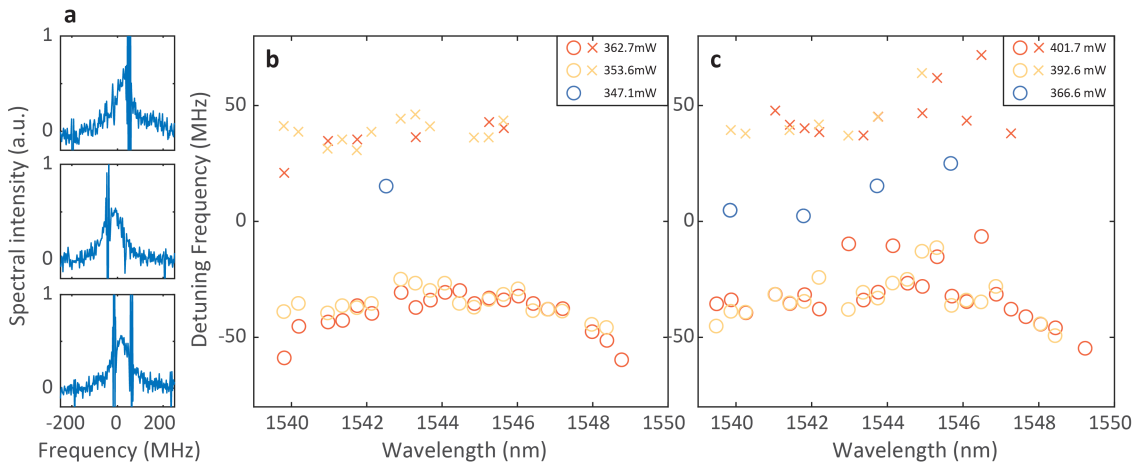

Figure 5.5: Dispersion of the oscillating lines within the microcavity. (a) Typical laser scanning spectroscopy measurements of a blue detuned oscillating line (top), red detuned line (centre) and coexistence of two oscillating modes (bottom). The detuning is calculated as the frequency difference between the centre of the microcavity resonance and the oscillating line. (b) Distribution of the detunings for the spectral modes in the example cases of Fig. 5.2(c). The primary oscillating laser lines are marked with a circle, while the secondary resonance, if any, is marked as a cross. (c) Distribution of the detunings for the modes in Fig. 5.3(c).

The resilience of the system from the initial phase mismatch of the cavities points towards the presence of a dynamical mechanism which prevalently locks the laser lines on the blue or red detuned slopes of the microcavity. Such relative detunings are shown in Fig. 5.5, which reports the measured positions of the lasing modes within the microcavity resonances, versus mode wavelength. The three example resonances shown in Fig. 5.5(a) are illustrative of a blue-detuned mode (top), a red-detuned mode (middle), and a coexisting state (bottom). The data in Figs. 5.5(b) and 5.5(c), then, corresponds to the maps of 5.2 and 5.3 respectively. The laser scanning spectroscopy measurements

reveal the relative detuning, over all lasing lines, for each lasing mode of the comb. For a fixed length of the main-cavity, starting from low to high pump power, we first find blue detuned states corresponding to the CW/ Turing waves, with the mode wavelength and relative detuning from the microresonator resonance indicated by the blue circles. When we enter in the soliton region, we observe a set of red-detuned modes, corresponding to soliton states spanning over the whole range of the observed wavelengths. In these cases, a smaller secondary mode, coexisting with the soliton modes, is sometimes observed [165]. These few blue detuned lines are marked with a cross, and are typically significantly less notable than the red-detuned lines. The exception here is to the couple of laser lines at and below the 1540 nm range. For these comb lines, the coexisting blue-detuned line is large, as shown in the bottom example resonance profile in Fig. 5.5(a). The presence of such lasing modes can be understood within the context of the dynamical and self-acting feedback that is present in the two cavities system due to the nonlocal nonlinearities.

As discussed in the introduction, an energy dependent, nonlocal nonlinearity can contribute to self-lock the system on a specific slope of the microcavity [168]. Very importantly, in a microresonator-filtered fibre laser system, where energy dependent nonlinearities are prevalent in both the main- and micro-cavities, such a locking point depends on the relative nonlinear frequency shift between the two cavities. Considering a predominantly focusing effect for both, when the thermal nonlinearity of the micro-resonator dominates, the lasing modes will lock on the blue slope of the microresonator, but when the system is dominated by the nonlocal nonlinearity of the amplifier, the modes will lock on the red slope, remarkably permitting soliton start-up and recovery. This dynamical system, with a strong thermo-optical nonlinearity in the microresonator, enables us to set the system in a regime where instabilities of the background states can grow spontaneously, due to modulational instability gain, but will lock once the cavity is 'hot' and the nonlocal nonlinear effects shift the absolute detuning of the two cavities. The periodical nature of the multi-modal system enables a certain redundancy with respect to the detunings of the two cavities. There is always a main-cavity mode in close spectral proximity with the micro-cavity resonance.

In particular, this phenomenon is quite evident in the resonance profile showing coexisting blue- and red-detuned modes at the bottom panel of Fig. 5.2(a). As noted, this case distinctly appears at comb lines below ∼1540 nm. We can attribute this appearance of blue-detuned states to the well-known wavelength-dependent behaviour of the refractive index in heavily-doped Erbium fibres [220, 221]. Notably, because the gain saturates with

the circulating laser power within the fibre cavity, the refractive index dependence on the circulating laser power is defocusing for wavelengths shorter than that of the resonance peak, and focusing for longer. In the EDFA used here, the resonant peak is at ∼1538 nm (see Refs. [220, 221] for experimental measurements the refractive index dependence on signal power in EDFAs).

In terms of the nonlocal self-locking behaviour in the microresonator-filtered fibre laser, the implication is that stable states are preferentially locked in blue detuned configurations for wavelength shorter than ∼1538 nm, where the laser gain refractive is nonlinearly defocusing, and on red-detuned configuration for wavelength longer than such a value, where the laser refractive index is focusing. It is important to highlight that a thermal nonlinearity is certainly also present in the amplifier cavity, which however, is expected not to show any wavelength dependence.

This factor contributes significantly in determining the presence of other states coexisting with the localised solitons. When the intracavity energy of the soliton alone is insufficient to saturate the laser gain, energetic background states emerge and appear to coexist with the soliton in the cavity. This is quite evident in the cases for the single soliton (Fig. 5.2(c) - middle), which clearly show two strong laser lines in the spectrum at ∼1538 nm. Such behaviour has indeed been observed in other works in the field [165, 223], where a peak at the resonance frequency of the optical amplifier is often observed.

5.4 Real-time observation of spontaneous laser cavity-soliton emergence

To obtain some insight into the dynamics at play with regard to the spontaneous emergence of the soliton state, we implement a modulated dispersive Fourier-transform spectroscopy setup to examine the evolution of the optical spectra in real-time. Real-time measurements of ultrafast optical phenomena are becoming ever more prevalent in the field, especially with regard to gaining insight into the formation processes and transient dynamics in ultrashort pulsed regimes [224–229].

Dispersive Fourier-transform (DFT) spectroscopy is usually implemented by passing the laser pulses through a length of dispersion compensating fibre (DCF). The chromatic dispersion is utilised to stretch out the temporal pulse, separating the distinct spectral components of the pulse, which can then be detected with a fast oscilloscope - providing that the propagation is sufficient to satisfy the far-field approximation of temporal disper-

sion [230].

An additional challenge is presented in making such a measurement for the laser cavity-solitons in a microresonator-filtered fibre laser. Since the repetition rate of these ultrashort pulses is at least 50 GHz (i.e. in the single soliton case) a stable pulse train undergoing the spectral stretching of the dispersive fibre would interfere with itself, distorting the spectral lines in the noise. In order to overcome this, we apply an electro-optic modulation (EOM) to the pulse train in order to isolate and select just a few pulses, which are then sufficiently separated from the next pulse window to perform the DFT measurement. A schematic of the full setup is presented in Fig. 5.6(a). The pulse train signal from the microcomb laser is optically isolated, to ensure no disruptive feedback, and the polarisation is matched to the EOM to ensure the maximum of the signal is transmitted to detection. A square modulation wave is applied to the pulse train, with an open window duration of 300 ps, and a window separation period of 31.3 ns. The transmitted block of pulses then passes through the length of DCF which compensates the amount of dispersion equivalent to 80 km of fibre. The total dispersion of the DCF is $D = -1360\,\mathrm{ps\,nm^{-1}}$. The induced temporal spreading must be lower than the periodic separation of the pulse windows set by the EOM. The final signal is then amplified with an in-line semiconductor optical amplifier to enable measurement of the signal by a 16 GHz photodiode. The optical spectrum of the microcomb output is measured adjacently by an optical spectrum analyser for direct comparison to the real-time spectrum. The concept behind this scheme is illustrated in Fig. 5.6(b).

By making some perturbation to the stable microcomb operation (e.g. mechanical), we are able to annihilate the stable soliton state and then actively observe its real-time spontaneous reformation. Figure 5.7 shows an experimental measurement of this. Figure 5.7(a) shows the oscilloscope trace for the output power of the microcomb, in the same manner as in Fig. 5.4(c), for direct comparison with the DFT measurement shown below in 5.7(b). Here, we plot the experimental measurement in 2D, where the colour scale is normalised to the maximum observed output power in the trace. The vertical 'slow axis' set to the repetition rate of the EOM. In this manner, each vertical 'slice' of the full oscilloscope measurement shows the spectrum for a single window of pulses. The horizontal axis, then, shows how the spectrum of the pulse train evolves in 'fast time'. During the chaotic formation period, the central line of the emergent comb appears dominantly. The dynamics of the formation observed occur over $\sim$10 µs. We note that this is in line with the typical response timescale on which the thermo-optical effect operates in silica-based

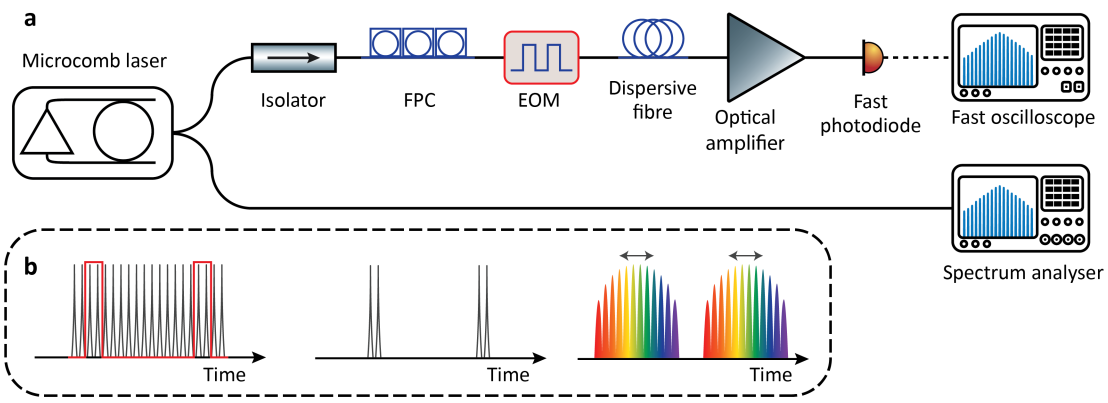

Figure 5.6: (a) Schematic of the modulated dispersive Fourier-transform spectroscopy (DFT) setup. The microcomb pulse train passes through an optical isolator and fibre polarisation controller (FPC) before an electro-optic modulator (EOM) is used to window and select a few pulses. The microcomb repetition rate is in the 50 GHz to 100 GHz range, so each 300 ps window contains tens of pulses. These pulses are then propagated through a length of dispersive optical fibre. The temporal separation induced by the dispersive fibre, is orders of magnitude greater than the initial temporal separation of the individual pulses; thus interference between multiple pulses is insignificant in measurement. The signal is amplified before being detected by a fast photodiode (EOT - 16 GHz) and oscilloscope (Teledyne Lecroy - 36 GHz). (b) Illustration of the measurement concept. The microcomb pulse train (black) is windowed by the EOM (red), before passing through a significant length of dispersive fibre to reach the far-field Fourier-transform limit where spectral components are effectively mapped to the temporal domain.

microresonators (see Chapter 4). This result supports the hypothesis that the nonlocal thermo-optical nonlinearity, induced in the 'hot' cavity condition, is one of the key components in the formation and the stabilisation dynamics of these laser CS microcombs. The inclusion of this thermal detuning into the numerical propagation model should be able to verify such behaviour, and this work will be conducted in future theoretical studies.

In conclusion, laser cavity-solitons have been demonstrated to spontaneously emerge in a microresonator-filtered fibre laser. We identified a region of global parameters such as cavity length, losses, temperature and EDFA pump power, where these solitary pulses exist and are stable. This region is remarkably repeatable also in terms of the number of formed solitons which are obtained independently on the initial phase detuning between the two cavities, instead depending on the saturation energy of the cavity gain, which in this case is primarily controlled with the EDFA pumping power. In this framework, we discussed the role of the nonlocal nonlinear thermo-optical nonlinearity in the system, and the complex dynamical interplay between the nonlinearities of the two cavities, which

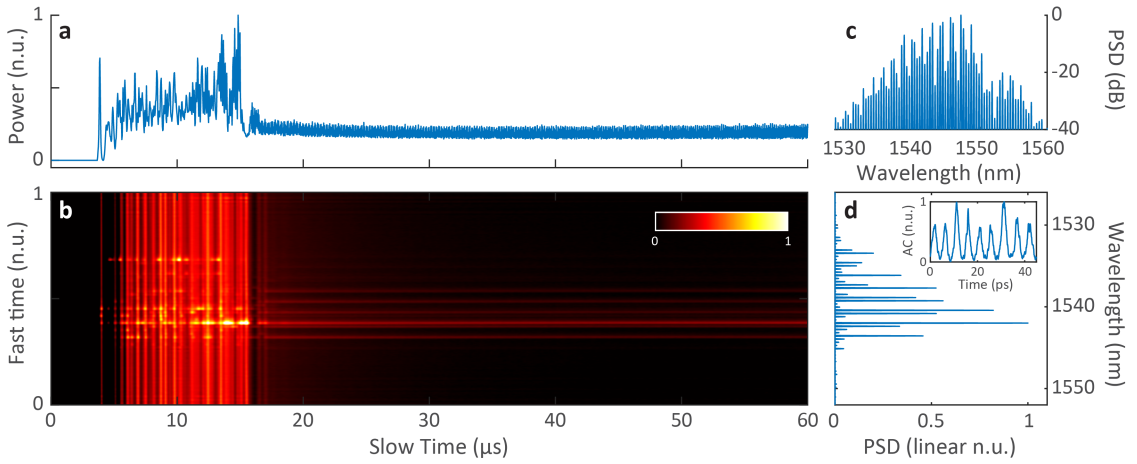

Figure 5.7: (a) The temporal DFT measurement is plotted in a 2D figure, with the fast-time axis (determined as the period of the EOM) in the y-axis and the slow-time axis on the x-axis. The measurement illustrates the spontaneous formation of a soliton state from the 'off' state. The normalised average energy of the signal is shown above. A period of apparent chaos, the duration of which is in-line with the response time of the microresonator thermo-optical effects, is followed by settling into stable soliton operation. The linear optical spectrum corresponding to this stable state is shown to the right of the 2D plot, with the corresponding autocorrelation shown in the inset. For reference, the log-scale optical spectrum is shown above.

under appropriate conditions, appears to enable the laser spectral modes to self-lock in a regime where solitons exist (i.e. a relatively red-detuning of the main-cavity mode with respect to the microresonator mode). In this regime, the stable soliton state is demonstrated to self-start from noise, with experimental measurements of the optical spectrum and intracavity power during start-up supporting this.

These capabilities, together with the high efficiency generation and background free operation of laser cavity solitons, make a microresonator-filtered fibre laser a viable approach for a robust, user friendly microcomb technology.

Chapter 6

Summary and future perspectives

Microresonator-based frequency combs have seen tremendous success over the past decade, and the future looks bright, extrapolating from the progress in micro-fabrication techniques and integration of these devices. In particular, the integration of lasers and microresonator on a single platform is the ultimate aim within the field. Significant progress is already being made towards this and, in particular, novel configurations are under intense research to overcome some of the limitations of the conventional externally-driven microcombs based on the Lugiato-Lefever equation (LLE).

In this thesis, I have investigated the lasing regimes that can manifest in one such configuration: the microresonator-filtered fibre laser. The dynamical interplay between the nonlinear high-Q microresonator and the amplifying fibre cavity is certainly an interesting physical base for a range of complex and dynamical physical laser phenomena.

Temporal laser cavity-solitons are a new class of pulsed laser which shift the paradigm of microcomb generation by greatly reducing the potential power consumption of these devices. In applications requiring a low power source with a tunable repetition rate, such as in portable combs for optical atomic clocks, the microresonator-filtered fibre laser scheme shows excellent potential to overcome the limitations of current state-of-the-art microcomb devices.

On top of this, the recent experimental results have revealed the critical role played by nonlocal thermal effects in the transition from noise to stable operation.

For future works, it will be crucial to examine in more detail the soliton's stability, especially to better understand the impact of the coexisting states which have been observed. It is worth noting that as yet, the microresonator-filtered fibre laser has always been entirely free-running, with no active feedback mechanisms of external locking to assist with stability. Such features are common, and essential, for modern lasers. Moving forwards,

the implementation of active feedback will be key for measurements where stability over a longer timescale is necessary.

Adjacent to this aim, a powerful technique that is recently being developed within the scope of lasers stability, control, and start-up is the application of machine-learning protocols [159, 231–237]. There has also been success in utilising machine-learning concepts to control highly nonlinear interactions to create intelligently customisable light sources - as demonstrated in "Customizing supercontinuum generation via on-chip adaptive temporal pulse-splitting." *Nature Communications* **9**, (2018) - a work that I contributed to during my PhD [238].

For practical, commercial laser systems, the turn-on procedure must be reliable and require minimal interference by the user. The implementation of machine-learning approaches to reliably control the start-up dynamics of these lasers in an automated way, is currently subject to intense research efforts, and the application of such a technique has not yet been applied to microcombs systems.

The laser cavity-solitons, presented in Chapter 2, generally address the major limitations of conventional microcomb devices from research groups around the world. Self-starting operation, agile tunability of the comb spacing, overcoming thermal instabilities and sufficient microcomb power of octave spanning self-referencing and stabilisation are the key challenges. As discussed in Chapter 1, recent works [118, 119] have experimentally demonstrated extremely low power self-injection locked microcomb lasers, which are capable of turn-key operation. Higher power combs would be required for optical atomic clock applications, and in this case, thermal instabilities tend to grow and destabilise the soliton state. To address this issue, the use of an auxiliary CW laser has been proposed [120], with promising results albeit increasing somewhat the complexity and footprint of the eventual device. Regarding the tunability of comb modes, coarse steps can be achieved by increasing the number of solitons in the cavity – doubling the repetition rate of the comb, but no solution provides an agile fine tuning of this parameter. The microresonator-filtered fibre laser provides this tunability through the free-space delay stage, which is a unique component to this device. The soliton solutions intrinsically have a much higher optical efficiency as discussed in Chapter 2. Thermal instabilities indeed remain present in these devices as evidenced by the works presented in Chapter 4, although further investigations into the stability of the soliton comb modes is essential (applying the same methodology as performed in Chapter 3 for Turing patterns in the same laser). The most recent experimental results, presented in Chapter 5, show clearly a direct pathway to soliton generation in the

laser by simply turning on the amplifier – although the underlying mechanisms that drive this evolution still require investigation. Once these few questions have been answered, we may begin to work at packaging such a device into a truly compact, portable optical frequency comb.

The successes brought about over these past 20 years by the optical frequency comb are innumerable. To take such devices outside of the laboratory environment, to everyday settings, will certainly be a truly ground-breaking development.

Bibliography

1. Bao, H. *et al.* Laser cavity-soliton microcombs. *Nature Photonics* **13,** 384–389 (2019) (cit. on pp. ii, 11, 16, 37, 39–43, 56, 57, 68).
2. Bao, H. *et al.* Turing patterns in a fiber laser with a nested microresonator: Robust and controllable microcomb generation. *Physical Review Research* **2,** 023395 (2020) (cit. on pp. ii, 17, 68).
3. Rowley, M. *et al.* Thermo-optical pulsing in a microresonator filtered fiber-laser: a route towards all-optical control and synchronization. *Optics Express* **27,** 19242–19253 (2019) (cit. on pp. ii, 17, 74).
4. Nicolis, G. & Prigogine, I. *Self-Organization in Nonequilibrium Systems: from Dissipative Structures to Order through Fluctuations* (Wiley-Blackwell, 1977) (cit. on p. 1).
5. Prigogine, I. Time, Structure, and Fluctuations. *Science* **201,** 777–785 (1978) (cit. on p. 1).
6. Hänsch, T. W. Nobel Lecture: Passion for precision. *Reviews of Modern Physics* **78,** 1297–1309 (2006) (cit. on pp. 1, 2).
7. Essen, L. & Parry, J. V. L. An Atomic Standard of Frequency and Time Interval: A Cæsium Resonator. *Nature* **176,** 280–282 (1955) (cit. on p. 1).
8. Diddams, S. A. *et al.* An Optical Clock Based on a Single Trapped $^{199}Hg^{+}$ Ion. *Science* **293,** 825–828 (2001) (cit. on p. 1).
9. Udem, T., Holzwarth, R. & Hänsch, T. W. Optical frequency metrology. *Nature* **416,** 233–237 (2002) (cit. on pp. 1, 2).
10. Bloom, B. J. *et al.* An optical lattice clock with accuracy and stability at the 10^{-18} level. *Nature* **506,** 71–75 (2014) (cit. on p. 1).
11. Ludlow, A. D., Boyd, M. M., Ye, J., Peik, E. & Schmidt, P. O. Optical atomic clocks. *Reviews of Modern Physics* **87,** 637–701 (2015) (cit. on pp. 1, 4).

12. Nicholson, T. *et al.* Systematic evaluation of an atomic clock at 2 x 10^{-18} total uncertainty. *Nature Communications* **6,** 1–8 (2015) (cit. on p. 1).

13. Marti, G. E. *et al.* Imaging Optical Frequencies with 100 μHz Precision and 1.1 μm Resolution. *Physical Review Letters* **120,** 103201 (2018) (cit. on p. 1).

14. McGrew, W. F. *et al.* Atomic clock performance enabling geodesy below the centimetre level. *Nature* **564,** 87–90 (2018) (cit. on p. 1).

15. Hall, J. L. Nobel Lecture: Defining and measuring optical frequencies. *Reviews of Modern Physics* **78,** 1279–1295 (2006) (cit. on p. 2).

16. Holzwarth, R. *et al.* Optical Frequency Synthesizer for Precision Spectroscopy. *Physical Review Letters* **85,** 2264–2267 (2000) (cit. on p. 2).

17. Jones, D. J. Carrier-Envelope Phase Control of Femtosecond Mode-Locked Lasers and Direct Optical Frequency Synthesis. *Science* **288,** 635–639 (2000) (cit. on p. 2).

18. Rosenband, T. *et al.* Frequency Ratio of Al^+ and Hg^+ Single-Ion Optical Clocks; Metrology at the 17th Decimal Place. *Science* **319,** 1808–1812 (2008) (cit. on p. 2).

19. Safronova, M. S. *et al.* Search for new physics with atoms and molecules. *Reviews of Modern Physics* **90,** 025008 (2018) (cit. on p. 2).

20. Fortier, T. M. *et al.* Generation of ultrastable microwaves via optical frequency division. *Nature Photonics* **5,** 425–429 (2011) (cit. on p. 2).

21. Quinlan, F. *et al.* Exploiting shot noise correlations in the photodetection of ultrashort optical pulse trains. *Nature Photonics* **7,** 290–293 (2013) (cit. on p. 2).

22. Coddington, I., Newbury, N. & Swann, W. Dual-comb spectroscopy. *Optica* **3,** 414–426 (2016) (cit. on p. 2).

23. Steinmetz, T. *et al.* Laser Frequency Combs for Astronomical Observations. *Science* **321,** 1335–1337 (2008) (cit. on p. 2).

24. Fischer, D. A. *et al.* State of the Field: Extreme Precision Radial Velocities. *Publications of the Astronomical Society of the Pacific* **128,** 066001 (2016) (cit. on p. 2).

25. McCracken, R. A., Charsley, J. M. & Reid, D. T. A decade of astrocombs: recent advances in frequency combs for astronomy [Invited]. *Optics Express* **25,** 15058–15078 (2017) (cit. on p. 2).

26. Fortier, T. & Baumann, E. 20 years of developments in optical frequency comb technology and applications. *Communications Physics* **2,** 1–16 (2019) (cit. on pp. 2–4, 15).

27. Hargrove, L. E., Fork, R. L. & Pollack, M. A. Locking of He-Ne Laser Modes induced by synchronous intracavity modulation. *Applied Physics Letters* **5,** 4–5 (1964) (cit. on p. 2).

28. Ippen, E., Shank, C. & Dienes, A. Passive mode locking of the cw dye laser. *Applied Physics Letters* **21,** 348–350 (1972) (cit. on p. 2).

29. Haus, H. Mode-locking of lasers. *IEEE Journal of Selected Topics in Quantum Electronics* **6,** 1173–1185 (2000) (cit. on p. 2).

30. Telle, H., Lipphardt, B. & Stenger, J. Kerr-lens, mode-locked lasers as transfer oscillators for optical frequency measurements. *Applied Physics B: Lasers and Optics* **74,** 1–6 (2002) (cit. on p. 2).

31. Paschotta, R., Schlatter, A., Zeller, S., Telle, H. & Keller, U. Optical phase noise and carrier-envelope offset noise of mode-locked lasers. *Applied Physics B* **82,** 265–273 (2006) (cit. on p. 2).

32. Udem, T. *PhD Thesis: Phasenkohärente optische Frequenzmessungen am Wasserstoffatom. Bestimmung der Rydberg–Konstanten und der 1S Lamb–Verschiebung* PhD thesis (Ludwig–Maximilians–Universität München, 1997) (cit. on p. 4).

33. Reichert, J., Holzwarth, R., Udem, T. & Hänsch, T. W. Measuring the frequency of light with mode-locked lasers. *Optics Communications* **172,** 59–68 (1999) (cit. on p. 4).

34. Telle, H. *et al.* Carrier-envelope offset phase control: A novel concept for absolute optical frequency measurement and ultrashort pulse generation. *Applied Physics B* **69,** 327–332 (1999) (cit. on p. 4).

35. Fortier, T. M., Bartels, A. & Diddams, S. A. Octave-spanning Ti:sapphire laser with a repetition rate $>$ 1 GHz for optical frequency measurements and comparisons. *Optics Letters* **31,** 1011–1013 (2006) (cit. on p. 4).

36. Bartels, A., Heinecke, D. & Diddams, S. A. 10-GHz Self-Referenced Optical Frequency Comb. *Science* **326,** 681–681 (2009) (cit. on p. 4).

37. Sinclair, L. C. *et al.* Invited Article: A compact optically coherent fiber frequency comb. *Review of Scientific Instruments* **86,** 081301 (2015) (cit. on pp. 4, 68).

38. Schibli, T. R. *et al.* Optical frequency comb with submillihertz linewidth and more than 10 W average power. *Nature Photonics* **2,** 355–359 (2008) (cit. on p. 4).

39. Nicolodi, D. *et al.* Spectral purity transfer between optical wavelengths at the 10^{-18} level. *Nature Photonics* **8,** 219–223 (2014) (cit. on p. 4).

40. Riehle, F. Towards a redefinition of the second based on optical atomic clocks. *Comptes Rendus Physique* **16,** 506–515 (2015) (cit. on p. 4).

41. Giunta, M. *et al.* 20 Years and 20 Decimal Digits: A Journey With Optical Frequency Combs. *IEEE Photonics Technology Letters* **31,** 1898–1901 (2019) (cit. on p. 4).

42. *EU Quantum Technology Flagship-Intermediate Report* (High-level Steering Committee, 2017) (cit. on p. 5).

43. Foster, M. A., Turner, A. C., Lipson, M. & Gaeta, A. L. Nonlinear optics in photonic nanowires. *Optics Express* **16,** 1300–1320 (2008) (cit. on p. 5).

44. Leuthold, J., Koos, C. & Freude, W. Nonlinear silicon photonics. *Nature Photonics* **4,** 535–544 (2010) (cit. on pp. 5, 53).

45. Moss, D. J., Morandotti, R., Gaeta, A. L. & Lipson, M. New CMOS-compatible platforms based on silicon nitride and Hydex for nonlinear optics. *Nature Photonics* **7,** 597–607 (2013) (cit. on pp. 5, 6, 43).

46. Yamamoto, Y. & Slusher, R. E. Optical Processes in Microcavities. *Physics Today* **46,** 66–73 (1993) (cit. on p. 5).

47. Little, B., Chu, S., Haus, H., Foresi, J. & Laine, J.-P. Microring resonator channel dropping filters. *Journal of Lightwave Technology* **15,** 998–1005 (1997) (cit. on p. 5).

48. Djordjev, K., Choi, S.-J., Choi, S.-J. & Dapkus, R. Microdisk tunable resonant filters and switches. *IEEE Photonics Technology Letters* **14,** 828–830 (2002) (cit. on p. 5).

49. Offrein, B. *et al.* Resonant coupler-based tunable add after-drop filter in silicon-oxynitride technology for WDM networks. *IEEE Journal of Selected Topics in Quantum Electronics* **5,** 1400–1406 (1999) (cit. on p. 5).

50. Vahala, K. J. Optical microcavities. *Nature* **424,** 839–846 (2003) (cit. on p. 5).

51. Little, B. *et al.* Very high-order microring resonator filters for WDM applications. *IEEE Photonics Technology Letters* **16,** 2263–2265 (2004) (cit. on p. 5).

52. Matsko, A. & Ilchenko, V. Optical resonators with whispering-gallery modes-part I: basics. *IEEE Journal of Selected Topics in Quantum Electronics* **12,** 3–14 (2006) (cit. on p. 5).

53. Pfeiffer, M. H. P. *et al.* Photonic Damascene process for integrated high-Q microresonator based nonlinear photonics. *Optica* **3,** 20–25 (2016) (cit. on p. 5).

54. Braginsky, V., Gorodetsky, M. & Ilchenko, V. Quality-factor and nonlinear properties of optical whispering-gallery modes. *Physics Letters A* **137,** 393–397 (1989) (cit. on p. 6).

55. Del'Haye, P., Diddams, S. A. & Papp, S. B. Laser-machined ultra-high-Q microrod resonators for nonlinear optics. *Applied Physics Letters* **102,** 221119 (2013) (cit. on pp. 6, 54).

56. Lee, H. *et al.* Chemically etched ultrahigh- Q wedge-resonator on a silicon chip. *Nature Photonics* **6,** 369–373 (2012) (cit. on p. 6).

57. Kippenberg, T. J., Holzwarth, R. & Diddams, S. A. Microresonator-based optical frequency combs. *Science* **332,** 555–559 (2011) (cit. on pp. 7, 18, 19, 36, 53).

58. Pasquazi, A. *et al.* Micro-combs: A novel generation of optical sources. *Physics Reports* **729,** 1–81 (2018) (cit. on pp. 7, 18–20, 29, 36, 53, 56, 57).

59. Agrawal, G. *Nonlinear Fiber Optics* (Elsevier, 2013) (cit. on p. 7).

60. Hendry, I. *et al.* Experimental observation of internally pumped parametric oscillation and quadratic comb generation in a $\chi^{(2)}$ whispering-gallery-mode microresonator. *Optics Letters* **45,** 1204–1207 (2020) (cit. on p. 7).

61. Szabados, J. *et al.* Frequency Comb Generation via Cascaded Second-Order Nonlinearities in Microresonators. *Physical Review Letters* **124,** 203902 (2020) (cit. on p. 7).

62. Kippenberg, T. J., Spillane, S. M. & Vahala, K. J. Kerr-Nonlinearity Optical Parametric Oscillation in an Ultrahigh- Q Toroid Microcavity. *Physical Review Letters* **93,** 083904 (2004) (cit. on pp. 7, 53).

63. Savchenkov, A. A. *et al.* Low Threshold Optical Oscillations in a Whispering Gallery Mode CaF_2 Resonator. *Physical Review Letters* **93,** 243905 (2004) (cit. on pp. 7, 53).

64. Chembo, Y. K., Strekalov, D. V. & Yu, N. Spectrum and Dynamics of Optical Frequency Combs Generated with Monolithic Whispering Gallery Mode Resonators. *Physical Review Letters* **104,** 103902 (2010) (cit. on p. 7).

65. Matsko, A. B. *et al.* Mode-locked Kerr frequency combs. *Optics Letters* **36,** 2845–2847 (2011) (cit. on p. 7).

66. Ferdous, F. *et al.* Spectral line-by-line pulse shaping of on-chip microresonator frequency combs. *Nature Photonics* **5,** 770–776 (2011) (cit. on p. 7).

67. Herr, T. *et al.* Universal formation dynamics and noise of Kerr-frequency combs in microresonators. *Nature Photonics* **6,** 480–487 (2012) (cit. on p. 7).

68. Turing, A. M. The chemical basis of morphogenesis. *Philosophical Transactions of the Royal Society of London. Series B, Biological Sciences* **237,** 37–72 (1952) (cit. on pp. 7, 36).

69. Ikeda, K. Multiple-valued stationary state and its instability of the transmitted light by a ring cavity system. *Optics Communications* **30,** 257–261 (1979) (cit. on p. 7).

70. Ikeda, K., Daido, H. & Akimoto, O. Optical Turbulence: Chaotic Behavior of Transmitted Light from a Ring Cavity. *Physical Review Letters* **45,** 709–712 (1980) (cit. on p. 7).

71. McLaughlin, D. W., Moloney, J. V. & Newell, A. C. New Class of Instabilities in Passive Optical Cavities. *Physical Review Letters* **54,** 681–684 (1985) (cit. on pp. 7, 9).

72. Adachihara, H., McLaughlin, D. W., Moloney, J. V. & Newell, A. C. Solitary waves as fixed points of infinite-dimensional maps for an optical bistable ring cavity: Analysis. *Journal of Mathematical Physics* **29,** 63–85 (1988) (cit. on p. 7).

73. Lugiato, L. A. & Lefever, R. Spatial Dissipative Structures in Passive Optical Systems. *Physical Review Letters* **58,** 2209–2211 (1987) (cit. on pp. 7, 8, 36).

74. Haelterman, M., Trillo, S. & Wabnitz, S. Dissipative modulation instability in a nonlinear dispersive ring cavity. *Optics Communications* **91,** 401–407 (1992) (cit. on pp. 7, 8, 18–20, 36).

75. Scroggie, A. *et al.* Pattern formation in a passive Kerr cavity. *Chaos, Solitons & Fractals* **4,** 1323–1354 (1994) (cit. on pp. 8, 36).

76. Lugiato, L. A., Prati, F., Gorodetsky, M. L. & Kippenberg, T. J. From the Lugiato–Lefever equation to microresonator-based soliton Kerr frequency combs. *Philosophical Transactions of the Royal Society A: Mathematical, Physical and Engineering Sciences* **376,** 20180113 (2018) (cit. on pp. 8, 36).

77. Pampaloni, E., Residori, S. & Arecchi, F. T. Roll-Hexagon Transition in a Kerr-Like Experiment. *Europhysics Letters (EPL)* **24,** 647–652 (1993) (cit. on p. 8).

78. Arecchi, F. T. Optical morphogenesis: pattern formation and competition in nonlinear optics. *Physica D: Nonlinear Phenomena* **86,** 297–322 (1995) (cit. on p. 8).

79. Taranenko, V. B., Ganne, I., Kuszelewicz, R. J. & Weiss, C. O. Patterns and localized structures in bistable semiconductor resonators. *Physical Review A* **61,** 063818 (2000) (cit. on p. 8).

80. Coen, S. & Haelterman, M. Modulational Instability Induced by Cavity Boundary Conditions in a Normally Dispersive Optical Fiber. *Physical Review Letters* **79,** 4139–4142 (1997) (cit. on p. 8).

81. Herr, T. *et al.* Temporal solitons in optical microresonators. *Nature Photonics* **8,** 145–152 (2014) (cit. on pp. 8, 10–12, 18, 19, 53).

82. Coillet, A. *et al.* Azimuthal Turing Patterns, Bright and Dark Cavity Solitons in Kerr Combs Generated With Whispering-Gallery-Mode Resonators. *IEEE Photonics Journal* **5,** 6100409 (2013) (cit. on pp. 8, 36).

83. Coillet, A. & Chembo, Y. On the robustness of phase locking in Kerr optical frequency combs. *Optics Letters* **39,** 1529–1532 (2014) (cit. on pp. 8, 36, 47).

84. Lugiato, L. Introduction to the feature section on cavity solitons: An overview. *IEEE Journal of Quantum Electronics* **39,** 193–196 (2003) (cit. on p. 9).

85. Grelu, P. & Akhmediev, N. Dissipative solitons for mode-locked lasers. *Nature Photonics* **6,** 84–92 (2012) (cit. on pp. 9, 19, 68).

86. Firth, W. J. & Harkness, G. K. Cavity Solitons. *Asian Journal of Physics* **7,** 1–13 (1998) (cit. on p. 9).

87. McDonald, G. S. & Firth, W. J. Spatial solitary-wave optical memory. *Journal of the Optical Society of America B* **7,** 1328–1335 (1990) (cit. on p. 9).

88. Rosanov, N. N. in *Progress in Optics* (ed Wolf, E.) 1–60 (Elsevier, 1996) (cit. on p. 9).

89. Firth, W. Buffering optical data. *Nature Photonics* **4,** 415–417 (2010) (cit. on p. 9).

90. Marconi, M., Javaloyes, J., Balle, S. & Giudici, M. How Lasing Localized Structures Evolve out of Passive Mode Locking. *Physical Review Letters* **112,** 223901 (2014) (cit. on pp. 9, 14, 18, 19, 36, 40, 68, 69).

91. Leo, F. *et al.* Temporal cavity solitons in one-dimensional Kerr media as bits in an all-optical buffer. *Nature Photonics* **4,** 471–476 (2010) (cit. on pp. 9, 18, 19, 36, 53, 69).

92. Jang, J. K., Erkintalo, M., Murdoch, S. G. & Coen, S. Ultraweak long-range interactions of solitons observed over astronomical distances. *Nature Photonics* **7,** 657–663 (2013) (cit. on p. 9).

93. Leo, F., Gelens, L., Emplit, P., Haelterman, M. & Coen, S. Dynamics of one-dimensional Kerr cavity solitons. *Optics Express* **21,** 9180–9191 (2013) (cit. on p. 9).

94. Jang, J. K., Erkintalo, M., Murdoch, S. G. & Coen, S. Observation of dispersive wave emission by temporal cavity solitons. *Optics Letters* **39,** 5503–5506 (2014) (cit. on p. 9).

95. Jang, J. K., Erkintalo, M., Murdoch, S. G. & Coen, S. Writing and erasing of temporal cavity solitons by direct phase modulation of the cavity driving field. *Optics Letters* **40,** 4755–4758 (2015) (cit. on p. 9).

96. Luo, K., Jang, J. K., Coen, S., Murdoch, S. G. & Erkintalo, M. Spontaneous creation and annihilation of temporal cavity solitons in a coherently driven passive fiber resonator. *Optics Letters* **40,** 3735–3738 (2015) (cit. on p. 9).

97. Anderson, M., Leo, F., Coen, S., Erkintalo, M. & Murdoch, S. G. Observations of spatiotemporal instabilities of temporal cavity solitons. *Optica* **3,** 1071–1074 (2016) (cit. on p. 9).

98. Jang, J. K. *et al.* All-optical buffer based on temporal cavity solitons operating at 10 Gb/s. *Optics Letters* **41,** 4526–4529 (2016) (cit. on p. 9).

99. Del'Haye, P. *et al.* Optical frequency comb generation from a monolithic microresonator. *Nature* **450,** 1214–1217 (2007) (cit. on pp. 10, 44, 47, 53).

100. Yi, X., Yang, Q.-F., Yang, K. Y., Suh, M.-G. & Vahala, K. Soliton frequency comb at microwave rates in a high-Q silica microresonator. *Optica* **2,** 1078–1085 (2015) (cit. on p. 10).

101. Yi, X., Yang, Q.-F., Youl Yang, K. & Vahala, K. Active capture and stabilization of temporal solitons in microresonators. *Optics Letters* **41,** 2037 (2016) (cit. on p. 10).

102. Brasch, V. *et al.* Photonic chip–based optical frequency comb using soliton Cherenkov radiation. *Science* **351,** 357–360 (2016) (cit. on pp. 10, 18, 19, 36, 53, 68).

103. Joshi, C. *et al.* Thermally controlled comb generation and soliton modelocking in microresonators. *Optics Letters* **41,** 2565–2568 (2016) (cit. on p. 10).

104. Webb, K. E., Erkintalo, M., Coen, S. & Murdoch, S. G. Experimental observation of coherent cavity soliton frequency combs in silica microspheres. *Optics Letters* **41,** 4613–4616 (2016) (cit. on p. 10).

105. Obrzud, E., Lecomte, S. & Herr, T. Temporal solitons in microresonators driven by optical pulses. *Nature Photonics* **11,** 600–607 (2017) (cit. on pp. 11, 19, 36, 68).

106. Xue, X., Zheng, X. & Zhou, B. Super-efficient temporal solitons in mutually coupled optical cavities. *Nature Photonics* **13,** 616–622 (2019) (cit. on p. 11).

107. Stern, B., Ji, X., Okawachi, Y., Gaeta, A. L. & Lipson, M. Battery-operated integrated frequency comb generator. *Nature* **562,** 401–408 (2018) (cit. on pp. 11, 13, 19, 31, 36, 53, 68).

108. Raja, A. S. *et al.* Electrically pumped photonic integrated soliton microcomb. *Nature Communications* **10,** 1–8 (2019) (cit. on pp. 11, 13, 53).

109. Pfeiffer, M. H. P. *et al.* Octave-spanning dissipative Kerr soliton frequency combs in Si_3N_4 microresonators. *Optica* **4,** 684–691 (2017) (cit. on p. 11).

110. Chembo, Y. K. & Menyuk, C. R. Spatiotemporal Lugiato-Lefever formalism for Kerr-comb generation in whispering-gallery-mode resonators. *Physical Review A* **87,** 053852 (2013) (cit. on pp. 11, 39).

111. Godey, C., Balakireva, I. V., Coillet, A. & Chembo, Y. K. Stability analysis of the spatiotemporal Lugiato-Lefever model for Kerr optical frequency combs in the anomalous and normal dispersion regimes. *Physical Review A* **89,** 063814 (2014) (cit. on pp. 11, 36, 56).

112. Coen, S., Randle, H. G., Sylvestre, T. & Erkintalo, M. Modeling of octave-spanning Kerr frequency combs using a generalized mean-field Lugiato-Lefever model. *Optics Letters* **38,** 37–39 (2013) (cit. on pp. 11, 36).

113. Ilchenko, V. & Gorodetsky, M. Thermal nonlinear effects in optical whispering gallery microresonators. *Laser Physics* **2,** 1004–1009 (1992) (cit. on pp. 12, 53, 57).

114. Matsko, A. B., Savchenkov, A. A., Yu, N. & Maleki, L. Whispering-gallery-mode resonators as frequency references I Fundamental limitations. *Journal of the Optical Society of America B* **24,** 1324–1335 (2007) (cit. on p. 12).

115. Savchenkov, A. A., Matsko, A. B., Ilchenko, V. S., Yu, N. & Maleki, L. Whispering-gallery-mode resonators as frequency references II Stabilization. *Journal of the Optical Society of America B* **24,** 2988–2997 (2007) (cit. on p. 12).

116. Carmon, T., Yang, L. & Vahala, K. J. Dynamical thermal behavior and thermal selfstability of microcavities. *Optics Express* **12,** 4742–4750 (2004) (cit. on p. 12).

117. Xue, X., Wang, P.-H., Xuan, Y., Qi, M. & Weiner, A. M. Microresonator Kerr frequency combs with high conversion efficiency: High-efficiency microcombs. *Laser & Photonics Reviews* **11,** 1600276 (2017) (cit. on pp. 12, 18, 19, 25, 31).

118. He, Y. *et al.* Self-starting bi-chromatic $LiNbO_3$ soliton microcomb. *Optica* **6,** 1138–1144 (2019) (cit. on pp. 13, 68, 69, 83).

119. Shen, B. *et al.* Integrated turnkey soliton microcombs. *Nature* **582,** 365–369 (2020) (cit. on pp. 13, 69, 83).

120. Zhang, S. *et al.* Sub-milliwatt-level microresonator solitons with extended access range using an auxiliary laser. *Optica* **6,** 206–212 (2019) (cit. on pp. 13, 36, 68, 83).

121. Genevet, P., Barland, S., Giudici, M. & Tredicce, J. R. Cavity Soliton Laser Based on Mutually Coupled Semiconductor Microresonators. *Physical Review Letters* **101,** 123905 (2008) (cit. on pp. 13, 14, 18, 19, 68).

122. Tanguy, Y., Ackemann, T., Firth, W. J. & Jäger, R. Realization of a Semiconductor-Based Cavity Soliton Laser. *Physical Review Letters* **100,** 013907 (2008) (cit. on pp. 13, 14, 18–20, 68).

123. Rosanov, N. N. & Fedorov, S. V. Diffraction switching waves and autosolitons in a saturable-absorber laser. *Optics and Spectroscopy* **72,** 782–785 (1992) (cit. on p. 13).

124. Grigoryan, V. S. & Muradyan, T. S. Evolution of light pulses into autosolitons in nonlinear amplifying media. *Journal of the Optical Society of America B* **8,** 1757–1765 (1991) (cit. on p. 14).

125. Yang, L. & Vahala, K. J. Gain functionalization of silica microresonators. *Optics Letters* **28,** 592–594 (2003) (cit. on pp. 14, 53).

126. He, L., Özdemir, Ş. K. & Yang, L. Whispering gallery microcavity lasers: WGM microlasers. *Laser & Photonics Reviews* **7,** 60–82 (2013) (cit. on pp. 14, 53).

127. Peccianti, M. *et al.* Demonstration of a stable ultrafast laser based on a nonlinear microcavity. *Nature Communications* **3** (2012) (cit. on pp. 14, 20, 29, 30, 37, 43, 53, 69).

128. Malomed, B. A. Solitary pulses in linearly coupled Ginzburg-Landau equations. *Chaos: An Interdisciplinary Journal of Nonlinear Science* **17,** 037117 (2007) (cit. on pp. 15, 40).

129. Faist, J. *et al.* Quantum Cascade Laser Frequency Combs. *Nanophotonics* **5,** 272–291 (2016) (cit. on p. 15).

130. Prati, F. *et al.* Soliton dynamics of ring quantum cascade lasers with injected signal. *Nanophotonics* **10,** 195–207 (2020) (cit. on p. 15).

131. Carlson, D. R. *et al.* Ultrafast electro-optic light with subcycle control. *Science* **361,** 1358–1363 (2018) (cit. on p. 15).

132. Suh, M.-G., Yang, Q.-F., Yang, K. Y., Yi, X. & Vahala, K. J. Microresonator soliton dual-comb spectroscopy. *Science* **354,** 600–603 (2016) (cit. on pp. 18, 19, 36, 68).

133. Yu, M. *et al.* Silicon-chip-based mid-infrared dual-comb spectroscopy. *Nature Communications* **9,** 1–6 (2018) (cit. on pp. 18, 19, 36).

134. Marin-Palomo, P. *et al.* Microresonator-based solitons for massively parallel coherent optical communications. *Nature* **546,** 274–279 (2017) (cit. on pp. 18, 19, 36, 68).

135. Pfeifle, J. *et al.* Optimally Coherent Kerr Combs Generated with Crystalline Whispering Gallery Mode Resonators for Ultrahigh Capacity Fiber Communications. *Physical Review Letters* **114,** 093902 (2015) (cit. on pp. 18, 19, 36).

136. Liang, W. *et al.* High spectral purity Kerr frequency comb radio frequency photonic oscillator. *Nature Communications* **6,** 7957 (2015) (cit. on pp. 18, 19, 36, 68, 69).

137. Spencer, D. T. *et al.* An optical-frequency synthesizer using integrated photonics. *Nature* **557,** 81–88 (2018) (cit. on pp. 18, 19, 36, 68).

138. Trocha, P. *et al.* Ultrafast optical ranging using microresonator soliton frequency combs. *Science* **359,** 887–891 (2018) (cit. on pp. 18, 19, 25).

139. Suh, M.-G. & Vahala, K. J. Soliton microcomb range measurement. *Science* **359,** 884–887 (2018) (cit. on pp. 18, 19, 36, 68).

140. Kues, M. *et al.* On-chip generation of high-dimensional entangled quantum states and their coherent control. *Nature* **546,** 622–626 (2017) (cit. on pp. 18, 19).

141. Reimer, C. *et al.* Generation of multiphoton entangled quantum states by means of integrated frequency combs. *Science* **351,** 1176–1180 (2016) (cit. on pp. 18, 19, 53).

142. Del'Haye, P. *et al.* Phase-coherent microwave-to-optical link with a self-referenced microcomb. *Nature Photonics* **10,** 516–520 (2016) (cit. on pp. 18, 19).

143. Suh, M.-G. *et al.* Searching for exoplanets using a microresonator astrocomb. *Nature Photonics* **13,** 25–31 (2019) (cit. on pp. 18, 19).

144. Obrzud, E. *et al.* A microphotonic astrocomb. *Nature Photonics* **13,** 31–35 (2019) (cit. on pp. 18, 19).

145. Xue, X. *et al.* Mode-locked dark pulse Kerr combs in normal-dispersion microresonators. *Nature Photonics* **9,** 594–600 (2015) (cit. on pp. 18, 19, 25).

146. Cole, D. C., Lamb, E. S., Del'Haye, P., Diddams, S. A. & Papp, S. B. Soliton crystals in Kerr resonators. *Nature Photonics* **11,** 671–676 (2017) (cit. on pp. 18, 19).

147. Lugiato, L., Prati, F. & Brambilla, M. *Nonlinear Optical Systems* (Cambridge University Press, 2015) (cit. on pp. 18, 19, 27, 29, 36, 41, 63, 68).

148. Yao, B. *et al.* Gate-tunable frequency combs in graphene–nitride microresonators. *Nature* **558,** 410–419 (2018) (cit. on pp. 18, 19).

149. Barland, S. *et al.* Cavity solitons as pixels in semiconductor microcavities. *Nature* **419,** 699–702 (2002) (cit. on pp. 18, 19, 68).

150. Wright, L. G., Christodoulides, D. N. & Wise, F. W. Spatiotemporal mode-locking in multimode fiber lasers. *Science* **358,** 94–97 (2017) (cit. on pp. 18, 20, 22).

151. Yang, Q.-F., Yi, X., Yang, K. Y. & Vahala, K. Counter-propagating solitons in microresonators. *Nature Photonics* **11,** 560–564 (2017) (cit. on p. 19).

152. Miller, S. A. *et al.* Tunable frequency combs based on dual microring resonators. *Optics Express* **23,** 21527–21540 (2015) (cit. on p. 19).

153. Gustave, F. *et al.* Observation of Mode-Locked Spatial Laser Solitons. *Physical Review Letters* **118,** 044102 (2017) (cit. on pp. 19, 68).

154. Krupa, K. *et al.* Spatial beam self-cleaning in multimode fibres. *Nature Photonics* **11,** 237–241 (2017) (cit. on p. 20).

155. Scroggie, A. J., Firth, W. J. & Oppo, G.-L. Cavity-soliton laser with frequency-selective feedback. *Physical Review A* **80,** 013829 (2009) (cit. on pp. 20, 40).

156. Wang, W. *et al.* Repetition Rate Multiplication Pulsed Laser Source Based on a Microring Resonator. *ACS Photonics* **4,** 1677–1683 (2017) (cit. on pp. 20, 29, 30, 37, 42, 43).

157. Del'Haye, P., Arcizet, O., Gorodetsky, M. L., Holzwarth, R. & Kippenberg, T. J. Frequency comb assisted diode laser spectroscopy for measurement of microcavity dispersion. *Nature Photonics* **3,** 529–533 (2009) (cit. on pp. 24, 43).

158. Bao, H. *et al.* Type-II micro-comb generation in a filter-driven four wave mixing laser [Invited]. *Photonics Research* **6,** B67–B73 (2018) (cit. on pp. 29, 30, 37, 42, 43).

159. Andral, U. & Grelu, P. Fiber laser mode locked through an evolutionary algorithm. *Optica* **2,** 275–278 (2015) (cit. on pp. 33, 83).

160. Staliūnas, K. & Sánchez-Morcillo, V. J. *Transverse Patterns in Nonlinear Optical Resonators* red. by Höhler, G. *et al.* (Springer Berlin Heidelberg, 2003) (cit. on p. 36).

161. Ackemann, T., Logvin, Y. A., Heuer, A. & Lange, W. Transition between Positive and Negative Hexagons in Optical Pattern Formation. *Physical Review Letters* **75,** 3450–3453 (1995) (cit. on p. 36).

162. D'Alessandro, G., Pampaloni, E., Ramazza, P.-L., Residori, S. & Arecchi, F. T. Amplitude equations and pattern formation in a liquid-crystal light-valve experiment. *Physical Review A* **52,** 4176–4181 (1995) (cit. on p. 36).

163. Oppo, G.-L., Brambilla, M. & Lugiato, L. A. Formation and evolution of roll patterns in optical parametric oscillators. *Physical Review A* **49,** 2028–2032 (1994) (cit. on p. 36).

164. Perego, A. M., Tarasov, N., Churkin, D. V., Turitsyn, S. K. & Staliunas, K. Pattern Generation by Dissipative Parametric Instability. *Physical Review Letters* **116,** 028701 (2016) (cit. on p. 36).

165. Anderson, M. *et al.* Coexistence of Multiple Nonlinear States in a Tristable Passive Kerr Resonator. *Physical Review X* **7,** 031031 (2017) (cit. on pp. 36, 77, 78).

166. Nielsen, A. U., Garbin, B., Coen, S., Murdoch, S. G. & Erkintalo, M. Coexistence and Interactions between Nonlinear States with Different Polarizations in a Monochromatically Driven Passive Kerr Resonator. *Physical Review Letters* **123,** 013902 (2019) (cit. on p. 36).

167. Savchenkov, A. A., Matsko, A. B. & Maleki, L. On Frequency Combs in Monolithic Resonators. *Nanophotonics* **5,** 363–391 (2016) (cit. on p. 36).

168. Grelu, P. *Nonlinear Optical Cavity Dynamics: From Microresonators to Fiber Lasers* (Wiley-VCH, 2016) (cit. on pp. 36, 43, 69, 77).

169. Kippenberg, T. J., Gaeta, A. L., Lipson, M. & Gorodetsky, M. L. Dissipative Kerr solitons in optical microresonators. *Science* **361,** eaan8083 (2018) (cit. on p. 36).

170. Gaeta, A. L., Lipson, M. & Kippenberg, T. J. Photonic-chip-based frequency combs. *Nature Photonics* **13,** 158–169 (2019) (cit. on p. 36).

171. Liang, W. *et al.* Miniature multioctave light source based on a monolithic microcavity. *Optica* **2,** 40–47 (2015) (cit. on p. 36).

172. Maleki, L., Ilchenko, V. S. & Matsko, A. B. *Practical Applications of Microresonators in Optics and Photonics* (CRC press, 2018) (cit. on p. 36).

173. Huang, S.-W. *et al.* A broadband chip-scale optical frequency synthesizer at 2.7 x 10^{-16} relative uncertainty. *Science Advances* **2,** e1501489 (2016) (cit. on pp. 36, 68).

174. Dutt, A. *et al.* On-chip dual-comb source for spectroscopy. *Science Advances* **4,** e1701858 (2018) (cit. on p. 36).

175. Huang, S.-W. *et al.* Globally Stable Microresonator Turing Pattern Formation for Coherent High-Power THz Radiation On-Chip. *Physical Review X* **7,** 041002 (2017) (cit. on pp. 36, 37, 44, 47, 50).

176. Diallo, S. & Chembo, Y. K. Optimization of primary Kerr optical frequency combs for tunable microwave generation. *Optics Letters* **42,** 3522–3525 (2017) (cit. on p. 36).

177. Coulibaly, S. *et al.* Turbulence-Induced Rogue Waves in Kerr Resonators. *Physical Review X* **9,** 011054 (2019) (cit. on p. 37).

178. Pasquazi, A. *et al.* Stable, dual mode, high repetition rate mode-locked laser based on a microring resonator. *Optics Express* **20,** 27355–27363 (2012) (cit. on pp. 37, 43).

179. Haus, H. A. & Huang, W. Coupled-mode theory. *Proceedings of the IEEE* **79,** 1505–1518 (1991) (cit. on p. 40).

180. Atai, J. & Malomed, B. A. Stability and interactions of solitons in two-component active systems. *Physical Review E* **54,** 4371–4374 (1996) (cit. on p. 40).

181. Sigler, A., Malomed, B. A. & Skryabin, D. V. Localized states in a triangular set of linearly coupled complex Ginzburg-Landau equations. *Physical Review E* **74,** 066604 (2006) (cit. on p. 40).

182. Haboucha, A., Leblond, H., Salhi, M., Komarov, A. & Sanchez, F. Analysis of soliton pattern formation in passively mode-locked fiber lasers. *Physical Review A* **78,** 043806 (2008) (cit. on p. 40).

183. Si Fodil, R., Amrani, F., Yang, C., Kellou, A. & Grelu, P. Adjustable high-repetition-rate pulse trains in a passively-mode-locked fiber laser. *Physical Review A* **94,** 013813 (2016) (cit. on p. 42).

184. Tarasov, N., Perego, A. M., Churkin, D. V., Staliunas, K. & Turitsyn, S. K. Mode-locking via dissipative Faraday instability. *Nature Communications* **7** (2016) (cit. on p. 43).

185. Copie, F., Conforti, M., Kudlinski, A., Mussot, A. & Trillo, S. Competing Turing and Faraday Instabilities in Longitudinally Modulated Passive Resonators. *Physical Review Letters* **116,** 143901 (2016) (cit. on p. 43).

186. Udem, T., Reichert, J., Holzwarth, R. & Hänsch, T. W. Accurate measurement of large optical frequency differences with a mode-locked laser. *Optics Letters* **24,** 881–883 (1999) (cit. on pp. 44, 47).

187. Zhang, S. *et al.* Terahertz wave generation using a soliton microcomb. *Optics Express* **27,** 35257–35266 (2019) (cit. on p. 49).

188. Weng, W. *et al.* Spectral Purification of Microwave Signals with Disciplined Dissipative Kerr Solitons. *Physical Review Letters* **122,** 013902 (2019) (cit. on p. 49).

189. Chembo, Y. K. Kerr optical frequency combs: theory, applications and perspectives. *Nanophotonics* **5,** 214–230 (2016) (cit. on p. 53).

190. Haelterman, M., Trillo, S. & Wabnitz, S. Polarization multistability and instability in a nonlinear dispersive ring cavity. *Journal of the Optical Society of America B* **11,** 446–456 (1994) (cit. on p. 53).

191. Pavlov, N. G. *et al.* Narrow-linewidth lasing and soliton Kerr microcombs with ordinary laser diodes. *Nature Photonics* **12,** 694–699 (2018) (cit. on pp. 53, 68, 69).

192. Galiev, R. R. *et al.* Spectrum collapse, narrow linewidth, and Bogatov effect in diode lasers locked to high-Q optical microresonators. *Optics Express* **26,** 30509–30522 (2018) (cit. on p. 53).

193. Kues, M. *et al.* Passively mode-locked laser with an ultra-narrow spectral width. *Nature Photonics* **11,** 159–162 (2017) (cit. on p. 53).

194. Boyd, R. W. *Nonlinear Optics* (Academic Press, 2003) (cit. on p. 53).

195. Kippenberg, T. J., Rokhsari, H., Carmon, T., Scherer, A. & Vahala, K. J. Analysis of Radiation-Pressure Induced Mechanical Oscillation of an Optical Microcavity. *Physical Review Letters* **95,** 033901 (2005) (cit. on p. 53).

196. Monifi, F. *et al.* Optomechanically induced stochastic resonance and chaos transfer between optical fields. *Nature Photonics* **10,** 399–405 (2016) (cit. on p. 53).

197. Diallo, S., Lin, G. & Chembo, Y. K. Giant thermo-optical relaxation oscillations in millimeter-size whispering gallery mode disk resonators. *Optics Letters* **40,** 3834 (2015) (cit. on p. 53).

198. Deng, Y., Liu, F., Leseman, Z. C. & Hossein-Zadeh, M. Thermo-optomechanical oscillator for sensing applications. *Optics Letters* **21,** 4653–4664 (2013) (cit. on p. 53).

199. Park, Y.-S. & Wang, H. Regenerative pulsation in silica microspheres. *Optics Letters* **32,** 3104–3106 (2007) (cit. on p. 53).

200. Luo, Z.-C., Ma, C.-Y., Li, B.-B. & Xiao, Y.-F. MHz-level self-sustained pulsation in polymer microspheres on a chip. *AIP Advances* **4,** 122902 (2014) (cit. on p. 53).

201. He, L., Özdemir, Ş. K., Zhu, J. & Yang, L. Self-pulsation in fiber-coupled, on-chip microcavity lasers. *Optics Letters* **35,** 256–258 (2010) (cit. on pp. 53, 56).

202. Baker, C. *et al.* Optical instability and self-pulsing in silicon nitride whispering gallery resonators. *Optics Express* **20,** 29076–29089 (2012) (cit. on pp. 53, 56).

203. Di Lauro, L. *et al.* Parametric control of thermal self-pulsation in micro-cavities. *Optics Letters* **42,** 3407–3410 (2017) (cit. on p. 53).

204. Ikeda, K. & Akimoto, O. Instability Leading to Periodic and Chaotic Self-Pulsations in a Bistable Optical Cavity. *Physical Review Letters* **48,** 617–620 (1982) (cit. on pp. 54, 56).

205. Haus, H. A. *Waves And Fields In Optoelectronics* (Prentice-Hall, 1984) (cit. on p. 56).

206. Van Tartwijk, G. H. & Agrawal, G. P. Laser instabilities: a modern perspective. *Progress in Quantum Electronics* **22,** 43–122 (1998) (cit. on pp. 56–58).

207. Moloney, J. V. & Newell, A. C. *Nonlinear Optics* (Westview Press, 2004) (cit. on p. 56).

208. Davidovich, L. Sub-Poissonian processes in quantum optics. *Reviews of Modern Physics* **68,** 127–173 (1996) (cit. on pp. 56, 57).

209. Weber, M. J. *Handbook of optical materials* (CRC Press, 2003) (cit. on p. 57).

210. Del'Haye, P., Papp, S. B. & Diddams, S. A. Hybrid Electro-Optically Modulated Microcombs. *Physical Review Letters* **109,** 263901 (2012) (cit. on p. 58).

211. Del'Haye, P. *PhD Thesis: Optical Frequency Comb Generation in Monolithic Microresonators* PhD thesis (Ludwig–Maximilians–Universität München, 2011) (cit. on p. 60).

212. Steinmeyer, G. Frontiers in Ultrashort Pulse Generation: Pushing the Limits in Linear and Nonlinear Optics. *Science* **286,** 1507–1512 (1999) (cit. on p. 68).

213. Li, Q. *et al.* Stably accessing octave-spanning microresonator frequency combs in the soliton regime. *Optica* **4,** 193–203 (2017) (cit. on p. 68).

214. Barland, S. *et al.* Temporal localized structures in optical resonators. *Advances in Physics: X* **2,** 496–517 (2017) (cit. on pp. 68, 69).

215. Qi, Z. *et al.* Dissipative cnoidal waves (Turing rolls) and the soliton limit in microring resonators. *Optica* **6,** 1220–1232 (2019) (cit. on pp. 68, 69).

216. Huang, Y. *et al.* Temporal soliton and optical frequency comb generation in a Brillouin laser cavity. *Optica* **6,** 1491–1497 (2019) (cit. on p. 69).

217. Voloshin, A. S. *et al.* Dynamics of soliton self-injection locking in a photonic chip-based microresonator. *arXiv:1912.11303.* arXiv: 1912.11303 (2020) (cit. on p. 69).

218. Wilmart, Q. *et al.* A Versatile Silicon-Silicon Nitride Photonics Platform for Enhanced Functionalities and Applications. *Applied Sciences* **9,** 1–16 (2019) (cit. on p. 74).

219. Thirstrup, C., Shi, Y. & Palsdottir, B. Pump-Induced Refractive Index and Dispersions in Er^{3+} -Doped fibers. *Journal of Lightwave Technology* **14,** 732–738 (1996) (cit. on pp. 75, 76).

220. Janos, M. & Guy, S. Signal-induced refractive index changes in erbium-doped fiber amplifiers. *Journal of Lightwave Technology* **16,** 542–548 (1998) (cit. on pp. 75–78).

221. Barmenkov, Y. O., Kir'yanov, A. V. & Andrés, M. V. Resonant and thermal changes of refractive index in a heavily doped erbium fiber pumped at wavelength 980nm. *Applied Physics Letters* **85,** 2466–2468 (2004) (cit. on pp. 75–78).

222. Davis, M., Digonnet, M. & Pantell, R. Thermal effects in doped fibers. *Journal of Lightwave Technology* **16,** 1013–1023 (1998) (cit. on pp. 75, 76).

223. Tang, D. Y., Zhao, L. M., Xie, G. Q. & Qian, L. J. Coexistence and competition between different soliton-shaping mechanisms in a laser. *Physical Review A* **75,** 063810 (2007) (cit. on p. 78).

224. Herink, G., Jalali, B., Ropers, C. & Solli, D. R. Resolving the build-up of femtosecond mode-locking with single-shot spectroscopy at 90 MHz frame rate. *Nature Photonics* **10,** 321–326 (2016) (cit. on p. 78).

225. Herink, G., Kurtz, F., Jalali, B., Solli, D. R. & Ropers, C. Real-time spectral interferometry probes the internal dynamics of femtosecond soliton molecules. *Science* **356,** 50–54 (2017) (cit. on p. 78).

226. Peng, J. *et al.* Real-time observation of dissipative soliton formation in nonlinear polarization rotation mode-locked fibre lasers. *Communications Physics* **1,** 1–8 (2018) (cit. on p. 78).

227. Liu, X. & Cui, Y. Revealing the behavior of soliton buildup in a mode-locked laser. *Advanced Photonics* **1,** 016003 (2019) (cit. on p. 78).

228. Lapre, C. *et al.* Real-time characterization of spectral instabilities in a mode-locked fibre laser exhibiting soliton-similariton dynamics. *Scientific Reports* **9,** 13950 (2019) (cit. on p. 78).

229. Peng, J., Boscolo, S., Zhao, Z. & Zeng, H. Breathing dissipative solitons in mode-locked fiber lasers. *Science Advances* **5,** eaax1110 (2019) (cit. on p. 78).

230. Goda, K. & Jalali, B. Dispersive Fourier transformation for fast continuous single-shot measurements. *Nature Photonics* **7,** 102–112 (2013) (cit. on p. 79).

231. Fu, X. Classification of birefringence in mode-locked fiber lasers using machine learning and sparse representation. *Optics Express* **22,** 8585–8597 (2014) (cit. on p. 83).

232. Kutz, J. N. Machine Learning for Self-Tuning Optical Systems. *Proceedings of the World Congress on Engineering* **1** (2015) (cit. on p. 83).

233. Woodward, R. I. & Kelleher, E. J. R. Towards 'smart lasers': self-optimisation of an ultrafast pulse source using a genetic algorithm. *Scientific Reports* **6,** 37616 (2016) (cit. on p. 83).

234. Andral, U. *et al.* Toward an autosetting mode-locked fiber laser cavity. *JOSA B* **33,** 825–833 (2016) (cit. on p. 83).

235. Baumeister, T., Brunton, S. L. & Nathan Kutz, J. Deep learning and model predictive control for self-tuning mode-locked lasers. *Journal of the Optical Society of America B* **35,** 617–626 (2018) (cit. on p. 83).

236. Kokhanovskiy, A., Ivanenko, A., Kobtsev, S., Smirnov, S. & Turitsyn, S. Machine Learning Methods for Control of Fibre Lasers with Double Gain Nonlinear Loop Mirror. *Scientific Reports* **9,** 2916 (2019) (cit. on p. 83).

237. Pu, G., Yi, L., Zhang, L. & Hu, W. Intelligent programmable mode-locked fiber laser with a human-like algorithm. *Optica* **6,** 362–369 (2019) (cit. on p. 83).

238. Wetzel, B. *et al.* Customizing supercontinuum generation via on-chip adaptive temporal pulse-splitting. *Nature Communications* **9,** 4884 (2018) (cit. on p. 83).